Institut de Physique de l'Université de Neuchâtel (Suisse)

Structural and electronic properties of self-assembled nanostructures on silicon surfaces

Thèse

présentée à la Faculté des Sciences

de l'Université de Neuchâtel

pour l'obtention du grade de Docteur ès Sciences par

Corsin Battaglia

soutenue le 7 mai 2008

en présence du directeur de thèse

Prof. Philipp Aebi

et des rapporteurs

Prof. Wolf-Dieter Schneider, EPFL

Prof. Christophe Ballif, Université de Neuchâtel

Dr. Pascal Ruffieux, EMPA

Neuchâtel, 27 mai 2008

Université de Neuchâtel

FACULTE DES SCIENCES
Secrétariat-Décanat de la faculté
- Rue Emile-Argand 11
- CP 158
- CH-2009 Neuchâtel

IMPRIMATUR POUR LA THESE

Structural and electronic properties of self-assembled nanostructures on silicon surfaces

Corsin BATTAGLIA

UNIVERSITE DE NEUCHATEL

FACULTE DES SCIENCES

La Faculté des sciences de l'Université de Neuchâtel,
sur le rapport des membres du jury

MM. P. Aebi (directeur de thèse),
C. Ballif, W.-D. Schneider (EPF Lausanne)
et P. Ruffieux (EMPA, Thoune)

autorise l'impression de la présente thèse.

Neuchâtel, le 16 mai 2008

Le doyen :
F. Kessler

Felix Kessler

■ Téléphone : +41 32 718 21 00 ■ E-mail : secretariat.sciences@unine.ch ■ www.unine.ch/sciences

Keywords

self-assembly, nanostructures, atomic chains, surface reconstructions, silicon surfaces, scanning tunneling microscopy and spectroscopy, dynamical low-energy electron diffraction, angle-resolved photoemission spectroscopy, density functional theory

Mots clés

auto-assemblage, nanostructures, chaînes atomiques, reconstructions de surface, surfaces de silicium, microscopie et spectroscopie tunnel, diffraction dynamique d'électron de basse énergie, spectroscopie de photoélectrons résolue en angle, théorie de la fonctionnelle de densité

Abstract

This thesis reports new results on self-assembled nanostructures on silicon surfaces studied by a combination of low-temperature scanning tunneling microscopy (STM) and spectroscopy (STS), dynamical low-energy electron diffraction (LEED), angle-resolved photoemission spectroscopy (ARPES) and first-principles calculations within the framework of density functional theory (DFT). Understanding quantum phenomena at semiconductor surfaces is of ever increasing importance for both science and technology as the size of electronic, magnetic and optical devices shrinks down to the nanometer regime. In particular, here we investigate the structural and electronic properties of the Si(331)-(12×1) surface reconstruction and of atomic chains self-assembled on the Si(111) surface.

Si(331) is an important surface as it is the only planar silicon surface with a stable reconstruction located between (111) and (110). We optimized the annealing sequence and were able to obtain almost defect free, atomically precise surface areas approaching micrometer dimensions. The unprecedented perfection of the surface combined with its pronounced structural anisotropy makes it a promising candidate to serve as a template for the growth of self-assembled hetero-epitaxial nanostructure arrays. Since its discovery more than 17 years ago several structural models have been proposed. However, none of these models is able to explain our high resolution STM images. Combining the complementary strength of STM, LEED and DFT, we propose a new structural model for the Si(331)-(12×1) reconstruction and discuss its stability and electronic properties.

Secondly we focus on the mechanisms underlying the self-assembly of atomic chains on the Si(111) surface. These have attracted tremendous interest because of their quasi one-dimensional electronic properties. Based on a combined STM and LEED study, we propose a new structural model for the Gd induced atomic chains. We conclude that besides mono- and divalent adsorbates, also trivalent adsorbates are able to stabilize atomic chains, establishing silicon honeycomb and Seiwatz chains as universal building blocks in adsorbate induced atomic chain reconstructions. The systematics in the self-assembly is explained by relating the valence state of the adsorbate to the accessible symmetries of the chains. We further examine theoretically the stability of the various chain phases using first-principles electronic structure methods and compare our results to experiment.

Zusammenfassung

In dieser Doktorarbeit werden Messungen an selbst-organisierten Nanostrukturen auf Silizium Oberflächen vorgestellt, welche mit Hilfe einer Kombination aus Tieftemperatur Rastertunnelmikroskopie (STM) und -spektroskopie (STS), sowie dynamischer Beugung langsamer Elektronen (LEED), winkelaufgelöster Photoelektronenspektroskopie (ARPES) und *ab initio* Rechnungen im Rahmen der Dichtefunktionaltheorie (DFT) untersucht wurden. Das Verständnis grundlegender Quantenphänomene auf Halbleiteroberflächen ist von stetig wachsender Bedeutung sowohl für die Wissenschaft als auch für die Industrie, da die Ausmasse elektronischer, magnetischer und optischer Bauteile mittlerweile auf die Nanometerskala geschrumpft sind. Im Rahmen der hier vorliegenden Arbeit bestimmen wir die strukturellen und elektronischen Eigenschaften der Si(331)-(12×1) Oberflächen Rekonstruktion sowie jene selbst-organisierter Atomketten auf Si(111).
Si(331) ist als Oberfläche von besonderer Bedeutung, da es die einzige flache Oberfläche zwischen den Hochsymmetrieebenen (111) und (110) ist, die eine stabile Rekonstruktion aufweist. Die Probenherstellungsprozedur wurde soweit optimiert, dass fast defektfreie, Mikrometer grosse Bereiche mit atomarer Präzision hergestellt werden können. Die erstmalig erreichte Qualität der Oberfläche zusammen mit ihrer ausgeprägten Anisotropie bietet ideale Vorraussetzungen, um als Vorlage für selbst-organisierte hetero-epitaktische Nanostrukturen eingesetzt zu werden. Seit der Entdeckung vor mehr als 17 Jahren wurden bereits mehrere Modelle vorgestellt, welche die atomare Struktur beschreiben sollten. Keines dieser Modelle ist jedoch in der Lage, unsere hoch aufgelösten STM Bilder zu erklären. Die sich gegenseitig ergänzenden Vorteile von STM, LEED und DFT erlauben es uns, ein neues Modell der Struktur von Si(331)-(12×1) vorzuschlagen.
Des Weiteren haben wir die Mechanismen untersucht, welche der Selbst-Organisation atomarer Ketten auf Si(111) zugrunde liegen. Diese haben aufgrund ihrer quasi eindimensionalen elektronischen Eigenschaften grosse Aufmerksamkeit geweckt. Basierend auf den Ergebnissen aus STM und LEED Messungen bestimmen wir erst die Struktur Gd induzierter Ketten. Daraus schliessen wir, dass neben mono- und divalenten auch trivalente Adsorbate in der Lage sind, stabile Silizium *honeycomb* und *Seiwatz* Ketten zu bilden, was sie als universelle Bausteine Adsorbat induzierter Rekonstruktionen etabliert. Zudem lässt sich klar eine Systematik im Selbst-Organisationsprozess, anhand eines Zusammenhanges zwischen dem Valenzzustand des Adsorbates und den erlaubten Symmetrien der Ketten, aufzeigen. Die Phasenstabilität der Ketten wird schliesslich mit Hilfe von *ab initio* Berechnungen untersucht und mit Experimenten verglichen.

Résumé

Cette thèse présente de nouveaux résultats sur les nanostructures auto-assemblées sur surfaces de silicium étudiées par différentes techniques complémentaires: la microscopie et spectroscopie tunnel (STM/STS) à basse température, la diffraction dynamique d'électron de basse énergie (LEED), la spectroscopie de photoélectrons résolue en angle (ARPES) ainsi que des calculs *ab initio* réalisés dans le cadre de la théorie de la fonctionnelle de densité (DFT). A mesure que la taille des dispositifs électroniques, magnétiques et optiques s'approche du régime nanométrique, la compréhension des phénomènes quantiques présents sur les surfaces semiconductrices est de plus en plus importante pour la science et pour la technologie. Nous investiguons ici les propriétés structurales et électroniques à l'échelle atomique de la reconstruction Si(331)-(12×1), ainsi que des chaînes atomiques auto-assemblées sur la surface de Si(111).

La surface de Si(331) est importante puisque c'est la seule surface plane de silicium qui présente une reconstruction stable avec une orientation comprise entre les directions (111) et (110). Après avoir optimisé la méthode de préparation de la surface, nous sommes désormais capables d'obtenir des régions de taille quasi micrométrique où l'arrangement atomique ne présente presque aucun défaut. Cette perfection sans précédent de la surface, combinée avec son anisotropie structurale prononcée, font de cette surface un candidat prometteur pour guider la croissance auto-assemblée de réseaux de nanostructures hétéro-épitaxiales. Depuis sa découverte datant de plus de 17 ans, plusieurs modèles structuraux ont été proposés. Cependant, aucun de ces modèles n'a été capable d'expliquer nos images STM à haute résolution. En exploitant la complémentarité de STM, LEED et DFT, nous proposons un nouveau modèle structural pour la reconstruction Si(331)-(12×1) et discutons sa stabilité et ses propriétés électroniques.

Nous nous focalisons ensuite sur les mécanismes sous-jacents de l'auto-assemblage des chaînes atomiques sur la surface de Si(111). Ces nanostructures ont suscité un énorme intérêt en raison de leurs propriétés électroniques quasi uni-dimensionnelles. En se basant sur la combinaison de nos études STM et LEED, nous proposons un nouveau modèle structural pour les chaînes atomiques induites par le Gd. Nous concluons qu'outre les adsorbats mono- et divalents, les adsorbats trivalents sont aussi capables de stabiliser des chaînes atomiques. Ceci établit les chaînes constituées de silicium du type *honeycomb* et *Seiwatz* comme blocs de construction universels dans les reconstructions de chaîne atomiques induites par les adsorbats. La systématique dans l'auto-assemblage est expliquée en reliant l'état de valence de l'adsorbat aux symétries accessibles des chaînes. Nous examinons encore théoriquement la stabilité des différentes phases de chaînes en utilisant des méthodes de calculs de structure électronique *ab initio* et comparons nos résultats aux expériences.

Preface

The content of this thesis is based on research carried out in the Electron Spectroscopy Group at the Institut de physique, Université de Neuchâtel during the period 2004-2008. This work was supported by the Swiss National Science Foundation (SNF) through Division II and the National Center of Competence in Research (NCCR) Materials with Novel Electronic Properties (MaNEP). First-principles calculations presented in this thesis were performed in collaboration with Dr. Katalin Gaál-Nagy of the Milan node of the European Theoretical Spectroscopy Facility (ETSF), Università di Milano within the Nanoquanta Network of Excellence and Dr. Steven C. Erwin of the Center of Computational Materials Science, U.S. Naval Research Laboratory Washington DC.
The thesis consists of four chapters. Chapter 1 gives an introduction to self-assembled nanostructures on silicon surfaces. Chapter 2 describes experimental and theoretical techniques including a description of the newly installed LT-STM setup with sample preparation and characterization facilities and the IV-LEED setup developed during this thesis. Chapter 3 presents new results on pristine Si surface reconstructions. Chapter 4 focuses on self-assembled atomic chains grown on Si(111) surfaces. Chapter 3 and 4 contain sections from published articles which stand completely on their own and can be read independently. For sequential reading this leads inevitably to redundancies. Articles included in this thesis are

C. Battaglia, K. Gaál-Nagy, C. Didiot, C. Monney, E.F. Schwier, M.G. Garnier, P. Aebi,
A new structural model for the Si(331)-(12×1) reconstruction,
to be submitted ..... page 82

C. Battaglia, H. Cercellier, C. Monney, M.G. Garnier, P. Aebi,
Stabilization of silicon honeycomb chains by trivalent adsorbates,
Europhys. Lett. **77**, 36003 (2007)
http://arxiv.org/abs/cond-mat/0611776, ... page 101

C. Battaglia, H. Cercellier, C. Monney, M.G. Garnier, P. Aebi,
Unveiling new systematics in the self-assembly of atomic chains on Si(111),
Proceedings of the International Conference on Nanoscience and Technology ICN+T 2007,
J. Phys.: Conf. Ser. 100, 052078 (2008)
http://arxiv.org/abs/0706.3175 ..... page 109

C. Battaglia, P. Aebi, S. Erwin
Stability and structure of atomic chains on Si(111),
submitted to Phys. Rev. B
http://arxiv.org/abs/0805.1843 ..... page 114

Parts of the thesis were devoted to the study of two-dimensional transition metal dichalcogenides. These results are not included here. For a complete list of publications including the work on transition metal dichalcogenides see page 134.

Contents

Chapter 1

Introduction

Nanotechnology holds the potential to meet many of the greatest global challenges in science, medicine, energy and industry. The guiding vision of nanotechnology is the fabrication of a wide range of functional devices and products with atomic precision. However, there are immense technical challenges in attaining complete control over the structure of matter. Nevertheless, physical principles and examples from nature both indicate the promise of extending today's limited atomically precise manufacturing capabilities to larger scales, greater complexity and a wider range of materials.

Current techniques for implementing atomically precise systems may be divided into two classes [1]. The first one is anchored in the direct manipulation of atomic and molecular structures by means of a scanning probe device. The use of a scanning probe tip as lithographic tool has revealed exciting possibilities to create nanoscale structures down to the atomic scale [2]. Mechanosynthesis of nanostructures involves mechanical positioning of atoms or molecules on crystal surfaces by the probe to direct the creation and breaking of bonds [3,4]. Alternatively, synthesis can be directed by creating reactive sites which then react or bind with molecules from an ambient gas or liquid. This method has the advantage that it avoids the need for binding and transporting reactive molecules with the probe, since the selective activation plus reaction sequence requires no molecular placement and transfer operation. However, the intrinsic slow speed of such serial approaches presents a serious hurdle for technological applications.

A promising bottom-up alternative to built atomically precise systems is self-assembly [5]. Self-assembly refers to any process in which a disordered system of preexisting components spontaneously forms an organized structure or pattern as a consequence of specific interactions among the components themselves without external direction. The folding of polypeptide chains into proteins is an example for a self-assembled biological system. The wide range of functions that proteins carry out in living organisms makes them a natural candidate as building blocks and active working components of productive nanosystems [6]. Besides its role as a carrier of genetic information, DNA serves as structural raw material to create self-assembled DNA

complexes with specific properties [7]. Self-assembled monolayers of molecules on crystal surfaces are also studied intensively since the molecules can be equipped with chemical functionality [8]. Self-assembly is not only useful in the synthesis of organized macromolecular structures, but also in the formation of templates supporting complex three-dimensional architectures. Compared to mechanosynthesis, self-assembly offers the advantage that it is intrinsically parallel and thus allows fast, low-cost and large-scale production.

The need for atomically precise nanostructures is well illustrated using the example of traditional silicon based electronic devices. Since the invention of the transistor in 1947, the traditional top-down fabrication methods of the microelectronic industry have been continuously refined to produce ever smaller, faster and more powerful devices. Intel's atom processor announced in March this year contains 47 million transistors on an area of less than 25 mm^2. The simple downscaling of existing electronic components, however, reaches limits in terms of technology as well as the cost of manufacture [9, 10]. Typical dimensions of state-of-the-art silicon integrated circuit product are currently around 45 nm and the industry is facing serious problems in upholding the trends due to fundamental physical limits [11] as it works towards future technology nodes at 32 nm, 22 nm and below [9].

Transistors are essentially little switches which consist of a source, where electrons enter, the drain, where electrons leave, and a gate that controls the flow of electrons through the channel which connects source and drain. When the channel is open and electrons flow from the source to the drain, a computer reads "1". If no current flows, the transistor represents "0". Within the current technology generation, gate sizes are of the order of 18 nm [9]. Shrinking the size of the gate further, electrons will start to pass through the channel on their own via quantum tunneling even when the gate is closed.

Further problems must be expected due to the fact that current technology is based on doping of silicon with donor and acceptor impurities. The doping densities, which are usually below 10^{20} per cm^3, are much lower than the densities of atoms in a solid, which are of the order of 10^{23} per cm^3. Therefore to go to the ultimate limits of atomic size, a new type of transistor, without the traditional doping, is needed. One way out may be the atomically precise synthesis of electrically conventional transistors, but with atomically precise positioning of impurity atoms [1]. Synthesis of exotic, but proven, active devices, such as carbon nanotube [12] or semiconductor nanowire [13, 14] transistors may represent a second alternative. The fact that scaling does not extrapolate into the nanoscale world is a curse for the traditional semiconductor industry but represents a chance for nanotechnology.

In view of future applications, it is highly desirable to integrate nanodevices into advanced silicon technology. Although silicon is a very inefficient light emitter due to its indirect bandgap, operation of a silicon Raman laser has been demonstrated [15]. However, only recently silicon has been considered as a practical option for photonics. Due to the wavelengths typically used for optical transport and silicon's high index of refraction, existing manufacturing technologies from the electronic indus-

try are sufficient to process silicon waveguides requiring features of the order of 0.5 - 1 μm [16]. Silicon is not only used for electronic and photonic applications, but also dominates the current photovoltaic market [1]. Within the actual trend towards thinner and more efficient solar cells, surfaces and interfaces are of increasing importance [17]. Silicon surfaces also present attractive building platforms for molecular electronics [18] and have distinct advantages over metallic surfaces [19].
The importance of understanding surface processes at the atomic level had been recognized since the early part of the twentieth century, but it was not until the 1960s with the introduction and development of ultra-high vacuum techniques that experiments on atomically precise surfaces became available. Many of the analytical tools developed in the field of surface science, above all scanning tunneling microscopy, have been essential for the birth of nanoscience and nanotechnology. In chapter 2, we describe experimental and theoretical techniques used in this study. Specific aspects of low-temperature scanning tunneling microscopy (STM) and spectroscopy (STS) on semiconductor surfaces are discussed. Part of the mission of this thesis was the installation and maintenance of the newly acquired low-temperature scanning tunneling microscope including the ultra-high vacuum chamber, sample preparation and characterization facilities. Low-energy electron diffraction (LEED) has been used not only to check the long range order at the surface but also to determine precise atomic coordinates. To do this, fully dynamical LEED capabilities were implemented into a conventional LEED setup. The development of a data analysis package as well as the installation of programs for the calculation of phaseshifts [20] and simulated LEED intensity vs voltage (IV) curves [21] within a multiple scattering approach give access to the full power of LEED. The electronic structure has been studied using angle-resolved photoemission spectroscopy (ARPES). Structural models were tested theoretically using density functional theory (DFT).
A complete understanding of structural and electronic properties of silicon surfaces at the atomic scale is of tremendous importance. Physicist Wolfgang Pauli used to say "God made the bulk, surfaces were invented by the devil" [22]. This quote expresses well the complexity of the phenomena encountered on surfaces. The complete characterization of a surface requires not only knowledge of the kind of atoms, which are present at the surface, but also where they are. The elaboration of a structural model is thus of prime importance, since it is the geometrical arrangement of the surface atoms which determines electronic, optical, magnetic and catalytic properties of the surface. It has been known since 1958, that atoms at the surface of a semiconductor assume a different structure than that of the bulk [23]. The creation of a surface results in broken chemical bonds, so called dangling bonds, pointing into the vacuum. Dangling bonds are energetically unfavorable causing surface atoms to rearrange or reconstruct in order to lower the total energy of the surface. Reconstruction results in highly complex atomic architectures. The determination of the atomic structure requires the complementary role of different experimental and theoretical techniques. Still no single technique can do it alone. It took 26 years of combined effort to solve the atomic structure of the famous Si(111)-(7$\times$7) reconstruction. In

chapter 2, we describe known silicon surface reconstructions emphasizing the role of basic structural building blocks. We then focus on the Si(331)-(12×1) reconstruction discovered 17 years ago [24]. Our experimental results allow us to propose a new atomic structural model for the Si(331)-(12×1) reconstruction containing the pentamer as a basic building block.

In chapter 3 we concentrate on self-assembled atomic chains on the Si(111) surface. These consist of silicon atoms and may be stabilized by the adsorption of foreign atoms on Si(111). Atomic chains represent the ultimate limit in miniaturization of an electric cable, since they are only one or two atoms wide. What makes atomic chains so fascinating is that electrons passing through these chains behave radically different to what is expected from our experience coming from the macroscopic world. Spatial confinement of electrons results in phenomena only explainable via quantum mechanics. The properties of electrons become more and more exotic as one progresses from the three-dimensional world into lower dimension. In one dimension, the Luttinger theory predicts that electrons loose their identity and separate into spinons and holons traveling at different velocities [25]. Even the very existence of a metallic state in one dimension is in question. Peierls argued that a one-dimensional electron gas is unstable with respect to charge density wave formation [26]. Also the spin degrees of freedom result in interesting phenomena in low dimension. Recently the splitting of the energy bands observed for certain atomic chains has been interpreted as a spin-splitting due to the Rashba effect in agreement with theoretical predictions [27, 28].

The traditional approach to one-dimensional electronic systems is based on three-dimensional solids consisting of weakly coupled chains embedded in an ideally electronically passive matrix. Although ideal for bulk-sensitive measurements, the residual coupling between the chains is difficult to control. More recently the synthesis of nanowires as well as carbon nanotubes has stimulated physics in one dimension. However, it is very difficult to attach leads to a single nanowire allowing to probe the electronic states. Attaching atomic chains on atomically precise surfaces opens the door to the entire range of powerful surface science methods. Furthermore compared to metallic substrates, semiconductor surfaces offer the advantage that their electronic surface states are completely decoupled from the bulk states allowing for genuinely low-dimensional states.

In chapter 3 we first retrace research on atomic chains leading to the honeycomb chain-channel model, which serves as the starting point for our research. We then present experimental results leading us to propose a new structural model for the Gd induced atomic chain system. Further we have discovered a new systematics in the self-assembly process of atomic chains relating the valence state of the adsorbate to the allowed symmetries of the chains. The phase stability of atomic chains as a function of the adsorbate valence is investigated using first-principles calculations.

Chapter 2

Experimental and theoretical techniques

The complexity of phenomena encountered on semiconductor surfaces requires a complementary experimental approach. All experimental techniques, presented here, involve electrons as a probe. The underlying reason is that the mean free path of electrons in a solid is only of the order of a few Ångströms [29], rendering these methods intrinsically sensitive to the surface.
Scanning tunneling microscopy (STM) is the most direct method to visualize the surface structure with atomic resolution in real space. Although inspection of STM images gives many hints about the actual atomic structure, the interpretation, though sometimes obvious, generally requires a comparison with theoretical calculations, since STM images represent a convolution of topographic and spectroscopic information. Low-energy electron diffraction (LEED) ideally complements STM, since it delivers structural information in reciprocal space. Periodicity and long range order of a surface are determined easily. Precise atomic coordinates may be extracted from the diffraction intensities. However, this method requires elaborate calculations.
Electronic properties are studied using angle-resolved photoemission spectroscopy (ARPES). ARPES is a momentum sensitive method and allows to directly map the electronic dispersion and Fermi surface of the system under investigation in reciprocal space. Local details of the electronic structure may be associated to local topographic features in real space via scanning tunneling spectroscopy (STS) virtually atom by atom. In order to obtain reproducible results on atomically clean surfaces, ultra-high vacuum (UHV) in the 10^{-10} mbar range is a stringent requirement for all these methods.

2.1 Scanning tunneling microscopy

Since its invention by Binnig and Rohrer in 1981 at the IBM research laboratories in Zürich [30–32], the scanning tunneling microscope (STM) has become one of the most important tools for studying surfaces at the atomic scale. A multitude of

related scanning probe microscopy (SPM) methods such as atomic force microscopy (AFM) [33], scanning near-field optical microscopy (SNOM) [34] and magnetic force microscopy (MFM) [35] has been developed since then. All of these methods have in common that an image of the surface is obtained by scanning a physical probe laterally across a grid of points on the surface, while simultaneously recording the probe-surface interaction as a function of position. Using a probe has the advantage that the resolution of scanning probe microscopes is not limited by diffraction, as is the case for instance for traditional optical microscopes and scanning electron microscopes, but only by the size of the probe-sample interaction volume, which can be as small as a few picometers.

In the case of the STM, an ideally atomically sharp conducting tip is scanned within a few Ångströms over a metallic or semiconducting surface. When applying a bias V or U of up to a few Volts between tip and sample, a current I typically of the order of 1 nA referred to as tunneling current can flow between tip and sample (see Fig. 2.1a)). Although classically forbidden, tunneling of electrons between tip and sample is allowed in quantum mechanics even before tip and sample come into contact. On the quantum scale, an electron exhibits wave-like behavior and can be described by a wave function $\psi(z)$ which represents the probability amplitude of finding it in a certain location z. From elementary quantum mechanics, assuming a one-dimensional tunneling geometry, an electron in the tip ($z = 0$) at the energy $\epsilon = E - E_F$, represented by its wavefunction $\psi(z)$ possesses a finite probability $|\psi(z)|^2$ of being in the sample at position z

$$T(\epsilon, z) = |\psi(z)|^2 = |\psi(0)|^2 e^{-2\kappa z},\ \kappa = \sqrt{\frac{2m}{\hbar^2}\Big(\frac{\phi_t + \phi_s}{2} - \frac{eV}{2} + \epsilon\Big)}.$$

Here ϕ_t and ϕ_s are the tip and sample workfunction, E_F the Fermi energy and e the charge of the electron. $T(\epsilon, z)$ is called the transmission factor which depends exponentially on the tunneling gap distance z. Electrons from higher energy levels are more likely to tunnel because of the reduced barrier height. Taking the free electron mass and realistic values for the work functions $\phi \approx 4 - 5$ eV, 2κ is of the order of 20 nm^{-1}. Thus a variation of the tip-sample distance of 0.1 nm results in an order of magnitude difference in the tunneling probability. The high sensitivity on the tip-sample distance is the reason for the extremely high vertical resolution of the STM which can reach the sub-picometer regime [36]. Furthermore only the last atom of the tip significantly contributes to the tunneling process allowing high lateral resolution.

To create an image of the surface, the tunneling current is fed into an electrical feedback loop which adjusts the tip-sample distance via a piezoelectric transducer in order to keep the tunneling current at a constant setpoint value. Variations in the tip height Δz induced by the local geometric but also electronic structure of the surface are then used to construct an image $\Delta z(x, y)$. Nearly topographic images are obtained in cases where geometrically induced height variations dominate.

Shortly after the invention of the STM, Tersoff and Hamann [37, 38] presented a

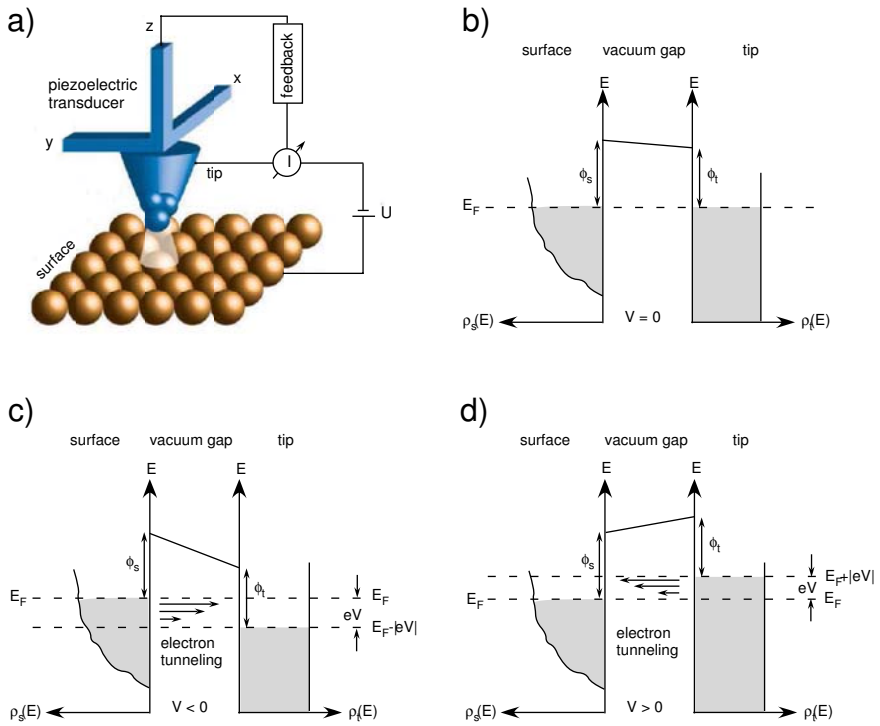

Figure 2.1: a) Sketch of the STM geometry. b) c) d) Schematic view of the quantum-mechanical tunneling process between an ideal tip with flat LDOS and a sample with an energy dependent LDOS. When no bias b) is applied, no net tunneling current is measured. When a negative bias c) is applied, electrons tunnel from the occupied states of the sample into the tip. When a positive bias d) is applied, electrons tunnel from the tip into the empty states of the sample.

theory for the tunneling process using first-order perturbation theory [39]. In a first approximation it is often assumed that the current produced by electrons tunneling across the vacuum gap into an energy level ψ_ν at energy E_ν is proportional to the energy dependent local density of states (LDOS) $\rho(x, y, E)$ defined by

$$\rho(x, y, E) = \sum_\nu |\psi_\nu(x, y)|^2 \delta(E_v - E).$$

Using this definition, the total tunneling current at location (x, y) may be expressed by (we drop (x, y) for simplicity) [40]

$$I \propto \int_{-\infty}^{+\infty} d\epsilon \rho_s(\epsilon)\rho_t(\epsilon - eV)(f_t(\epsilon - eV) - f_s(\epsilon))T(\epsilon, z). \tag{2.1}$$

Here $\rho_s(\epsilon)$ and $\rho_t(\epsilon)$ are the LDOS of the sample and the tip respectively and $f(\epsilon)$ is the temperature dependent Fermi-Dirac distribution. $T(\epsilon, z)$ is the transmission factor accounting for the tunneling barrier. At low temperature $f(\epsilon) \longrightarrow 1 - \Theta(\epsilon)$,

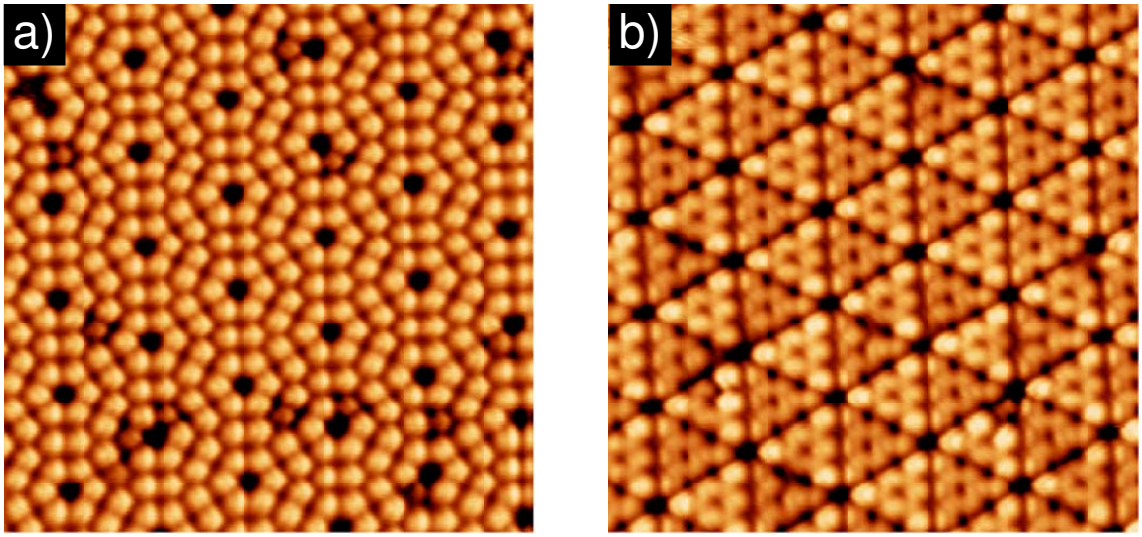

Figure 2.2: STM images of the Si(111)-(7×7) surface: a) tunneling into empty states of the surface, $U = 1.8$ V and b) tunneling out of filled states of the surface $U = -1.8$ V. $I = 0.2$ nA, 14nm×14nm.

assuming a constant LDOS for the tip and an approximately energy independent transmission factor ($\epsilon \ll \phi_s + \phi_t$) we get

$$I \propto \rho_t T(z) \int_0^{eV} d\epsilon \rho_s(\epsilon). \tag{2.2}$$

Since an electron may not just tunnel into an electronic state at the Fermi energy E_F, but into any state between E_F and $E_F + eV$ (see Fig. 2.1b-d)), one obtains the total tunneling current by integrating over all available energy levels between $\epsilon = 0$ and $\epsilon = eV$ ($\epsilon = E - E_F$). However, although STM allows direct observation of the atomic structure of a surface, one has to be aware of the complexity of the tunneling process when interpreting experimental data.

Fig. 2.2 presents STM images of the Si(111)-(7×7) reconstruction at a) positive (tunneling into empty states of the surface) and b) negative (tunneling out of filled states of the surface) bias. Each triangular subunit contains six protrusions at the locations of the adatoms of the DAS model [41,42] (see section 3.3 for a description of the model). At the corner holes where six triangular subunits join, the STM images show a depression about 2 Å lower than the height of the adatoms. It is clear from the differences between the two images that the bias dependence of the STM image encodes a lot of information. Whereas the empty state image suggests a six-fold symmetry, the filled state image clearly shows that the surface only exhibits a three-fold symmetry due to the presence of a stacking fault in every other triangular subunit. Additionally, within each half of the unit cell the three adatoms which are closer to the corner holes appear higher than the three interior adatoms. Thus, the images reveal four kinds of electronically inequivalent adatoms.

2.2 Scanning tunneling spectroscopy

Besides studying the topography of a surface, STM allows to obtain spectroscopic information with atomic resolution [43]. Taking the derivative of the tunneling current I in Eqn. 2.1 with respect to the gap voltage V and assuming an approximately constant transmission factor ($eV \ll \phi_s + \phi_t$), we get

$$\frac{\partial I}{\partial V} \propto \int_{-\infty}^{+\infty} d\epsilon \rho_s(\epsilon) \left[\frac{\partial \rho_t(\epsilon - eV)}{\partial V} \Big(f_t(\epsilon - eV) - f_s(\epsilon) \Big) + \rho_t(\epsilon - eV) \frac{\partial f_t(\epsilon - eV)}{\partial V} \right] T(\epsilon, z).$$

Assuming again a structureless LDOS for the tip $\partial \rho_t(\epsilon - eV)/\partial V = 0$ and using $\partial f_t(\epsilon - eV)/\partial V = \delta(\epsilon - eV)$ one obtains

$$\frac{\partial I}{\partial V} \propto \rho_t \int_{-\infty}^{+\infty} d\epsilon \rho_s(\epsilon) \delta(\epsilon - eV) T(\epsilon, z) = \rho_t \rho_s(eV) T(eV, z).$$

Thus the derivative of the tunneling current with respect to the bias voltage is directly proportional to the LDOS of the surface at energy eV.
In order to acquire a tunneling spectrum, the tip is placed over a point of interest (x, y) on the sample surface. Then the feedback loop is opened, i.e. z determined by the setpoint current remains constant, while the bias voltage V is ramped and the tunneling current $I(V)$ is recorded.
Fig. 2.3b) presents a typical dI/dV spectrum as a function of bias voltage V of Si(111)-(7×7) at $T = 5$ K recorded on top of the adatom marked by a white circle in the topography image in Fig. 2.3a). As is characteristic for a semiconductor we observe a large gap in the LDOS ranging from roughly -2V to 1V.[1] Several pronounced spectral features can be distinguished above and below the gap. In order to correlate these with the geometric structure of the surface, it is useful to acquire an entire series of scanning tunneling spectra $dI/dV(x, y, V)$ distributed on a regular grid on the surface. This acquisition mode is known as current imaging tunneling spectroscopy (CITS) [43]. After recording a first spectrum by going trough the voltage ramp on a given point with the feedback loop open, the feedback loop is closed again and the tip is moved to the next point. Then the feedback loop is opened again and a second spectrum is acquired.
Once all spectra are acquired, the data can be represented in different ways. In Fig. 2.3c), a series of spectra along the lines $\mathbf{r}$ marked in Fig. 2.3a) have been extracted and represented by a color-coded image plot $dI/dV(\mathbf{r}, V)$. Here vertical lines represent the position of the corner hole and dashed lines indicate the position of an adatom. From these data one clearly sees that the various adatoms are not equivalent and possess their own characteristic energy states.
A second way to represent the data is to extract $dI/dV(x, y)|_V$ maps at a specified energy V as shown in Fig. 2.4. Such maps are useful for linking spectral features

[1] The energy gap of silicon is 1.17 eV at low temperature [44]. See section 2.2.5 for an explanation for this discrepancy.

to the topography. The color scale is the same as in Fig. 2.3c) allowing direct comparison. CITS involving a voltage ramp allows comparison of absolute intensities between maps acquired at different voltages. One could also acquire dI/dV maps at fixed voltage. However at each voltage the tip follows a different contour so that this kind of dI/dV maps contains a mixtures of geometric and electronic structure information complicating interpretation of the observed features.

2.2.1 Drift

During the acquisition of a typical dI/dV spectrum as shown in Fig. 2.3a), the feedback loop remains open for approximately 8s (400 points per spectrum with 20 ms integration time per point). Due to the exponential dependence of the tunneling current on the tip-sample distance a high mechanical stability along the z direction during acquisition of a dI/dV spectrum is absolutely necessary. Measuring at low temperature permits not only a substantial increase in spectral resolution [36], but significantly increases the stability of the tip and minimizes the drift. The lateral stability of the STM is also of high importance if one wants to acquire an entire grid of spectroscopic data and compare them to the topography. Fig. 2.3a) shows a topography image of the Si(111)-(7×7) surface, where each data point was recorded right before opening the feedback loop for the acquisition of the spectrum. A grid of 80×66 spectra has been acquired that way, requiring approximately 15 hours to complete the measurement (10 s per spectrum including the various switching periods). As can be determined from the small distortion of the image in Fig. 2.3a), the lateral drift is below 0.2 nm/h.

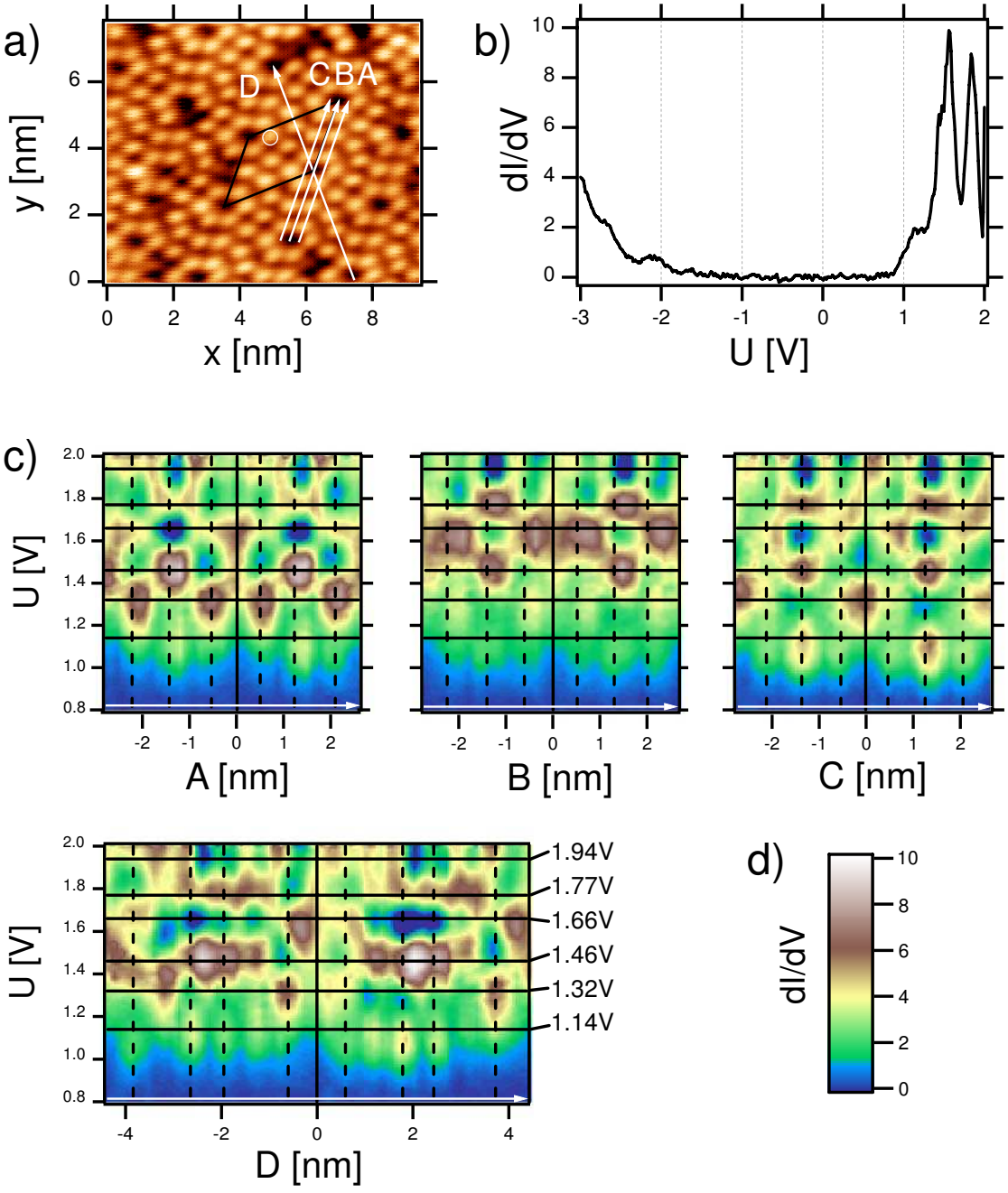

Figure 2.3: STS measurements on boron doped Si(111)-(7×7) at $T = 5$ K, $\rho = 0.022$ Ωcm, current setpoint $I = 0.2$ nA, modulation frequency $f = 472$ Hz, modulation amplitude $\Delta V = 22.5$ mV, $\tau = 20$ ms. a) Topography image at $U = 2$ V, b) dI/dV spectrum recorded on the adatom marked by a white empty circle in a), c) color-coded STS spectra along the lines A, B, C and D shown by white arrows in Fig. 2.3a). Full vertical lines indicate the position of the corner hole, dashed vertical lines indicate the position of an adatom.

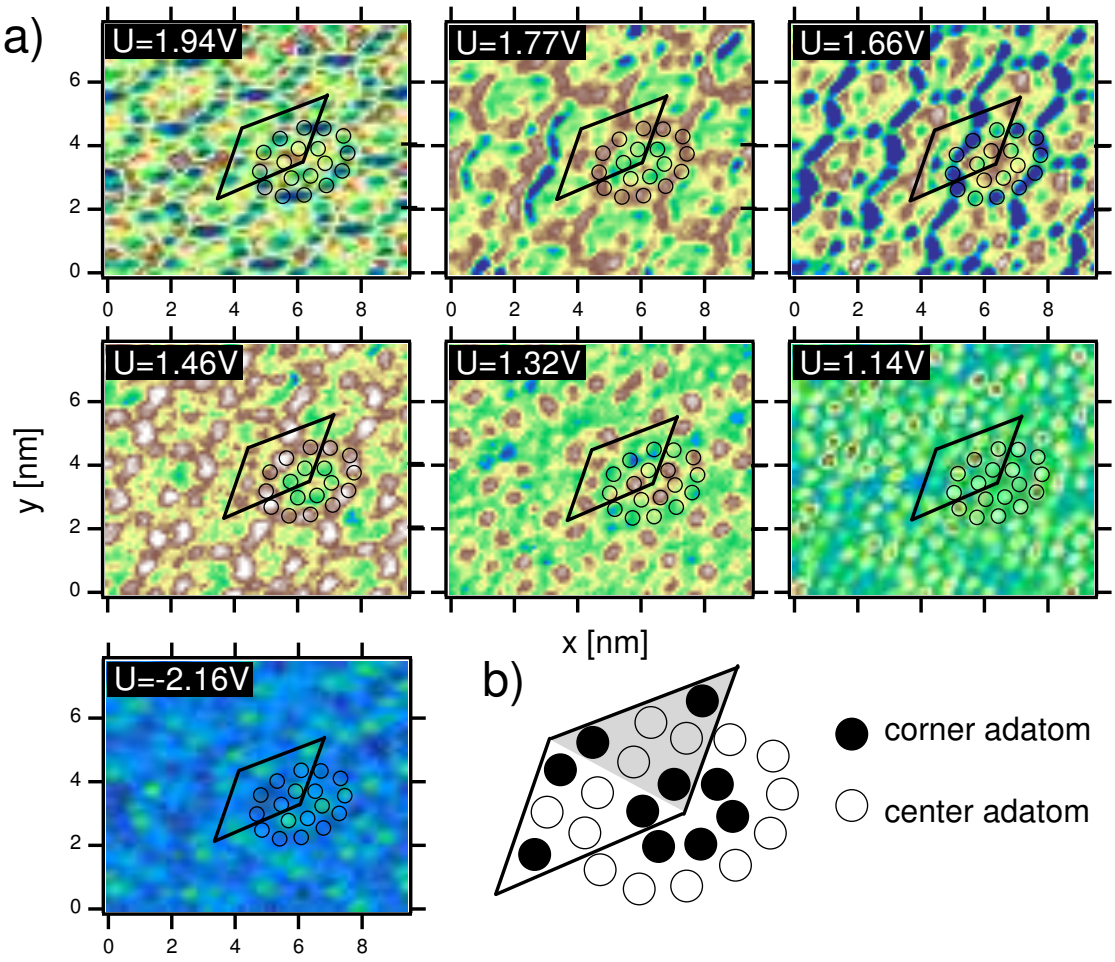

Figure 2.4: a) Color-coded dI/dV maps of Si(111)-(7×7) as a function of position for a given energy. The sampled area corresponds exactly to the area shown in Fig. 2.3a). The (7×7) unit cell is outlined as a guide to the eye. Circles indicate the position of the adatoms. b) Sketch of the adatom arrangement in the (7×7) reconstruction.

2.2.2 The lock-in technique

In principle the derivative dI/dV of the tunneling current I(V) could be obtained numerically, in practice however one always uses the lock-in technique, since the tunneling current often is too noisy to obtain reasonable results by numerical derivation. A lock-in amplifier adds a small sinusoidal modulation $\Delta V \sin(\omega t)$ to the tunneling voltage V. Adapting Eqn. 2.2, the resulting tunneling current is

$$I(\omega) \propto \rho_t T(z) \int_0^{e(V+\Delta V \sin(\omega t))} d\epsilon \rho_s(\epsilon).$$

Expanding the current in a Taylor series

$$I(\omega) \propto \underbrace{\rho_t T(z) \int_0^{eV} d\epsilon \rho_s(\epsilon)}_{I\big|_V} + \underbrace{\rho_t \rho_s(eV) T(eV,z)}_{\partial I/\partial V\big|_V} e\Delta V \sin(\omega t) + \ldots$$

we see that the first order term is directly proportional to the first derivative of the tunneling current (see Fig. 2.5a)). Inside the lock-in, the modulated tunneling current is multiplied by the reference signal $\sin(\omega t+\phi)$ and integrated over a specified time $\tau >> T = 2\pi/\omega$.

$$1/\tau \int_t^{t+\tau} dt I(\omega) \sin(\omega t + \phi) \propto \rho_t \rho_s(eV) T(eV,z) cos(\phi)$$

Here ϕ is the phase difference between reference signal and tunneling current. The resulting signal is a DC signal during the period τ. The contribution from any signal that is not at the same frequency as the reference signal as well as the out-of-phase component of the signal that has the same frequency as the reference signal is attenuated essentially to zero. The output signal of the lock-in is directly proportional to the LDOS of the surface ρ_s at the tunneling voltage V.
Although increasing the modulation amplitude ΔV increases the signal at the input of the lock-in amplifier, it also limits the energy resolution of the measurement. However, as long as the modulation amplitude is significantly smaller than the characteristic spectral features, this broadening can be neglected.

2.2.3 Mechanical noise

As we have seen in the previous section, the lock-in allows to electronically measure the first derivative of the tunneling current by transposing the signal from zero frequency to the frequency of modulation $f = \omega/2\pi$. With this method noise originating from mechanical vibrations coupling into the tunneling current via small variations in z and thermal noise generated in the amplifiers is efficiently suppressed.
The choice of the modulation frequency should be made carefully avoiding mechan-

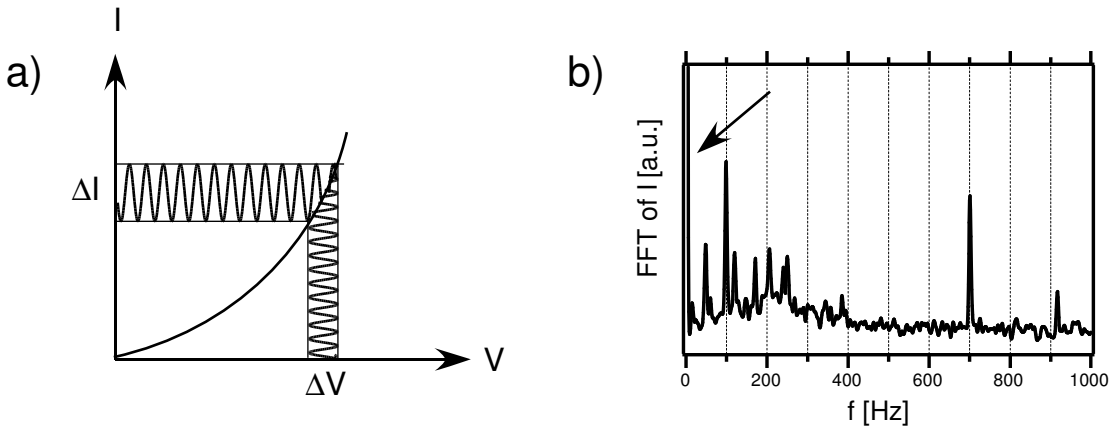

Figure 2.5: a) A sketch of the lock-in principle: a small modulation ΔV of the tunneling voltage V results in a modulation ΔI of the tunneling current I. ΔI depends on the slope of the $I(V)$ curve. Thus it is proportional to $\partial I/\partial V$. b) FFT of I. Note the actual tunneling signal at very low frequency marked by the arrow.

ical eigenfrequencies of the STM (including the vacuum chamber with all its components) which can be determined by analyzing the spectral content of the tunneling current. In Fig. 2.5b) we show the frequency spectrum of the tunneling current obtained by fast Fourier transform (FFT) of I, acquired while the tip was not scanning (point mode). The high value at low frequency marked by an arrow represents the actual tunneling current we are interested in. The spectral component at zero frequency is approximately 100 times larger than the baseline value of the spectrum. At higher frequency, besides a 700 Hz noise, the 100 Hz hum dominates the spectrum. Above 400 Hz the spectrum is attenuated by the low pass filters located right before the preamplifier output. For the determination of the eigenfrequencies of the STM, it is useful to perform repeated sequential acquisition of FFT tunneling spectra as a function of time as shown in Fig. 2.6a) in a logarithmic gray scale map. We clearly see again the 100 Hz component accompanied by a weaker 50 Hz and 200 Hz branch and various permanent branches at other frequencies. Most of these branches get excited by external sound and vibration sources such as fans, mechanical pumps etc. To demonstrate this we turned on the scroll pump in the neighboring ARPES lab at $t = 70$ s. Additional branches immediately appear and disappear again after turning the pump off. However, the origin of some branches remains unidentified such as for example the branch at around 700 Hz. It appears that depending on the momentary tip condition and tip position some frequencies may be picked up more easily (see Fig. 2.6c) where this 700 Hz component is absent).
In order to study the sensitivity of the tunnel junction to an external sound excitation more systematically, we have amplified an acoustic sine wave via an external high fidelity speaker system and slowly ramped the frequency from 0 to 1 kHz while measuring FFTs of I (see Fig. 2.6c)). Again we see several eigenfrequency branches (horizontal in this plot). More interesting is the multiplet of diagonal branches high-

lighted in the sketch in Fig. 2.6d). The most prominent one corresponds exactly to the excitation frequency f (slope=1). The faint higher order branches (slope=2, 3, 4, ...) correspond to integer harmonics of the excitation frequency. It is not clear whether these harmonics are produced directly by the speaker system or correspond to higher order excitations of the STM chamber.
We also observe shifts of some of the branches as a function of the temperature of the STM stage. Changing the temperature of operation may require readjustment of the three-point port aligner to make sure that the STM swings freely and that the suspension springs do not touch the cryostat. We have further noticed branches which shift as a function of the cryostat filling level. In Fig. 2.6b) we have acquired FFTs during 48 hours starting with a full cryostat. During the first hours, a fraction of a branch located at 600 Hz moves down to 570 Hz, then it moves again up to 600 Hz and finally reaches 700 Hz after 48 hours. It must be emphasized that during the entire 48 hours the STM remained at 77 K. The spectrum also depends on the momentary lateral tip position which modifies the center of gravity of the suspended STM stage and therefore the coupling of the STM stage with the outside via the suspension springs. It is obviously of prior importance to avoid any contact of the suspension springs with the cryostat.

In order to avoid unnecessary problems, the modulation frequency for the lock-in should be selected in a region which is not polluted by noise. The use of external sound and vibration sources such as fans, air conditioners etc. should be reduced to a minimum.

2.2.4 Crosstalk

A serious drawback of the lock-in technique is the crosstalk induced by the capacity C of the wires connecting sample and tip. When applying a voltage modulation, a parasitical alternating current $I_c = C\frac{dV}{dt}$ is flowing across the junction independently of the tunneling process. Due to the capacitive coupling, this current is dephased by 90^o with respect to the actual tunneling current across the junction, which behaves like an ohmic resistor $R = V/I$. Although the phase sensitive detection of the lock-in is in principle able to separate the two contributions to the total current, the crosstalk current can overcome the signal of interest by several orders of magnitude, representing a serious nuisance to the measurement. Under such conditions a correct phase adjustment is crucial in order to obtain accurate spectroscopic data. Furthermore a dominant crosstalk signal reduces the dynamic range of the lock-in amplifier accessible for the actual tunneling signal. Here a crosstalk compensation circuit is useful, which injects, via a small capacitance, a variable fraction of the modulation voltage dephased by 180^o with respect to the actual modulation signal into the tunneling current in order to eliminate the crosstalk current before it enters the lock-in amplifier.

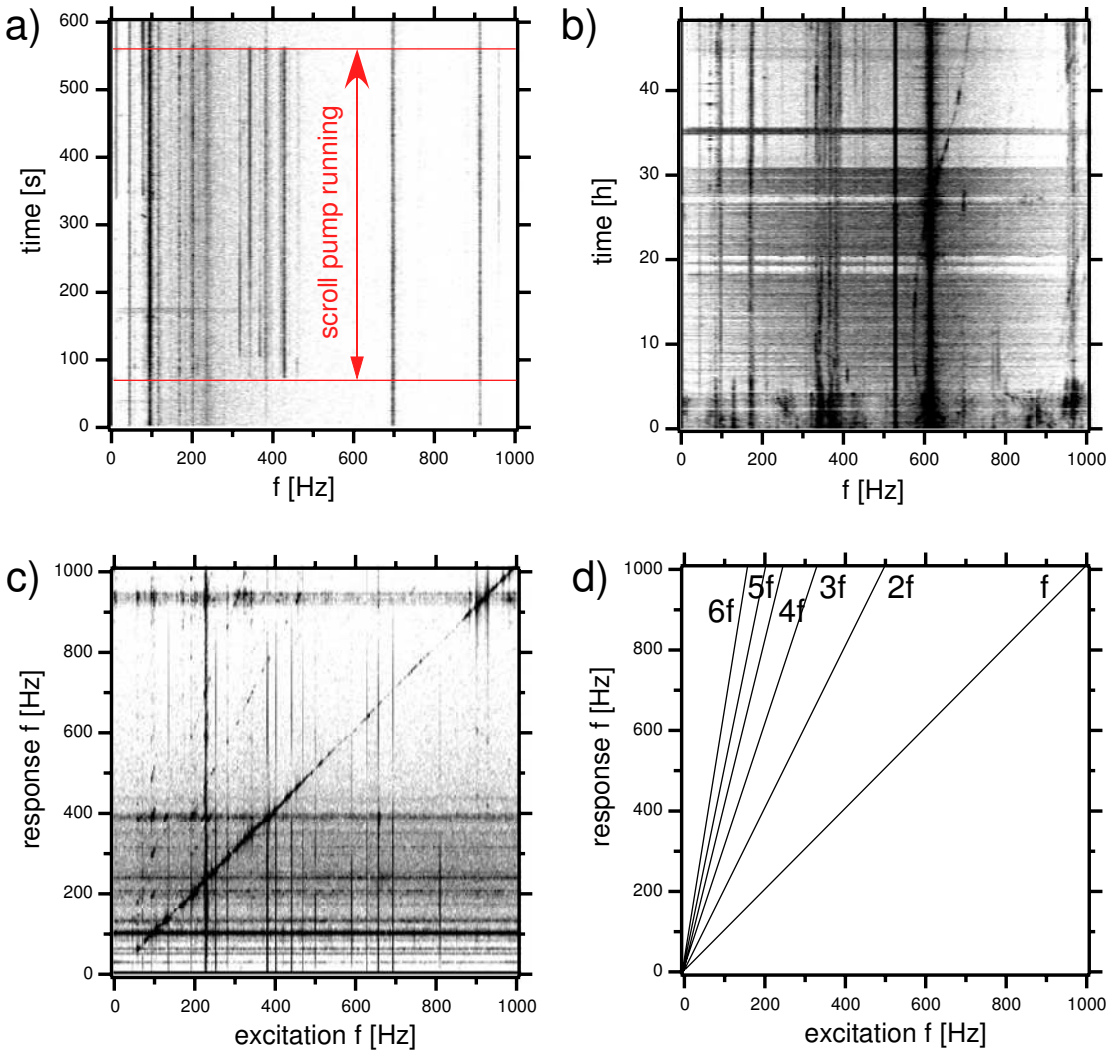

Figure 2.6: a) FFT map of the tunneling current as a function of time. The noise induced by the scroll pump is clearly seen in the tunneling current. b) FFT map as a function of time showing the effect of the cryostat filling level on the eigenmodes. c) FFT map as a function of external sound excitation frequency. d) A sketch of the FFT map shown in c) emphasizing observed harmonics. All spectra were measured at 77 K on an Ag film deposited at 100 K on Si(111)-(5×"2")-Au and annealed to 300 K. $U = -0.4$ V, $I = 0.1$ nA, no modulation was applied, the tip was in point mode, i.e. not scanning.

2.2.5 Band-bending and non-equilibrium tunneling

At room temperature, one usually considers that spectroscopy curves represent the coupling between the tip and the sample surface since the tunneling resistance is of the order of $R = 1$ to 10 GΩ. However, at low temperature, where the resistivity of the semiconductor sample can no longer be neglected, the analysis of tunneling spectra is more complicated due to band-bending effects and non-equilibrium carrier dynamics.

It has been pointed out already in the early days of STM that the electric field from the tip may penetrate into the bulk, causing a fraction of the applied voltage between tip and sample to be dropped in the semiconductor itself [45,46] . In a semiclassical approximation, the effect of the varying electrostatic potential in the semiconductor is simply to rigidly shift the energy bands [47]. In the limit of low current, this is known as tip-induced band-bending. Fig. 2.7 presents two prototypical situations for a n-type semiconductor, doped with electron donor impurities. When no bias is applied, tip and sample are in thermal equilibrium and their respective Fermi levels E_F are aligned (not shown). In Fig. 2.7a) a positive bias V is applied causing the Fermi level E_F of the metal tip to be shifted by an amount V with respect to the Fermi level of the semiconductor at a point deep inside the bulk ($z \to \infty$). Here E_c and E_v are the conduction minimum and valence band maximum respectively, E_G the energy of the band gap and ϕ_m and ϕ_s the workfunction of the metallic tip and the sample respectively measured from their respective Fermi levels E_F to the vacuum level E_{vac}. A fraction of the applied bias drops across the vacuum gap. The electric field from the tip penetrating into the semiconductor causes the energy bands to bend upwards close to the surface. Electrons in the near surface donor impurity levels (located 44 meV below the conduction band edge for phosphorus impurities [48]) are pushed away from the surface into the bulk, since the conduction band edge in the bulk is at a lower energy than the impurity state at the surface. The ionized impurities left behind at the surface are responsible for a positive space charge layer which screens the electric field from the tip. Since the electron density within the space charge layer is lower than the density of free electrons in the bulk, this particular type of space charge layer is called a depletion layer. In Fig. 2.7b) a negative bias V is applied. In this case, the energy bands at the surface are bend downwards. This causes electrons from the bulk donors to accumulate at the surface. This negatively charged space charge layer is called an accumulation layer. Note that in contrast to a depletion layer, where the positive space charge originates from spatially fixed, ionized donors, the accumulation layer is due to free electronic charge which is mobile [49]. Since free electrons may be compressed, accumulation layers are, in general, much narrower than depletion layers. Note also that at the tip side, negligible band-bending occurs, since the electric field is efficiently screened by the high density of free electrons.

Early attempts to quantify tip-induced band-bending on semiconductor surfaces have used a planar geometry as a starting point [50]. Feenstra [47] recently pre-

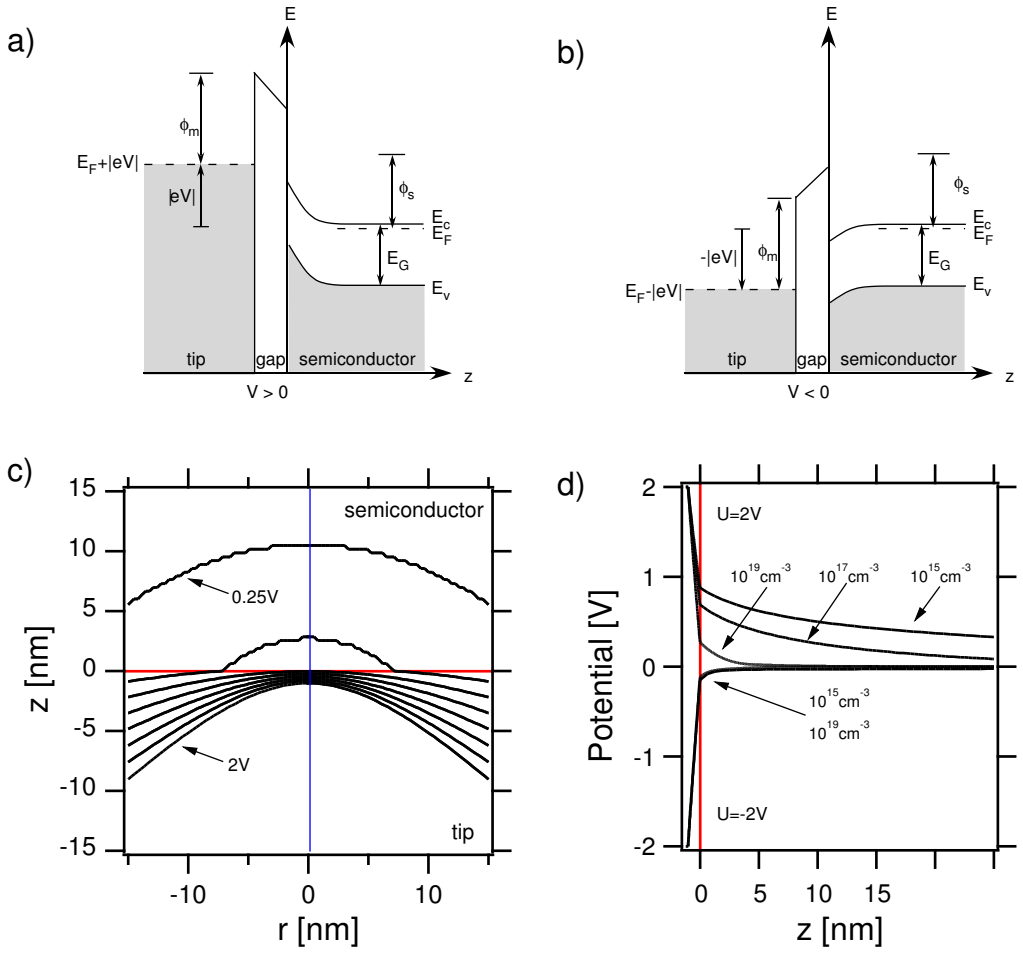

Figure 2.7: Tip-induced band-bending at a n-type semiconductor surface for a) positive and b) negative bias. The applied voltage V appears partly in the vacuum gap as an electric field and partly in the semiconductor interior as band-bending. In a) a depletion region forms below the semiconductor surface, whereas in b) an accumulation layer is observed. c) Potential distribution across the STM junction for a silicon sample in the depletion regime obtained from the theoretical calculation with a bias of $U = 2$ V and a phosphorus concentration of $N_D = 10^{17}$ cm^{-3}. The red line marks the semiconductor vacuum interface. d) Potential distribution in depletion ($U = 2$ V) and accumulation ($U = -2$ V) regime along the central axis (blue line in c)) as a function of z position for various phosphorus concentrations.

sented a three-dimensional finite-element method for solving the Poisson equation for the tip-semiconductor geometry. An extension taking into account surface states was presented in Ref. [51]. Fig. 2.7c) presents results obtained with the SEMI-TIP code of Feenstra [52] for a silicon sample with a phosphorus concentration of $N_D = 10^{17}$ cm^{-3}. All calculations presented hereafter assume a probe tip of radius 10 nm and of opening angle of 90^o, with the tip placed 1 nm above the surface.

Note that the tip geometry also influences the band-bending at the surface. However, here we do not study the influence of the tip geometry. The tip is at a potential of 2 V relative to a point far inside the semiconductor. The n-type silicon sample is characterized by its dielectric constant $\epsilon = 11.9$ [53], its energy gap $E_G = 1.17$ eV and the density-of-states effective masses of valence and conduction band of $m_v = 0.59m_0$ and $m_c = 1.06m_0$ respectively [44] with m_0 the free electron mass. The surface state density is assumed to be negligible. Calculations were performed at $T = 4.5$ K. Fig. 2.7c) shows a contour plot of the electrostatic potential with equipotential lines from 0.25 V to 2 V spaced by 0.25 V. The potential contour at 2 V follows the tip shape. The red line marks the silicon ($z > 0$) vacuum ($z < 0$) interface. A considerable amount of the voltage drops inside the silicon sample. In Fig. 2.7d) we present the electrostatic potential distribution along the central axis (blue line in Fig. 2.7c)) for various donor concentrations and for a tip potential of $U = \pm 2$ V. For positive bias of $U = 2$ V, the semiconductor is in depletion. For low donor concentration of $N_D = 10^{15}$ cm^{-3} the depletion layer extends far into the semiconductor and only 56 % of the voltage drops across the vacuum gap resulting in a potential of $U_{bb} = 0.88V$ at the point on the surface directly opposite to the tip. U_{bb} is a measure of the band-bending at the surface and is obviously bias dependent. The value of U_{bb} is only weakly dependent on temperature. At $T = 300$ K we also obtain $U_{bb} = 0.88V$ within the numerical accuracy. The reason is that the ionization of donor impurities is not thermally activated here. The depletion width and the value of U_{bb} reduce with increasing doping, since the increased number of available donors screens the electric field of the tip more efficiently. When the tip is at a negative bias $U = -2$ V, the semiconductor is in accumulation. The width of the accumulation layer only slightly depends on doping. The curves for $N_D = 10^{15}$ and 10^{19} cm^{-3} almost coincide. The accumulation layer is much more efficient in screening the electric field from the tip than the depletion layer. More than 94 % of the potential drops across the vacuum gap. We also clearly see that the width of the accumulation layer is much smaller than the width of a typical depletion layer.

Band-bending may already occur when no bias is applied. This is the case, when tip and sample have different workfunctions. Since sample and tip are in electrical contact, their Fermi levels align in thermal equilibrium. When $\phi_m > \phi_s$, in order to establish thermal equilibrium, electrons will flow from the semiconductor to the metal resulting in a depletion layer accompanied by an upward band-bending at the surface as shown in Fig. 2.8a). Here χ is the electron affinity at the semiconductor surface measured from the bottom of the conduction band E_c to the vacuum level E_{vac} and I the ionization energy. When $\phi_m < \phi_s$ as is the case in Fig. 2.8b) a downward band-bending results. Here the workfunction of the semiconductor has been modified by modifying its Fermi level via doping. For a p-type semiconductor doped with acceptor impurities, having its acceptor levels located 46 meV above the valence band edge for boron impurities [48], majority carriers are holes. Downward band-bending at the surface causes all acceptor states to be filled by bulk electrons, resulting in a negative space charge layer due to ionized acceptor impurities. Since

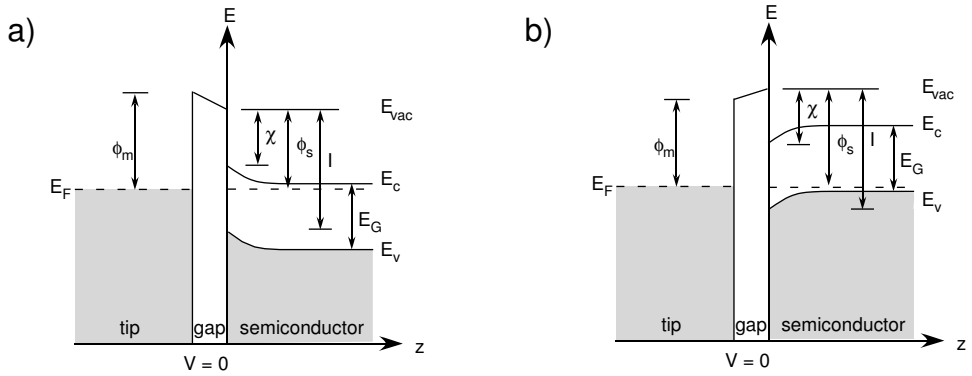

Figure 2.8: Band-bending for a a) n-type and b) p-type semiconductor, when tip and sample have different workfunctions.

the number of mobile hole carriers is reduced at the surface, one speaks of a hole depletion layer.
The workfunction of the Si(111)-(7×7) surface is $\phi_s = 4.6$ eV [54] irrespective of the doping. This phenomenon is due to Fermi level pinning, discussed afterwards, caused by the presence of a high density of surface states not considered in Fig. 2.8. The workfunction of polycrystalline W, used for the tip, is also $\phi_m = 4.6$ eV [29]. Thus no band-bending is expected for the Si(111)-(7×7) surface due to workfunction mismatch.

A third mechanism leads to band-bending at the surface. This is caused by the presence of surface states. Here we have to take into account intrinsic surface states, due to surface reconstructions, but also extrinsic surface states, due to defects. Surface states may have acceptor (neutral when empty, negatively charged when filled with electrons) or donor character (neutral when filled with electrons, positively charged when empty). However, this distinction is somewhat artificial, because surface states may change their character when changing for example the bulk doping. The associated positive or negative net charge in the surface state must be compensated by a space charge layer at the surface of opposite sign which causes the band-bending. When the surface state density N_S is much larger than the bulk impurity density at the surface $N_D^{2/3}$, the Fermi level at the surface is said to be pinned, i.e. it is independent of the bulk doping.
Central to the concept of surface state induced band-bending is the charge neutrality level (CNL). It is defined as the Fermi level position that produces zero net surface charge for an undoped semiconductor at $T = 0$ K measured with respect to the valence band maximum [55]. The definition of the CNL makes the tacit assumption that the energy levels of surface states are referenceable to the bulk bands. If the Fermi level is lower than the CNL, the surface region has a positive net charge. If the Fermi level is above the CNL the surface has an excess of electrons and is negatively charged. In Fig. 2.9a) the situation for a n-type semiconductor in the presence of surface states is shown. Here the CNL (not drawn) is slightly above E_F resulting

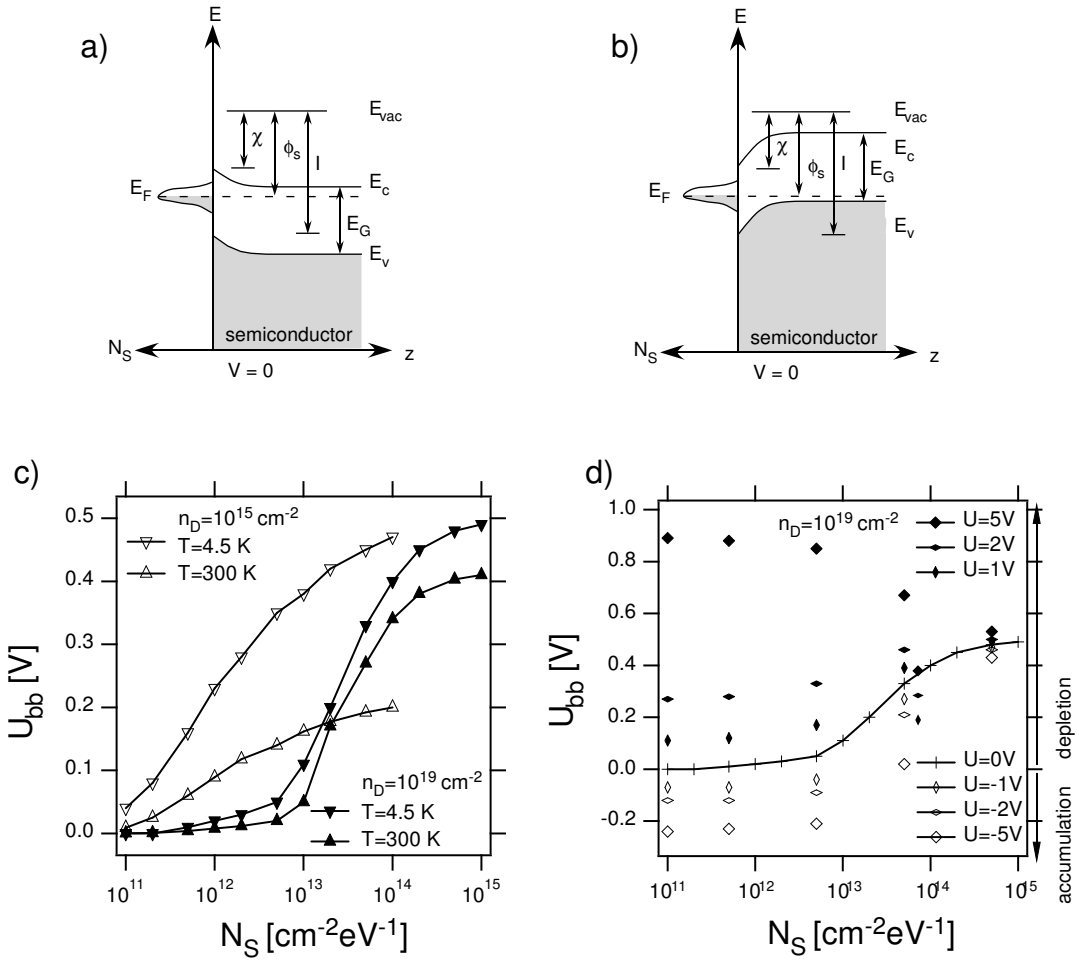

Figure 2.9: Band-bending for a a) n-type and b) p-type semiconductor in the presence of surface states. In c) the surface state induced band-bending U_{bb} of Si(111) is plotted as a function of the surface state density n_S for two different phosphor concentrations n_D and temperatures. In d) the bias dependence of the total band-bending U_{bb} due to surface states and induced by the tip is presented at $T = 4.5$ K.

in a net negative charge at the surface. This negative charge is compensated by a positive space charge layer induced by an upward bending of the bulk bands beneath the surface.

For Si(111)-(7×7) the Fermi level is pinned 0.65 eV above the valence band maximum at the surface irrespective of the type and amount of bulk doping [56, 57]. For a donor density of $n_D = 10^{17}$ cm^{-3}, the Fermi level, as determined from a bulk calculation, is 1.02 eV at 300 K (1.15 eV at 4.5 K) above the valence band maximum in the bulk. Thus the band-bending, obtained by taking the difference between the bulk Fermi energy and the CNL, is 0.37 eV (0.60 eV) for this case (see Fig. 2.9a) for a sketch). For $n_D = 10^{19}$ cm^{-3}, the Fermi level is located at 1.12 eV at 300

K (1.15 eV at 4.5 K) and consequently the bands are bend by 0.47 eV (0.60 eV). The increased band-bending indicates that there is more negative charge in the surface state. For p-type semiconductors as shown in Fig. 2.9b) the bands are bent downwards, since the Fermi level at 0.13 eV is now positioned below the CNL. The bend-banding of -0.52 eV compensates the positive net charge in the surface state. These consideration assume that the surface state density is large enough to pin the Fermi level.

In order to determine the surface state density of the Si(111)-(7×7) reconstruction, knowledge about its atomic structure is required. Details on the generally accepted DAS model for Si(111)-(7×7) are given in section 3.3. The DAS model contains 12 adatoms, 6 restatoms and one corner hole atom, each carrying a broken bond containing one electron. Energy minimization causes a transfer of 7 out of the 12 adatom electrons to the restatoms and the corner hole atom. So the restatom and corner hole atom states are completely filled and carry thus no net charge. The 5 remaining electrons of the adatoms are distributed over the 2×12 adatom states, the factor of 2 takes into account the spin degeneracy. For simplicity we assume here that all adatom states are equivalent and thus degenerate.[2] These states form a surface band with some dispersion. LDA predicts an overall bandwidth of the order of 0.4 eV [58]. The surface area of a Si(111)-(7×7) unit cell is 625.81 Å^2. Thus the surface state density is $N_S = 2 \cdot 12/(625.81\mathring{A}^2 \cdot 0.4eV) = 3.84 \times 10^{14}$ cm^{-2}eV^{-1}.

The density of extrinsic surface states, arising due to defects and disorder, may be roughly estimated by inspection of STM images [51]. These states produce surface charging, which leads to the observed spectral shifts. However, for Si(111)-(7×7) the density of extrinsic surface states[3] is much lower than the corresponding intrinsic surface state density and may be neglected.

Fig. 2.9c) presents theoretical results from a calculation for the Si(111) surface at zero bias $U = 0$ V. The CNL was placed 0.65 eV above the valence band maximum. Here the surface state induced band-bending U_{bb} is plotted as a function of intrinsic surface state density N_S for two different values of the bulk phosphorus doping N_D. We assumed a flat surface state density distributed uniformly between the valence band maximum and the conduction band minimum. For low values of N_S the surface state induced band-bending U_{bb} is small. In this regime, N_S is negligible compared to $N_D^{2/3}$ and the physics is dominated by the bulk doping. For a high surface density, U_{bb} saturates at a value U_{bb}^{sat}. This value can be estimated by taking the difference between the bulk Fermi energy and the CNL. For $N_D = 10^{15}$ and 10^{19} cm^{-2}, the bulk Fermi level is 1.14 (0.86) and 1.15 (1.07) eV above the valence band maximum at $T = 4.5$ K (300 K). Thus U_{bb}^{sat} is 0.49 (0.21) and 0.50 (0.42) eV in agreement with Fig. 2.9c). In this regime the surface state density is so high, that the Fermi level at the surface does not depend on bulk doping anymore. This is the origin for Fermi level pinning. In the intermediate surface state density

[2]This is not the case due to the stacking fault and the separation of adatoms in center adatoms and corner adatoms (see Fig. 2.4).

[3]For Ge(111)-c(2×8) the extrinsic surface state density is of the order of 10^{13} cm^{-2} [51].

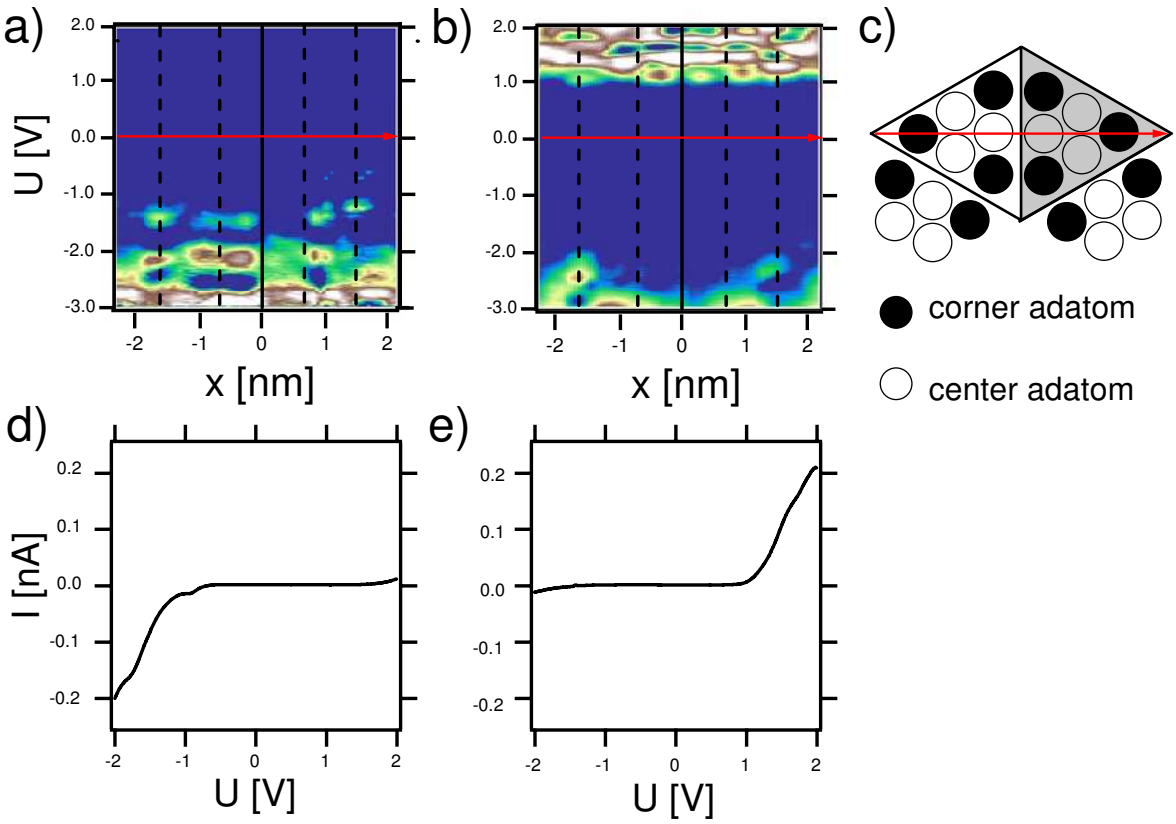

Figure 2.10: Comparison between STS measurements on Si(111)-(7×7) at T = 4.5 K. a) Phosphor doped n-type sample with a room temperature resistivity of 0.001-0.005 Ωcm corresponding the $N_D = 1 - 5 \times 10^{19}$ cm^{-2}. U=-3V, I=0.2 nA. b) Boron doped p-type sample with a room temperature resistivity of 0.022 Ωcm corresponding the $N_A = 3 \times 10^{18}$ cm^{-2}. U=2V, I=0.2 nA. c) Sketch of the Si(111)-(7×7) unit cell. The STS spectra were measured along the red arrow. Averaged I(V) characteristics for d) phosphorus and e) boron doped sample.

regime, band-bending strongly depends on bulk doping. Inspection of Fig. 2.9c) shows that the band-bending is less pronounced at higher bulk doping again due to the enhanced screening capabilities of the space charge layer. For Si(111)-(7×7) with $N_S = 3.84 \times 10^{14}$ cm^{-2}eV^{-1} we are clearly in the pinning regime.
In Fig. 2.9d) we study what happens when a bias is applied to the STM tip in the presence of surface states. For small values of N_S we recover the same results as for the situation without surface states. For $N_S > 10^{13}$ cm^{-2}eV^{-1} screening of the electric field from the tip by the surface states becomes efficient and the tip-induced contribution to the total band-bending becomes smaller. For N_S of the order of 10^{15} cm^{-2}eV^{-1} the screening of the tip is so efficient that hardly any tip-induced band-bending is observed. It is important to note that the surface remains in depletion even for a bias of -5 V. This observation has an important consequence for STS

spectroscopy on pinned Si surfaces. When measuring at positive bias, the barrier for electrons tunneling across the depletion layer from the surface state into the bulk is increased. This is expected to attenuate the tunneling current. When measuring at negative bias, the barrier is decreased and the tunneling current is expected to be enhanced. This considerations apply for a n-type sample. For p-type samples the situation is reversed. The surface state induces a hole depletion layer due to the downward bending of bands near the surface. For positive bias the barrier is decreased resulting in enhanced tunneling current. For negative bias the tunneling current is attenuated.

Fig. 2.10 presents experimental STS results on a n-type a) and p-type b) Si(111)-(7×7) surface measured at $T = 4.5$ K along the red arrow shown in the sketch in c). The two STS spectra are radically different. For the n-type phosphorus doped sample in a), clear spectroscopic features are observed at negative bias, whereas for positive bias no signal is observed. The opposite situation is observed for the p-type boron doped sample in b), where clear spectroscopic features are observed for positive bias. The averaged I(V) curves acquired simultaneously with the STS spectra presented in d) for the n-type sample and in e) for the p-type sample show the same asymmetry.[4] The attenuation of the tunneling current is in agreement with the discussion above. However, tip induced band-bending alone cannot explain all the findings. At room temperature no such asymmetry has been observed. The average gap extracted from our I(V) curves exceeds 2 eV and is not in agreement with the metallic character of the Si(111)-(7×7) surface observed at room temperature [43, 56]. This value of the gap measured with STM even exceeds the bulk energy gap of $E_G = 1.17$ eV [44]. The adatom states observed between $U = 1$ and 2 V in Fig. 2.10b) are found centered around 0.5 eV at room temperature [43]. As discussed above, tip induced band-bending becomes very small in the presence of a high density of surface states and cannot explain these shifts.

In order to understand the origin of these inconsistencies we have consulted the literature. Heike *et al.* [59] have explored transport between a n-type Si(111)-(7×7) surface and the bulk at room temperature. They created small patches of isolated Si(111)-(7×7) which are separated from surrounding Si(111)-(7×7) areas by insulating trenches. Topography images recorded at a positive bias of 2V showed clearly that the apparent height on the isolated patch is reduced compared to the surrounding area, whereas the apparent height is approximately the same in both areas for a negative bias of -2V. Applying a negative bias slightly reduces the band-bending at the surface allowing electrons to pass from the surface into the bulk more easily. At positive bias, the band-bending and the depletion barrier between surface and bulk is increased and hinders electrons to pass into the bulk causing the tip to approach the

[4]The I(V) curve in Fig. 2.10d) has been multiplied by a voltage independent normalization factor, simulating a current setpoint of I=0.2 nA at U=-2V, to allow comparison with the curve in e).

surface to maintain the setpoint current.[5] Further Heike *et al.* observed enhanced band-bending at positive bias, causing a significant shift of the spectral features in dI/dV curves and a widening of the apparent gap, whereas band-bending for negative bias was negligible. These observations show that band-bending becomes significant when the surface conductivity is eliminated. All these phenomena are reduced as the size of the isolated Si(111)-(7×7) patch is increased and consequently conduction parallel to the surface dominates. As the area is increased the electrons may travel along the surface until they eventually leak into the bulk trough a leakage path across the depletion layer provided for example by a defect or a step.
Tanikawa *et al.* [60] and Wells *et al.* [61] have measured the electrical surface transport properties of Si(111)-(7×7) using a micro-four-point probe and observed a drop of the surface conductivity of several orders of magnitude with decreasing temperature.[6] The suppression of surface conductivity also eliminates the leakage path through the depletion layer at defect sites. This leads to a non-equilibrium configuration in which the temporarily increased filling of the surface state causes band-bending until tunneling between the surface and the bulk becomes effective [63].
Only a few experimental STM studies focusing on the low-temperature electron transport properties of semiconductor surfaces were reported in the literature and the physical mechanisms behind those results are not completely understood. Dujardin *et al.* [64] investigated clean and H covered Ge(111)-c(2×8) surfaces. The p-type samples used in this study had a Ga concentration of 2×10^{14} cm^{-3} giving a room temperature resistivity of 15 Ωcm. They observed a linear increase of the energy gap with decreasing temperature from 0.2 eV at $T = 300$ K to 0.7 eV at $T = 30$ K ($U = \pm 1.8$ V, $I = 1$ nA). STS spectra obtained by Yokoyama and Takayanagi [65] at $T = 300$, 77 and 5 K on B and Sb doped Si(100)-(2×1) samples with a resistivity of 0.01-0.02 and 0.05-0.09 Ωcm respectively do not exhibit significant peak shifts as a function of temperature ($\pm 0.05V$, $U = 1.5$ V, $I = 0.1$ nA). Lastapis *et al.* [66] reported results on As doped Si(100) samples with a resistivity of 0.004-0.007 Ωcm and B doped Si(100) samples with a resistivity of 0.7 -1.3 Ωcm. The highly doped As sample exhibits a gap of 0.2 eV at $T = 300$ K, increasing to 1 eV at 35 K (U=-1.5 V, I=0.5 nA). For the moderately doped sample with B impurities the gap extends from 1 V down to -5 V at $T = 35$ K rendering it impossible to image the surface at

[5] In Ref. [59], Heike *et al.* observed rectifying behavior enhancing the spectrum for positive bias. However, for positive bias, the band-bending barrier is increased for a n-type sample, thus we would expect attenuation. This is in agreement with the depression seen at positive bias in the topography images, since the tip has to approach the surface for keeping the setpoint current constant. In this work, however dI/dV spectra have been normalized by I/V, which approximately eliminates the dependence on the tunneling transmission factor. Since I is reduced for positive bias at constant height, the positive side of the spectrum is enhanced.

[6] This method measures contributions from the surface states as well as from the space charge layer as indicated by the doping dependence of the conductivity at high temperature. At low temperature however, the conductivity is independent of doping [61] and is thus believed to represent the contributions due to the surface states. Data obtained via a four-tip STM is expected to contain exclusively the contribution to the conductivity from the surface states [62].

negative bias ($U = -7$ V, I=0.5 nA). Feenstra *et al.* [67] studied the dependence of STS spectra of Ge(111)-c(2×8) on the tunneling current setpoint, concluding that if spectral features shift when changing the current setpoint, non-equilibrium effects come into play [55]. The signature of charge transport limitations between surface and bulk is a logarithmic shift of spectral features away from the Fermi level with increasing set-point current [51] being also responsible for the widening of the apparent gap.

Logarithmic shifts have also been observed recently by Mysliveček *et al.* [63] at $T = 7$ K on n-type Si(111) samples with a high As concentration of 1.6×10^{19} cm^{-3}. They observed spectral features at U =-1.3, -0.9, -0.5, 1.2, 1.4 and 1.6 V ($U = 2$ V, $I = 0.1$ nA). Spectral features at 1.2 V and 1.6 V were identified with center adatoms. These states should correspond to the states in our dI/dV maps at 1.46 and 1.77 V from the p-type boron doped sample shown Fig. 2.4a). Corner adatoms states were observed at -0.9, -0.5 and 1.4 V. The state at 1.4 eV is found in our measurements at 1.66 V. Note that our unoccupied adatom states are 0.26 eV above the states observed by Mysliveček *et al.*. In addition we observe a clear corner adatom state at 1.32 V which exhibits different intensity depending on whether the adatom is in the faulted or unfaulted part of the unit cell. Two additional states may be distinguished in our measurement at 1.94 and 1.14 eV, but their localization is less pronounced. In any case, we do not observe the corner adatom states at -0.9 and -0.5 eV, neither do we see the rest atom state seen by Mysliveček *et al.* at -1.3 V. Further investigations are clearly required to fully understand STS data from low temperature measurements.

2.3 Low-energy electron diffraction

Low-energy electron diffraction is a powerful technique used in surface science for obtaining structural information about surfaces. The diffraction of electrons by crystalline surfaces was first demonstrated by Davisson and Germer in 1927 while working at Bell Telephone Laboratories [68]. Their observation was an important fundamental discovery, as it was the first experimental demonstration of the wave nature of the electron predicted by de Broglie. For energies below 300 eV, electron diffraction is particularly suited to surface studies since the inelastic mean free path of only a few Å provides excellent surface sensitivity. Furthermore, since according to the de Broglie relation

$$\lambda = \frac{2\pi}{k} = \frac{h}{p} = \frac{h}{\sqrt{2mE}},$$

typical LEED wavelengths are of the same magnitude as the interatomic distances in solids, LEED can be used to determine the atomic structure of single crystal surfaces in analogy with x-ray diffraction. The method is applied both to check the crystallographic quality of a freshly prepared surface and as a mean of obtaining new information about atomic surface structure.

In a typical LEED experiment, electrons emitted from an electron gun situated behind a hemispherical fluorescent screen are accelerated to an energy E and hit the sample after passing through a hole in the center of the screen (see Fig. 2.11a) for a sketch). The sample is placed in the center of the hemisphere so that all back-diffracted electrons travel towards the screen, held at a large positive potential. Before the electrons hit the screen they have to pass a retarding field energy analyzer consisting of four hemispherical grids, mounted concentrically with the screen, blocking inelastically scattered electrons from the screen. Since the fluorescent screen is transparent, diffraction spots due to elastically scattered electrons can be observed through a view-port behind the screen, where only the electron gun assembly slightly obstructs the view in the center of the screen.

Fig. 2.11b) and c) show experimental LEED patterns of the Si(111)-(7×7) and the Si(100)-(2×1) reconstruction recorded by taking a picture of the fluorescent screen with a digital camera. The symmetry of the diffraction pattern provides direct information about the symmetry of the surface. However, one should note that the atomic structure of the surface can have at most the symmetry indicated by the LEED pattern. Fig. 2.11b) for example may suggest a six-fold rotational symmetry for the Si(111)-(7×7) reconstruction. However, by measuring LEED patterns at different energies one finds that the LEED pattern is only three-fold symmetric. Another example is provided by the LEED pattern for Si(100)-(2×1) in Fig. 2.11c). Here one may expect a four-fold symmetric surface. However, the Si(100)-(2×1) reconstruction is only two-fold symmetric and the apparent four-fold symmetry stems from the incoherent addition of two orientational domains.

The mere existence of a sharp spot pattern already implies the existence of a well-ordered surface characterized by lattice vectors $\mathbf{a}_1$ and $\mathbf{a}_2$. Translational invariance

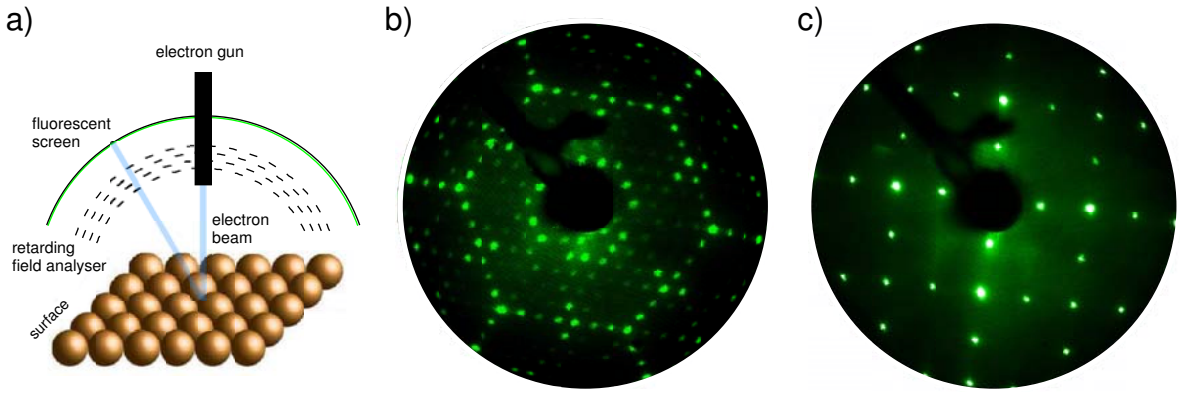

Figure 2.11: a) Sketch of the LEED geometry. b) LEED pattern of the Si(111)-(7×7) reconstruction at $E = 60$ eV. c) LEED pattern of the two-domain Si(100)-(2×1) reconstruction at $E = 78$ eV.

in two dimensions ensures that diffraction occurs when the two-dimensional Laue condition is satisfied.

$$(\mathbf{k}_i^{||} - \mathbf{k}_r^{||}) = \mathbf{G}(h,k)$$

where $\mathbf{k}_i^{||}$ and $\mathbf{k}_r^{||}$ are the parallel components of the wavevector of the incident and reflected electrons and $\mathbf{G}(h,k) = h\mathbf{b}_1 + k\mathbf{b}_2$ a linear combination of the reciprocal surface lattice vectors $\mathbf{b}_1$ and $\mathbf{b}_2$. The integer numbers (h,k) are used as indices to label the spots. Since the diffraction pattern corresponds to the surface reciprocal lattice, measurement of spot distances combined with a simple transformation

$$\mathbf{a}_i \cdot \mathbf{b}_j = 2\pi\delta_{ij}$$

yields the periodicity in real space. The perpendicular component $k_r^{\perp}$ of the back-diffracted electrons is defined by energy conservation

$$k_r^{\perp} = \sqrt{\frac{2mE}{\hbar^2} - \mathbf{k}_r^{||2}}.$$

This equation also limits the set of observable LEED spots by the condition that the expression inside the square root must be greater or equal to zero.
In many cases, the unit cell at the surface is larger than expected from the bulk-truncated surface, which leads to additional satellite spots in the LEED pattern for which fractional indices are used. The lattice vectors $\mathbf{A}_1$ and $\mathbf{A}_2$ of such superstructures can be expressed as multiples of the (1×1) surface vectors $\mathbf{a}_1$ and $\mathbf{a}_2$,

$$\begin{pmatrix} \mathbf{A}_1 \\ \mathbf{A}_2 \end{pmatrix} = \begin{pmatrix} m_{11} & m_{12} \\ m_{21} & m_{22} \end{pmatrix} \begin{pmatrix} \mathbf{a}_1 \\ \mathbf{a}_2 \end{pmatrix},$$

where the m_{ij} are the coefficients of the superstructure matrix. The position and indices of the additional LEED spots can be calculated directly from

$$\begin{pmatrix} \mathbf{B}_1 \\ \mathbf{B}_2 \end{pmatrix} = \frac{1}{m_{11}m_{22} - m_{12}m_{21}} \begin{pmatrix} m_{22} & -m_{21} \\ -m_{12} & m_{11} \end{pmatrix} \begin{pmatrix} \mathbf{b}_1 \\ \mathbf{b}_2 \end{pmatrix}.$$

A less general way to describe superstructures is the Wood notation [69], where the length of the vectors $\mathbf{A}_1$ and $\mathbf{A}_2$ are specified in units of $\mathbf{a}_1$ and $\mathbf{a}_2$ together with the rotation angle α between $\mathbf{A}_1$ and $\mathbf{a}_1$ (only specified if non-zero)

$$p/c\Big(\frac{|\mathbf{A_1}|}{|\mathbf{a_1}|} \times \frac{|\mathbf{A_2}|}{|\mathbf{a_2}|}\Big) R\alpha.$$

The letters p and c indicate a primitive and a centered surface unit cell respectively. The letter p is usually omitted unless needed for clarity.

2.4 Dynamical low-energy electron diffraction

LEED may also be used for the determination of atomic coordinates by measuring the diffracted intensities I as a function of acceleration voltage V or beam energy $E = eV$. This method is called dynamical LEED or IV-LEED. In any diffraction experiment, phase information is lost, as one measures intensity rather than amplitude, so that direct Fourier inversion of the data does not simply return the structure. Structure determination from LEED is further complicated by the fact that unlike x-rays, electrons undergo multiple elastic scattering at the surface. LEED analysis usually proceeds via a trial-and-error process: first a plausible trial structure is postulated, simulated $I(V)$ curves based on computer modeling of the multiple scattering process are calculated, and these are compared to the experimental $I(V)$ curves, using a reliability factor (R-factor), as a quantitative measure of the goodness of fit. The trial structure is further refined until the R-factor is optimized. The minimum R-factor value is then compared with those obtained by refining different trial structures until satisfactory agreement is achieved.

Standard experimental setups for collecting $I(V)$ curves use video cameras for collecting images of the fluorescent screen for each energy. In conventional video cameras images are acquired at a rate of 50-60 Hz, requiring averaging of several images in order to obtain a satisfying signal-to-noise ratio. In our home-build setup LEED intensity measurement were carried out using a calibrated 12-bit CCD camera with single-stage Peltier cooler which allows exposure times up to several seconds, avoiding multiple readout noise encountered in conventional video LEED systems [71]. The acquisition software is interfaced with the LEED optics controllers allowing to synchronize sequentially acquisition of images and incrementation of the beam energy. Data collection is mostly performed at normal incidence with respect to the incident electron beam. In our setup, a manipulator with a polar rotational axis allows off-normal measurements. Normal incidence conditions can be adjusted to within a few tenth of a degree by checking that the $I(V)$ curves of equivalent spots are identical. For this purpose a second rotational axis would be highly desirable. In our setup a four-point port aligner allows a fine adjustment of the electron gun orientation with respect to the sample.

Images are stored on a hard disk and analyzed in a second round by our own data analysis package. In a first step all images are assembled into a 3D data cylinder $I(x, y, E)$, here x and y represent the parallel-projected coordinates of a point on the fluorescent screen. Subsets of data may now be extracted and visualized in various ways. Vertical cuts $I(r, E)$ as shown in Fig. 2.12a) along a line $r = \sqrt{x^2 + y^2}$ on the screen, measured in units of the screen radius R, allow to observe the intensity variation of several spots as a function of energy. Usual images of the LEED pattern are recovered by extracting horizontal cuts $I(x, y)|_E$ at fixed energy (Fig. 2.12b). When increasing the energy E of the incident electrons, their wavevector $\mathbf{k}_i^2 = 2mE/\hbar^2$ is increased. At normal incidence $\mathbf{k}_i^{||} = 0$, the Laue condition $\mathbf{k}_r^{||} = \mathbf{G}(h, k)$ does not allow $\mathbf{k}_r^{||}$ to be modified in order to observe a LEED spot. Thus only the component $k_r^{\perp}$ perpendicular to the surface will increase as shown in Fig. 2.12c) causing the spots to converge towards the (0,0) spot as can be seen from the data in Fig.2.12a). Although the functional dependence of the spot position on the screen with energy is known ($E \propto r^{-2}$), the extraction of LEED intensities along a predefined path is tempting but not very accurate. Field inhomogeneities due to the LEED optics or external stray fields cause the electrons to slightly deviate from their ideal path as can be seen from Fig. 2.12b). In our data analysis package we have implemented a spot tracking procedure, which fits a 2D Gaussian to a selected spot on a LEED pattern extracted at a selected energy E_n. The fitted position (x_n, y_n) is then used as initial value (x_{n+1}, y_{n+1}) for the fit at the next energy E_{n+1}. In order to determine the intensity of a spot at a given energy, the values of all pixels within a disk of radius R_1 centered on the spot center are integrated and divided by the disk surface πR_1^2. The background is taken into account by subtracting the sum of all pixels on a ring with inner radius R_1 and outer radius R_2 divided by the ring surface.
In Fig. 2.12d) we compare our experimental normal incidence $I(V)$ curves for integer spots of Si(111)-(7×7) with experimental curves from the $I(V)$ curve repository of Jona's group at Stony Brook University [70]. We have plotted all of the equivalent $I(V)$ curves. Slight variations from curve to curve are due to small residual deviations from the normal incidence condition. Although our curves exhibit an overall shift of approximately 3 eV to higher energies, the two data sets are in excellent agreement. In any case, when comparing experimental and simulated data, an overall shift of all spectra does not influence the final structure, since the R-factor is usually computed by shifting the energy of experimental and theoretical curves with respect to each other until an optimum value is achieved. The shift actually acts as a correction for any non-optimum value of the real part of the optical potential V_{or}, which needs therefore not be optimized by the search algorithm.

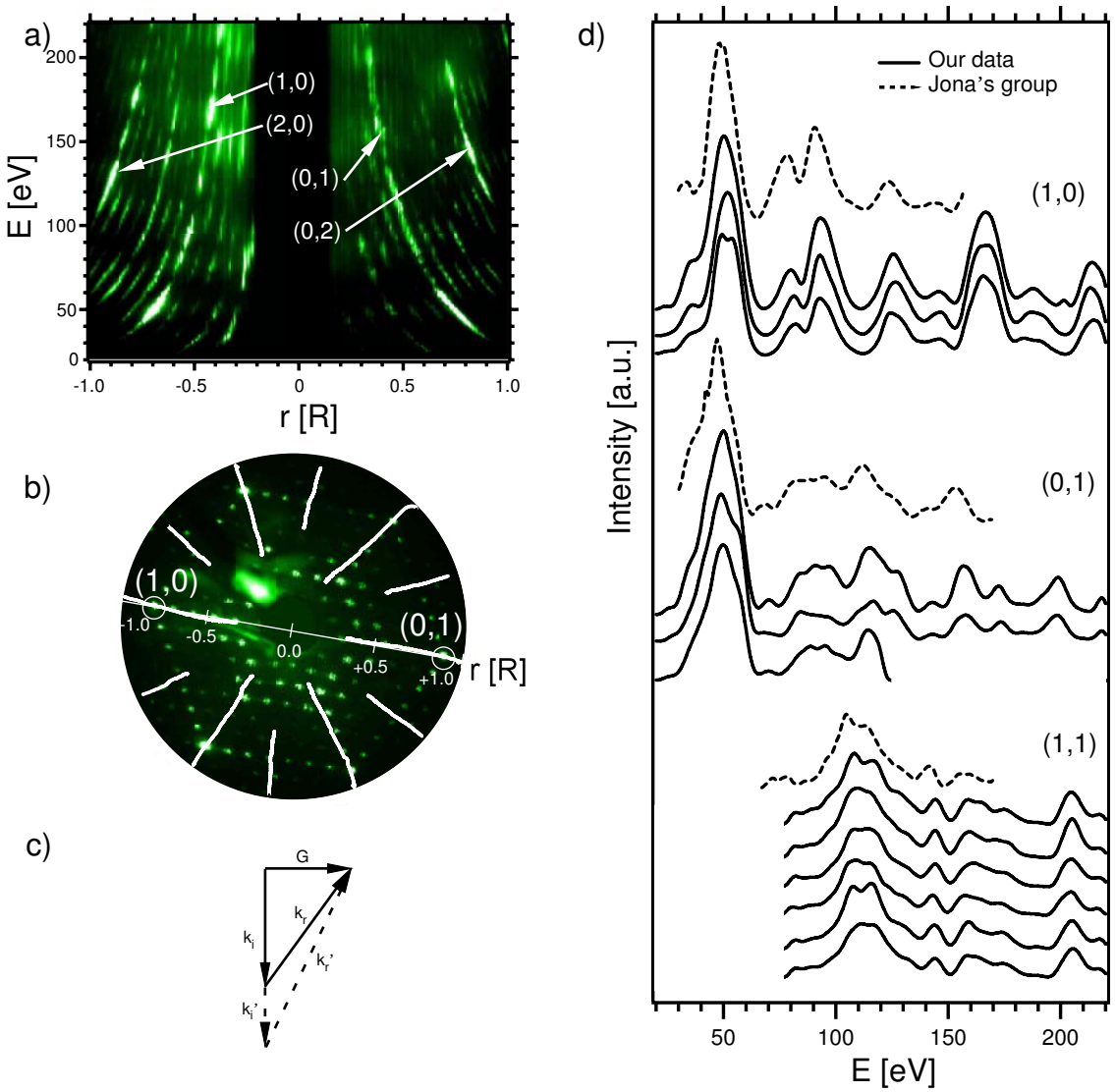

Figure 2.12: IV-LEED data of Si(111)-(7×7): a) IV-LEED map along the (1,0) direction. b) LEED pattern at $E = 35$ eV with the spot paths superimposed. The corresponding $I(V)$ curves are shown in d). c) Sketch of the effect of increasing the energy. Spots move towards the center of the screen. d) Comparison between experimental $I(V)$ curves from our setup and from Jona's group [70].

2.5 Multiple scattering calculations

For the calculation of LEED intensities one usually uses the muffin tin approximation. Within this approximation the crystal is divided into non-overlapping spheres, called the muffin tins, centered on the atomic nuclei, and an interstitial region. Inside the muffin tin the potential is supposed to be spherically symmetric, whereas the potential in the interstitial region is constant. The muffin tins are characterized by a set of phase shifts $\delta_l(E)$, one for every value of the energy E and angular momentum l of the incident electron. Since an elastic scattering event only alters the phase of the electron wavefunction, knowing the phase shifts of each element in the structure, one can predict what will come out from what goes in [72]. Since the potential acting on the electron inside the muffin tin is spherically symmetric, the radial component of the electron wavefunction and consequently the phase shift can not depend on the z-component of the angular momentum m.
Phase shifts required for a LEED calculation may be computed using the Barbieri/van Hove phase shift package [20]. In a first step the charge density of each element (see Fig. 2.13a) must be determined by solving the free atom Dirac-Fock equation, the relativistic analogue of the Hartree-Fock equation, in a self-consistent way. In a second step the atomic charge densities are superimposed in order to obtain the charge density for the crystal structure of interest. For the purpose of obtaining phase shifts for a LEED calculation it is not necessary to know the exact position of the atoms in the structure, because the phase shifts and therefore the calculated intensities are not strongly dependent on the manner in which the phase shifts are obtained. However, one may iterate the phase shift calculation after the LEED structure analysis to further refine the structure. The muffin tin potential is then obtained by adding the electrostatic potential, computed from the charge density via the Poisson equation, and a Slater like exchange term (see Fig. 2.13b). The final potential is shifted to set its zero to the average energy in the interstitial region (muffin tin zero). Due to the presence of the vacuum in a slab calculation, the average energy in the interstitial region is highly distorted. Therefore one first performs a bulk calculation for the substrate to determine its muffin tin zero and then performs a slab calculation with the muffin tin zero from the bulk. Finally the phase shifts are determined by solving the Dirac equation for the muffin tin potential. Phase shifts calculated for bulk Si using two different muffin tin radii $R_{MT} = 2.2$ and 1.8 Bohr are shown in Fig. 2.13c) along with Moruzzi phaseshifts ($R_{MT} = 2.2$ Bohr) distributed with the Barbieri/van Hove phasehift package [20]. Our phaseshifts calculated using $R_{MT} = 2.2$ Bohr which actually corresponds to the Si-Si nearest neighbor distance in bulk Si, slightly deviates from the Moruzzi phaseshifts. The set of phaseshifts calculated using $R_{MT} = 1.8$ Bohr agrees better with the ones from Moruzzi. Decreasing the muffin tin radius tends to reduce the phaseshifts except for the $l = 0$ component. It is not clear, how the Moruzzi phase shifts were calculated. Older calculations often did not take into account relativistic corrections due to the limited computational resources.

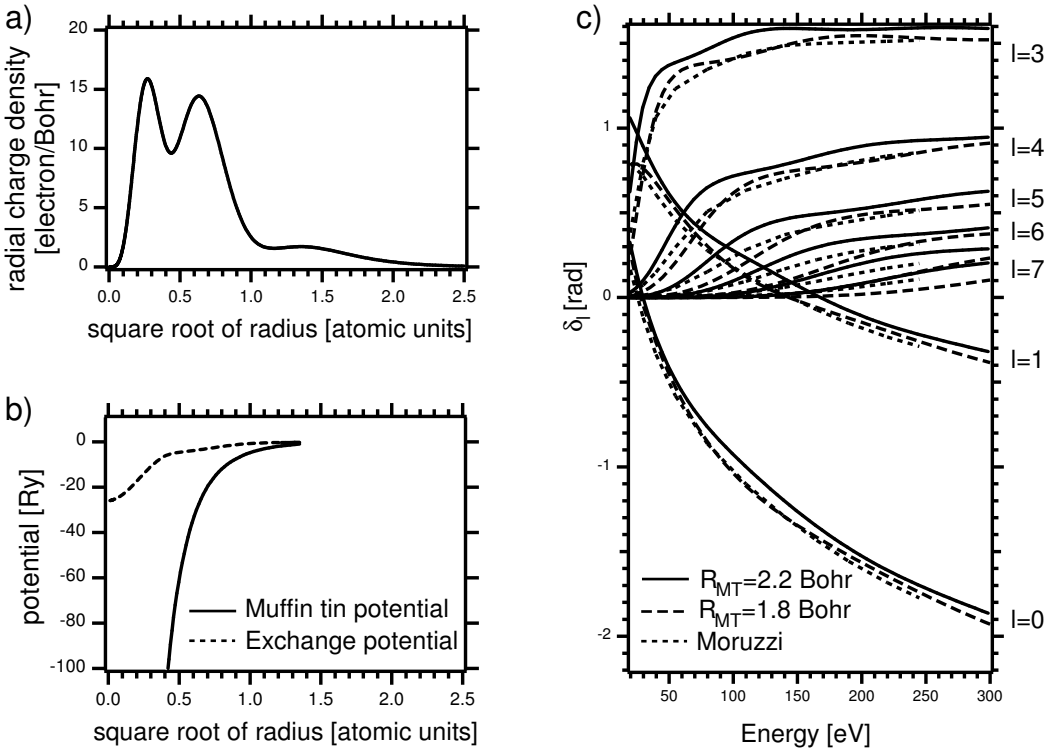

Figure 2.13: a) Radial atomic charge density of Si. The graph shows r^2 times the charge density. b) Muffin tin and exchange potential of Si in bulk Si calculated using $R_{MT} = 1.8$ Bohr. The electrostatic potential is given by the difference between the muffin tin and the exchange potential. c) Comparison between our bulk Si phaseshifts calculated with $R_{MT} = 2.2$ and 1.8 Bohr and the ones from Moruzzi [20].

For the computation of theoretical $I(V)$ curves we apply fully dynamical scattering theory as implemented in the CLEED package developed by Held [21] using the combined space method of Tong and van Hove [73, 74] together with the layer doubling scheme as described by Pendry [72]. Within the combined space method, the semi-infinite crystal is divided into layers of atoms. Adjacent layers having small interlayer separation are combined into a subgroup. For each subgroup the scattering matrices are calculated using spherical harmonics. Results for each subgroup are transformed to a plane wave representation. The multiple scattering problem between subgroups and simple crystal layers separated by larger interlayer spacings are solved using plane waves by layer doubling. Layer doubling generates the exact solution of forward and back layer-scattering matrices for two layers. The procedure is then repeated for four, eight, etc layers until convergence is reached. The converged scattering matrices are finally used to evaluate the LEED amplitudes.
The input for CLEED contains a set of coordinates for the surface structure and the angles of incidence of the electron beam. Temperature effects are taken into account via a Debye-Waller factor. The program allows to attribute individual anisotropic

root mean square displacements for each atom. Further the value for the optical potential V_o must be specified. The optical potential is in general non-Hermitian taking into account loss of intensity through inelastic scattering processes. As mentioned before the real part of the optical potential V_{or} only causes the $I(V)$ curves to shift in energy. The imaginary part V_{oi} produces absorption of the elastically scattered beam and causes broadening of structures in the $I(V)$ curves. V_{oi} is not a crucial parameter in structural analysis [21,72]. It changes peak width and intensity but has weak influence on peak positions on which we rely mostly for structural information. V_{oi}, which determines the mean free path of the electrons, is however an important convergence parameter for the layer doubling routine [21].
Theoretical $I(V)$ curves are compared to the experimental spectra via a R-factor. The problem with the visual evaluation is that it is not objective, not quantitative and cannot handle properly and weigh large amount of information [75]. The requirements for a R-factor are that it is chiefly sensitive to peak positions, it should not at all be sensitive to absolute intensities, but should pay attention to relative intensities of features that are close in energy. Several R-factors have been proposed in the literature [76]. One of the most common one is the Pendry R-factor R_p [77] defined by

$$R_p = \frac{\int (Y_{th} - Y_{exp})^2 dE}{\int (Y_{th}^2 + Y_{exp}^2)^2 dE}$$

with

$$Y = \frac{L}{1 + L^2 V_{oi}^2},\ L = \frac{I'}{I},\ I' = \frac{dI}{dE}.$$

For a perfect match between theory (th) and experiment (exp) $R_p = 0$, when no correlation exists between the two $R_p = 1$. R_p is clearly independent on an overall normalization factor since $L = \frac{I'}{I} = \frac{J'}{J}$ with $J = cI$. In order to add up R-factors from different spots $\mathbf{G}(h,k)$, van Hove [76] suggests to weight different beams proportionally to the energy range ΔE

$$R_p = \frac{\sum_{\mathbf{G}} R_{p,\mathbf{G}} \Delta E_{\mathbf{G}}}{\sum_{\mathbf{G}} \Delta E_{\mathbf{G}}}.$$

As mentioned before the R-factor determined by CLEED is the optimum value achieved by shifting the energy of the experimental and theoretical curves with respect to each other.
The CLEED package performs automatic structure optimization. It uses standard optimization algorithms [78] for the simultaneous refinement of structural parameters. Within each search step a set of geometrical parameters is chosen by the algorithm depending on the R-factor values achieved in prior runs and in accordance with the specified symmetry constraints.
In Fig. 2.14a) we compare experimental and calculated I(V) curves for the Si(100)-(2×1) reconstruction. Si(100)-(2×1) serves here as a test case allowing us to check the reliability of our experimental LEED setup and of our analysis methods. The

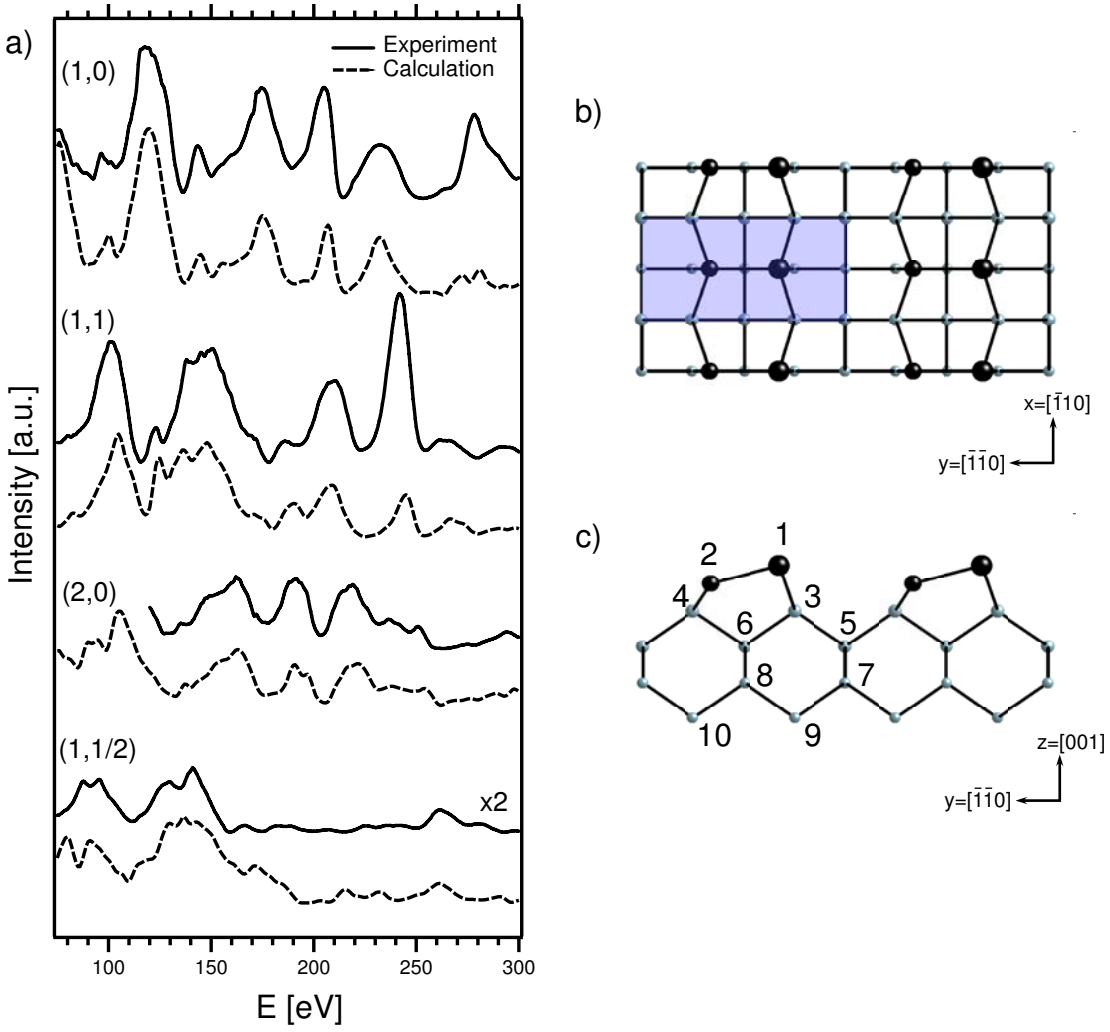

Figure 2.14: a) Comparison of experimental and calculated I(V) curves of Si(100)-(2×1). Top b) and side (c) view of the buckled dimer model. The (2×1) unit cell is shown in blue. The numbers allow identification of atoms in Tab. 2.1.

calculation was performed within a buckled dimer model with (2×1) periodicity shown in Fig. 2.14b) and c) (see also section 3.2 for details about the model). All three coordinates of the two dimer atoms as well as the eight atoms of the first four substrate layers were included in the optimization process. In order to take into account the presence of two orientational domains rotated with respect to each other by 90^o as well as the presence of adjacent oppositely buckled dimers, the following sets of simulated I(V) curves were added incoherently before comparison with experiment:

$$(1,0) + (0,1) + (-1,0) + (0,-1)$$
$$(1,1) + (1,-1) + (-1,1) + (1,1)$$
$$(2,0) + (0,2) + (-2,0) + (0,-2)$$

Si atom	x[Å]	y[Å]	z[Å]
1	1.88(1.92*)[0.04]	2.60(2.66)[0.06]	6.97(6.97*)[0.00]
2	2.18(1.92*)[0.26]	4.90(4.79)[0.11]	6.23(6.28)[0.05]
3	0.01(0.00*)[0.01]	2.22(2.23)[0.01]	5.55(5.54)[0.01]
4	0.13(0.00*)[0.13]	5.58(5.71)[0.13]	5.47(5.53)[0.06]
5	0.04(0.00*)[0.04]	0.39(0.00*)[0.39]	4.28(4.34)[0.06]
6	-0.24(0.00*)[0.24]	3.66(3.84*)[0.18]	3.90(3.96)[0.06]
7	1.97(1.92*)[0.05]	-0.28(0.00*)[0.28]	2.95(2.89)[0.06]
8	2.12(1.92*)[0.20]	3.91(3.84*)[0.07]	2.53(2.63)[0.10]
9	1.82(1.92*)[0.10]	1.96(1.84)[0.12]	1.41(1.40)[0.01]
10	1.79(1.92*)[0.13]	5.92(5.83)[0.09]	1.40(1.36)[0.04]

Table 2.1: Comparison of optimized structural parameters for the Si(100)-(2×1) reconstruction. The first values in the table are from our analysis, the values in parentheses are from Ref. [79]. The values in brackets give the absolute difference between the two set of coordinates. Fixed parameters are marked with an asterisk.

$$(1, 1/2) + (1, -1/2) + (-1, 1/2) + (-1, -1/2)$$

This approximation is sufficient to take into account the large-sized orientational domains, but neglects interference between oppositely buckled dimers. For the calculation we used the Moruzzi phase shifts for Si distributed with the Barbieri/van Hove phasehift package [20] including phaseshifts up to $l = 8$. For the imaginary part of the optical potential we used $V_{oi} = 3$ eV. We find that increasing the value of V_{oi} damps the spectrum by an equal factor over the entire energy range. Calculations were carried out at $T = 0$ K. Increasing the temperature tends to damp the high energy part of the spectrum more strongly than the low energy part. However, the calculation at $T = 0$ K already seems to overestimate the damping at high energy. The agreement between experiment and theory quantified by an R-factor of $R_p = 0.18$ is quite good. This value may be compared to $R_p = 0.26$ and 0.30 for two different experimental datasets obtained by Over *et al.* in Ref. [79]. However, in this work not all structural parameters were allowed to relax. The optimized coordinates are compared in Tab. 2.1. The z values agree nicely. It is interesting to note that especially for the lateral parameters which were fixed in Ref. [79] significant differences to our values occur.

It is important to note that the simplified asymmetric dimer model with (2×1) periodicity does not capture all the physics, since all dimers have the same orientation. A more recent IV-LEED study [80] at low temperature takes into account pairs of oppositely buckled dimers resulting in a c(4×2) periodicity.

2.6 Angle-resolved photoemission

Angle-resolved photoelectron spectroscopy (ARPES) allows to experimentally map the dispersion of occupied electronic states. The surface is irradiated with monoenergetic photons and the emitted photoelectrons are analyzed with respect to their kinetic energy and emission angles (see Fig. 2.15a)). A rigorous theoretical description of the photoemission process requires a full quantum-mechanical treatment within the one-step model [81]. Within the less accurate, but more instructive three-step model the photoemission process is separated into three independent steps.
1) Optical excitation of an electron from an initial to a final state inside the crystal
2) Propagation of the excited electron to the surface
3) Emission of the electron from the solid into the vacuum
The independent treatment of these three contributions leads to a simple factorization of the corresponding probabilities in the photoemission current.
An electron initially residing in a state with binding energy E_B is knocked out by a photon of energy $h\nu$. E_B is measured with respect to the Fermi energy E_F (see Fig. 2.15b)). In a first approximation only direct transitions with nearly unchanged wavevector $\mathbf{k}$ are taken into account. During their journey to the surface, a large number of photoelectrons undergoes inelastic scattering processes and contributes to the continuous secondary electron background. The probability that a photoelectron arrives at the surface is proportional to the mean free path λ. The value of λ of typically 5 to 20 Å [29] is responsible for the intrinsic surface sensitivity of ARPES. However, a description using the mean free path is simplified and does not describe complicated multiple scattering phenomena accurately. During transmission across the surface, the photoexcited electron is scattered by the inner optical surface potential V_o, which has only two-dimensional translational symmetry. This implies that only the component of the wavevector parallel to the surface is conserved

$$\mathbf{k}^s_{||} = \mathbf{k}^v_{||} \tag{2.3}$$

Here $\mathbf{k}^s_{||}$ and $\mathbf{k}^v_{||}$ are the parallel wavevector components of the photoelectron inside the solid and in vacuum respectively. Its component perpendicular to the surface $k_\perp$ is not conserved during transmission through the surface. The kinetic energy of the photoelectron E_{kin} on the vacuum side, referenced with respect to the vacuum level E_{vac}, is given by energy conservation

$$E_{kin} = h\nu - |E_B| - |\phi|, \tag{2.4}$$

where ϕ is the workfunction of the sample surface.
The norm of the parallel component of the wavevector can now be determined directly from experimental parameters using Eq. 2.3 and 2.4.

$$k^s_{||} = k^v_{||} = k^v \sin\theta,\ k^v = \sqrt{\frac{2m}{\hbar^2}E_{kin}} = \sqrt{\frac{2m}{\hbar^2}(h\nu - |E_B| - |\phi|)}$$

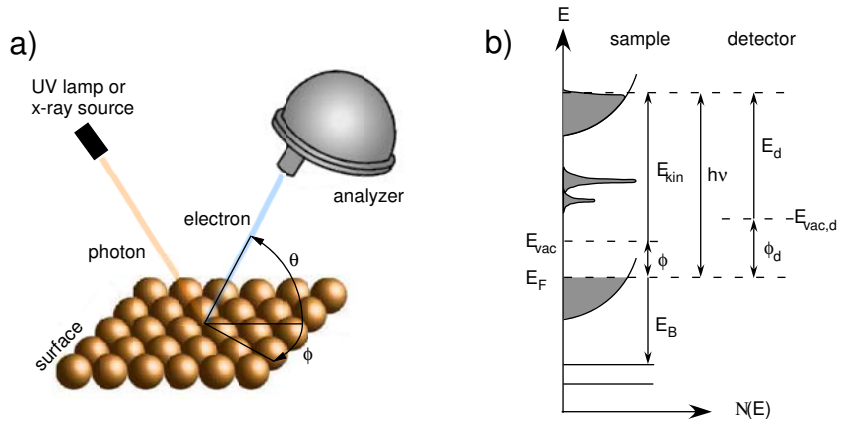

Figure 2.15: a) Sketch of the ARPES geometry. b) Energetics of the photoemission process.

where θ is the polar emission angle of the photoelectron and m the free electron mass. Together with the azimuthal emission angle ϕ, $\mathbf{k}^s_{||}$ is completely defined. On the other hand, due to the surface potential V_o, $k_\perp$ is not conserved. The vacuum component $k^v_\perp$ is determined by energy conservation

$$k^v_\perp = \sqrt{(k^v)^2 - (k^v_{||})^2} = \sqrt{\frac{2m}{\hbar^2}(h\nu - |E_B| - |\phi|)\cos^2\theta}.$$

Inside the solid, using the free electron final state approximation, we have

$$k^s = \sqrt{\frac{2m}{\hbar^2}(h\nu - |E_B| - |\phi| + |V_o|)}.$$

For $k^s_\perp$ we then obtain

$$k^s_\perp = \sqrt{(k^s)^2 - (k^s_{||})^2} = \sqrt{\frac{2m}{\hbar^2}(h\nu - |E_B| - |\phi|)\cos^2\theta + |V_o|}.$$

Thus the optical potential causes refraction of the photoelectrons in analogy with optical waves passing an interface.

During a measurement, the sample is in electrical contact with the detector causing their respective Fermi energies E_F to align (see Fig. 2.15b)). Since the workfunction of sample ϕ and detector ϕ_d are generally not the same, the vacuum level of sample and detector are not aligned. Consequently the energy of the photoelectron measured by the detector E_d is given by

$$E_d = E_{kin} + |\phi| - |\phi_d|.$$

In practice, ϕ_d is determined by measuring E_d of photoelectrons ejected from the Fermi energy of a polycrystalline metallic sample. The workfunction ϕ of the sample may be determined by taking the difference between the photon energy $h\nu$

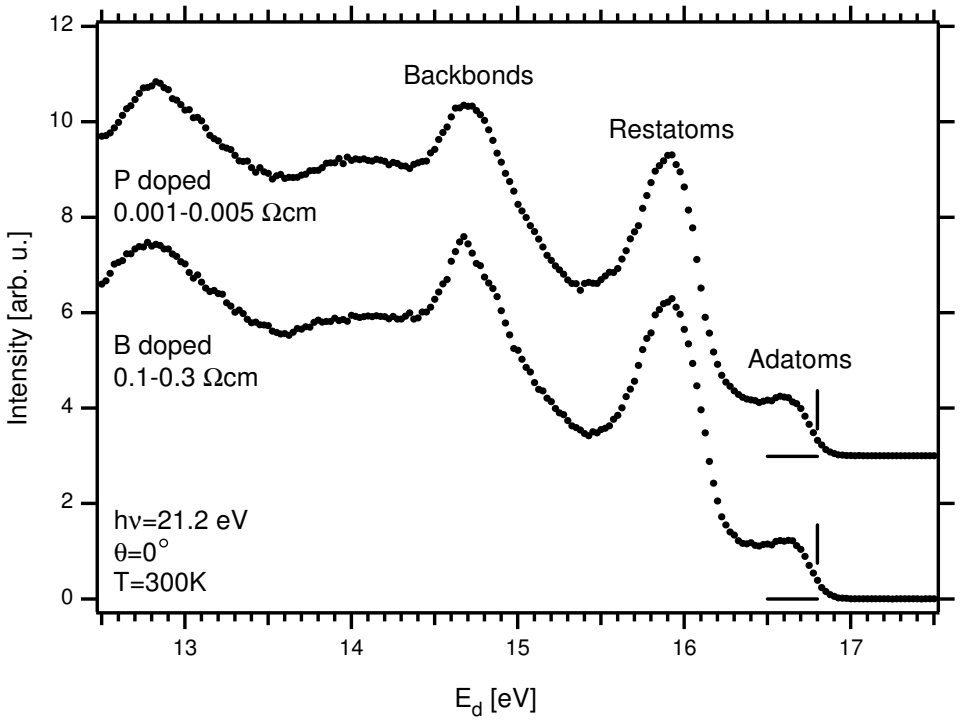

Figure 2.16: Photoemission energy distribution curve for a n- and p-type Si(111)-(7×7) surface. The short horizontal lines indicate the zero intensity level of the respective curve. The vertical line at $E_d = 16.8$ eV indicates the Fermi energy. The position of the Fermi energy has been determined using a polycrystalline Au sample.

and the experimentally determined energy interval between electrons originating from the Fermi energy $E_B = 0$ and electrons originating from states at energy $E_B = h\nu - \phi$. Since the kinetic energy of photoelectrons originating from a state at energy $E_B = h\nu - \phi$ is equal to zero, a negative bias of a few Volts needs to be applied to the sample for post acceleration. Note however, that for the determination of E_B only knowledge of ϕ_d is required.
In order to map out the dispersion along a chosen direction in reciprocal space, the photoelectron current I is measured as a function of binding energy E_B and emission angles (θ, ϕ). These so-called energy distribution curves (EDC) are then assembled in a two-dimensional plot $I(\mathbf{k}_{||}, E_B)$ by converting emission angles into parallel wavevectors. For Fermi surface maps on the other hand, the photoelectron intensity distribution is collected from a small, resolution limited energy window centered on E_F as a function of $\mathbf{k}_{||}$. Within the free electron final state approximation, these maps correspond to a spherical cut of radius k^s through the Fermi surface.

Figure 2.16 shows EDCs for a n- and p-type sample. The various states have been attributed to adatoms, restatoms and backbonds [56]. Note that the Fermi level of the Si(111)-(7×7) surface is pinned rendering the position of the spectral features independent of the bulk doping.

2.7 Electronic structure calculations

Theory and experiment have continuously stimulated each other. Electronic structure theory has achieved a considerable level of reliability in predicting the structure and properties of materials. Modern implementations do not only determine the electronic band structure of a solid, but also perform geometry optimization and molecular dynamics simulation by relaxing the atomic coordinates according to the forces. The generation of dynamical matrices gives access to the phonon band structure. Excited states may be computed within many-body perturbation theory. In what follows, we first discuss the elegant semi-empirical tight binding approach followed by an introduction to first-principles density functional theory.

2.7.1 Tight binding theory

Quantum mechanics allows in principle to write down the equations for any kind of system. In practise the solution of the Schrödinger equation becomes intractable already for systems containing only a moderate number of atoms. A series of approximations are required to solve the many-body problem. Since the motion of the nuclei is slow compared to the dynamics of the electrons, calculations can be carried out within the Born-Oppenheimer approximation, which assumes a static configuration of nuclei.
Within the tight binding theory originally proposed by Bloch [82], the electronic wave functions in a solid are approximated by linear combinations of atomic orbitals (LCAO) [83]. The position of an atom l in the unit cell j may be decomposed into $\mathbf{r}_{jl} = \mathbf{R}_j + \mathbf{r}_l$, where $\mathbf{R}_j$ is the location of the jth unit cell of the Bravais lattice and r_l the position of atom l within the unit cell. The isolated atom l is described by the atomic Hamiltonian $h_l(\mathbf{r} - \mathbf{r}_{jl})$. The atomic energy spectrum ϵ_{ml} and the eigenfunctions $|\phi_{ml}(\mathbf{r} - \mathbf{r}_{jl})\rangle$ may be determined by solving the corresponding Schrödinger equation

$$h_l(\mathbf{r} - \mathbf{r}_{jl})|\phi_{ml}(\mathbf{r} - \mathbf{r}_{jl})\rangle = \epsilon_{ml}|\phi_{ml}(\mathbf{r} - \mathbf{r}_{jl})\rangle.$$

Here m denotes a set of quantum numbers specifying the state $|\phi_{ml}(\mathbf{r} - \mathbf{r}_{jl})\rangle$. These atomic orbitals are known as Löwdin orbitals [84] and have been constructed in a way that wave functions centered at different atoms are orthogonal to each other without affecting their symmetry. Next we assume that the Hamiltonian H for the solid is equal to the sum of atomic Hamiltonians h_l and a term V which describes the interaction between different atoms. We further assume the interaction between atoms to be weak so that H can be diagonalized by perturbation theory. The eigenfunctions of the unperturbed Hamiltonian $H_0 = \sum_{jl} h_l(\mathbf{r} - \mathbf{r}_{jl})$ can be constructed as a linear combination of atomic orbitals $|\phi_{ml}(\mathbf{r} - \mathbf{r}_{jl})\rangle$. In order to account for the translational symmetry of the crystal, the unperturbed wave functions are expressed in the form of Bloch functions

$$|\Phi_{ml\mathbf{k}}(\mathbf{r})\rangle = \frac{1}{\sqrt{N}} \sum_j e^{i\mathbf{r}_{jl}\cdot\mathbf{k}} |\phi_{ml}(\mathbf{r} - \mathbf{r}_{jl})\rangle \tag{2.5}$$

where N is the number of unit cells in the crystal. The eigenfunctions $\Psi_{\mathbf{k}}$ of the full crystal Hamiltonian $H = H_0 + V$ indexed by the crystal momentum $\mathbf{k}$ may be written as a linear combination of $|\Phi_{ml\mathbf{k}}\rangle$

$$|\Psi_{\mathbf{k}}(\mathbf{r})\rangle = \sum_{ml} C_{ml} |\Phi_{ml\mathbf{k}}(\mathbf{r})\rangle.$$

To calculate the eigenfunctions $|\Psi_{\mathbf{k}}\rangle$ and eigenvalues E_k of H we operate with H on $|\Psi_{\mathbf{k}}\rangle$

$$H|\Psi_{\mathbf{k}}\rangle = E_k|\Psi_{\mathbf{k}}\rangle.$$

Using the orthogonality of the Bloch functions, which results from the orthogonality of the atomic orbitals, we obtain a set of linear equations for the C_{ml}

$$\sum_{m'l'} \Big(\langle \Phi_{m'l'\mathbf{k}}|H|\Phi_{ml\mathbf{k}}\rangle - E_k \delta_{mm'}\delta_{ll'} \Big) C_{ml} = 0.$$

Substituting equation 2.5 into the matrix element, we get

$$\begin{aligned}
\langle \Phi_{m'l'\mathbf{k}}|H|\Phi_{ml\mathbf{k}}\rangle &= \frac{1}{N}\sum_j \sum_{j'} e^{i(\mathbf{r}_{jl}-\mathbf{r}_{j'l'})\cdot\mathbf{k}} \langle \phi_{m'l'}(\mathbf{r}-\mathbf{r}_{j'l'})|H|\phi_{ml}(\mathbf{r}-\mathbf{r}_{jl})\rangle \\
&= \frac{1}{N}\sum_j \sum_{j'} e^{i(\mathbf{R}_j-\mathbf{R}_{j'}+\mathbf{r}_l-\mathbf{r}_{l'})\cdot\mathbf{k}} \langle \phi_{m'l'}(\mathbf{r}-\mathbf{r}_{j'l'})|H|\phi_{ml}(\mathbf{r}-\mathbf{r}_{jl})\rangle \\
&= \sum_j e^{i(\mathbf{R}_j-\mathbf{R}_{j'}+\mathbf{r}_l-\mathbf{r}_{l'})\cdot\mathbf{k}} \langle \phi_{m'l'}(\mathbf{r}-\mathbf{r}_{j'l'})|H|\phi_{ml}(\mathbf{r}-\mathbf{r}_{jl})\rangle
\end{aligned}$$

One of the summations in the double sum has been eliminated since it merely amounts to multiplying the single summation by N [83]. Since the atomic orbitals $|\phi_{ml}(\mathbf{r}-\mathbf{r}_{jl})\rangle$ are localized on atom l the summation is often restricted to nearest neighbor (n.n.) cells only

$$\langle \Phi_{m'l'\mathbf{k}}|H|\Phi_{ml\mathbf{k}}\rangle = \sum_j^{n.n.} e^{i(\mathbf{R}_j+\mathbf{r}_l-\mathbf{r}_{l'})\cdot\mathbf{k}} \langle \phi_{m'l'}(\mathbf{r}-\mathbf{r}_{j'l'})|H|\phi_{ml}(\mathbf{r}-\mathbf{r}_{jl})\rangle.$$

Here $\mathbf{R}_{j'}$ has been chosen to be at the origin.
All we have to do now in order to obtain the band structure is to diagonalize the Hamiltonian matrix $\langle \Phi_{m'l'\mathbf{k}}|H|\Phi_{ml\mathbf{k}}\rangle$ for the $\mathbf{k}$ points of interest. The size of the Hamiltonian is given by the number of atoms in the unit cell and the number of orbitals which are taken into account. Note that the number of orbitals must not be the same for inequivalent atoms in the unit cell.
For the diagonal intra-atomic matrix elements the atomic energies ϵ_{ml} tabulated in Harrison's book Ref. [85] may be used

$$\langle \phi_{ml}(\mathbf{r}-\mathbf{r}_{jl})|H|\phi_{ml}(\mathbf{r}-\mathbf{r}_{jl})\rangle \approx \epsilon_{ml}.$$

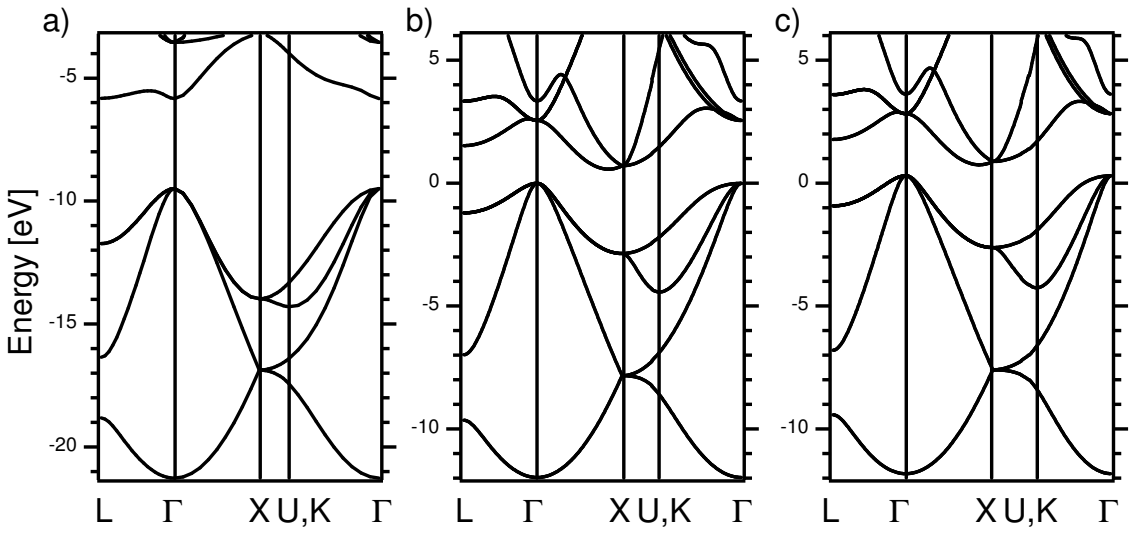

Figure 2.17: Band structure of Si along high-symmetry directions calculated using different methods: a) tight binding approach, b) full-potential augmented plane wave + local orbitals method [88], c) pseudo-potential plane wave method [89].

Off-diagonal intra-atomic matrix elements are zero

$$\langle \phi_{m'l}(\mathbf{r} - \mathbf{r}_{jl})|H|\phi_{ml}(\mathbf{r} - \mathbf{r}_{jl})\rangle \approx 0.$$

The off-diagonal inter-atomic matrix elements may be obtained from the solid state table in Ref. [85] in combination with the formulas given by Slater and Koster [83,86]. Fig. 2.17a) presents the band structure of Si calculated within our own tight binding code including Si 2s and 2p orbitals. The energies of the atomic levels $\epsilon_{Si,2s} = -13.55$ eV and $\epsilon_{Si,2p} = -6.52$ were taken from Herman and Skillman [87]. Off-diagonal matrix elements were determined by taking the values from the solid state table of Ref. [85] using $(ss\sigma) = -1.93$ eV, $(sp\sigma) = 2.54$ eV, $(pp\sigma) = 4.47$ eV, $(pp\pi) = 1.76$ eV.
As can be seen from Fig. 2.17 the occupied part of the band structure obtained within the tight binding approach agrees quite well with the results from more complex electronic structure methods. A better agreement may be achieved by fitting the tight binding band structure directly onto first-principles results. More flexibility in fitting may be achieved by including next nearest neighbors off-diagonal inter-atomic matrix elements. Although highly simplified, properly designed and parameterized semi-empirical calculations can be both efficient and quite reliable.

2.7.2 Density functional theory

In 1964 Hohenberg and Kohn [90] proved that the ground state energy of a system of interacting electrons even in the presence of a static external potential is a unique functional of the ground state density. In particular the exchange and correlation

energy is also a functional of the density. Kohn and Sham [91] subsequently showed that it is possible to replace the many-electron problem by an exactly equivalent set of self-consistent one-electron equations. The shift from the many-body wave function depending on $3N$ variables to the single-particle density implies an enormous advantage, because the density, no matter how large the system is, has only three variables x, y and z.
So far no approximation has been employed since the difficulty of solving the many-body problem was only transferred to the unknown exchange-correlation functional. Within the local density approximation (LDA) one takes the exchange-correlation energy of an electron in a homogeneous electron gas of a density equal to the density in the system being calculated, which is in general inhomogeneous. LDA is local in the sense that the electron exchange and correlation energy at any point in space is a function of the electron density at that point only.
In practice, numerical solutions of the Kohn-Sham equations are obtained by expanding the Kohn-Sham orbitals in a suitable finite set of basis functions. Within the augmented plane wave method, the unit cell is divided into non-overlapping muffin tin spheres centered on the atoms and an interstitial region. In the interstitial region the basis functions are plane waves. Inside the muffin tin, is is more suitable to use a linear combination of spherical harmonics. In order to obtain a well-behaved solution to the Kohn-Sham eigenvalue problem, the plane waves outside the muffin tins must be matched to the functions inside. A basis set combining plane waves with localized orbitals is well suited for a description of the rapid oscillations of the Bloch functions close to the nuclei and is thus often used in all electron implementations. Due to the large oscillations of the core orbitals in the neighborhood of a nucleus, plane waves alone cannot be used directly in the Kohn-Sham formalism. These oscillations would require an enormous basis set size to achieve an acceptable description. Within the pseudo-potential method, the effect of the core electrons is included in an effective potential and only the valence electrons are contained in the associated pseudo-wavefunction. This allows to use a relatively small plane wave basis, which renders the pseudo-potential methods computationally efficient. As can be seen from comparison of Fig. 2.17b) and c), the two methods deliver almost identical results.
By construction DFT is a method to obtain the electron density and the total energy of a many-body system in its ground state. However, since the effective DFT potential resembles the potential seen by electrons the Kohn-Sham eigenvalues are often interpreted as quasiparticle energies without formal justification. This works usually quite well for occupied states, but is generally less reliable for empty states. A common problem is that LDA band gaps often come out much smaller than in experiment. The experimental band gap of Si of 1.17 eV measured at low temperature [44] should be compared to the calculated band gap of 0.58 eV computed within the augmented plane wave method. The most popular method to compute quasiparticle energies is the GW method of Hedin [92], which delivers band gaps with typical discrepancies of only 0.2 eV with respect to experimental data [93]. How-

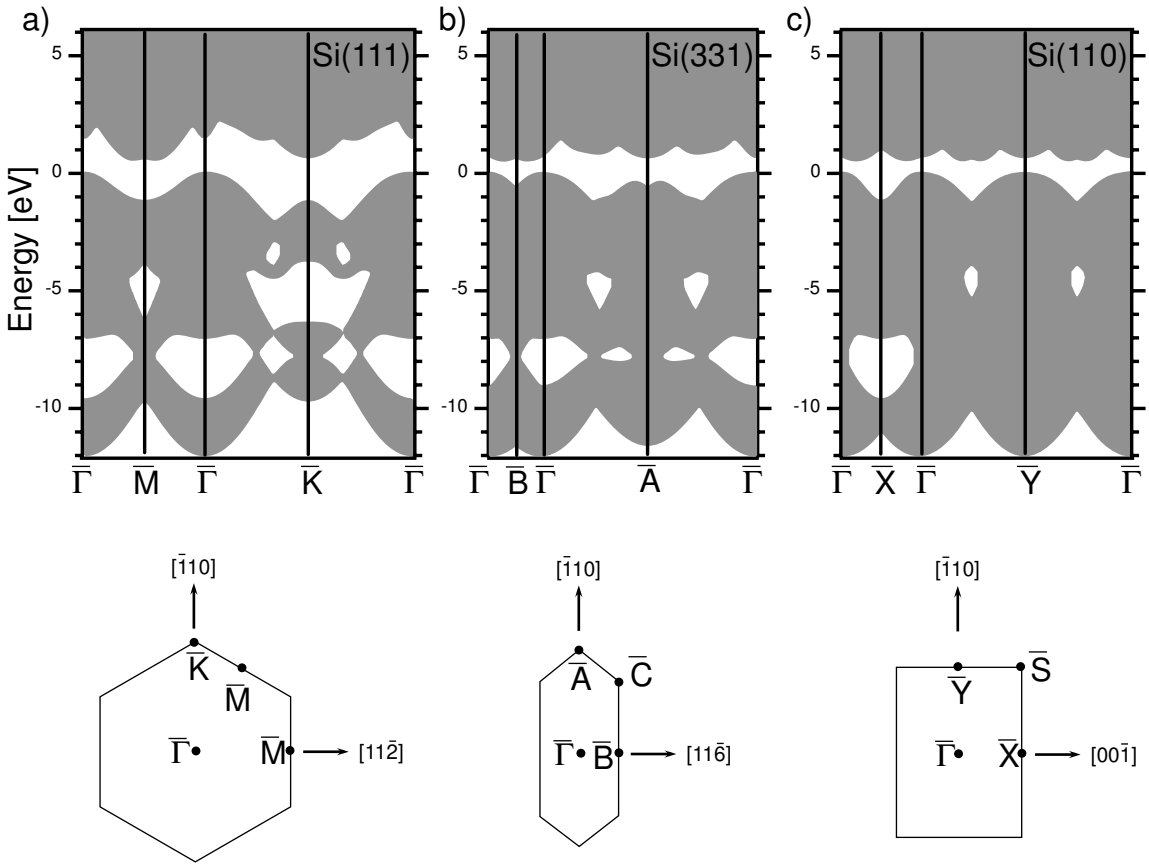

Figure 2.18: Projected bulk band structure for the a) Si(111), b) Si(331) and c) Si(110) surface along high-symmetry directions calculated using the full-potential augmented plane wave + local orbitals method [88]. The corresponding surface Brillouin zones including high symmetry points and bulk directions are shown as well.

ever, rigorous quasiparticle calculations are time consuming, because the dielectric response of the system has to be calculated.

For a given structure, forces on atoms and stresses on the cell may be computed. Such information allows to optimize the atomic positions and unit cell parameters by comparison of various trial structures. The typical accuracy on such geometry parameters is of the order of a few percents [93]. The relaxed cubic unit cell parameter for Si computed within the pseudo-potential method is $a = 5.40$ Å and compares nicely with the experimental value of $a = 5.43$ Å [94].

Within density functional perturbation theory (DFPT), linear and non-linear responses to applied electric fields, applied strains and internal atomic displacements may be computed allowing to access properties such as the optical dielectric tensor, the static dielectric tensor, the elastic tensor, the piezoelectric tensor, the Born effective charges, the interatomic force constants and the dynamical matrices, from

which the full phonon band structure can be computed.
In order to study surface properties, one usually works with a slab geometry. A slab simulates a semi-infinite crystal by taking into account only a small number of crystal layers separated by a vacuum region. Periodicity normal to the surface is restored by considering periodic arrays of supercells. The number of layers must be chosen sufficiently large to avoid that opposite surfaces interact. The number of vacuum layers is chosen such as to minimize the overlap of evanescent waves from surfaces of neighboring slabs. Typical numbers are ten semiconductor layers to simulate the bulk and five equivalent vacuum layers per supercell.
A surface reconstruction almost always leads to the formation of a superstructure. The calculations then have to be carried out within a larger unit cell. Within density functional theory, this leads inevitably to a higher number of bands and backfolding of bands. However, in real experiments, it is only the surface periodicity which gets larger, whereas the bulk periodicity remains unchanged. Thus the bulk bands are not expected to backfold. In order to compare theory with experiment it is thus useful to determine the surface-projected bulk band structure of Si. The projected band structure of a surface is obtained by projecting the band structure across the entire bulk Brillouin zone onto the surface Brillouin zone. Fig. 2.18 shows the bulk projected band structure for the Si(111), Si(331) and Si(110) surfaces along with the corresponding surface Brillouin zones. Projected band structures are also useful for determining regions within the bandstructure where surface states or surface resonances may exist.
One of the key criterions which determine the practical value of an *ab initio* result is its numerical convergency and an estimate of the error bar. Although a first-principles calculation is free from empirical parameters, it does employ parameters which control numerical performance. Resources such as computing time, memory and disk space are limited and their usage must be traded against accuracy. Key parameters are the size of the basis function set and the number of $\mathbf{k}$ points sampling the Brillouin zone. For slab calculations, the convergence of surface properties with respect to the number of bulk layers and the vacuum thickness must further be verified. However, even a perfectly converged *ab initio* calculation contains a biased input: the atomic configuration before the energy optimization. Within a given symmetry some structural degrees of freedom may be available during relaxation, however alternative or lower symmetries must be considered. Even the number of surface atoms may differ between physically plausible structures. It is therefore imperative that as many structures as practicable are compared to as many experimental results as possible, before a particular model may be accepted.

2.8 Preparation of silicon surfaces

Surface preparation is crucial if one wants to study structural and electronic properties at the atomic scale. In what follows we describe our optimized surface prepa-

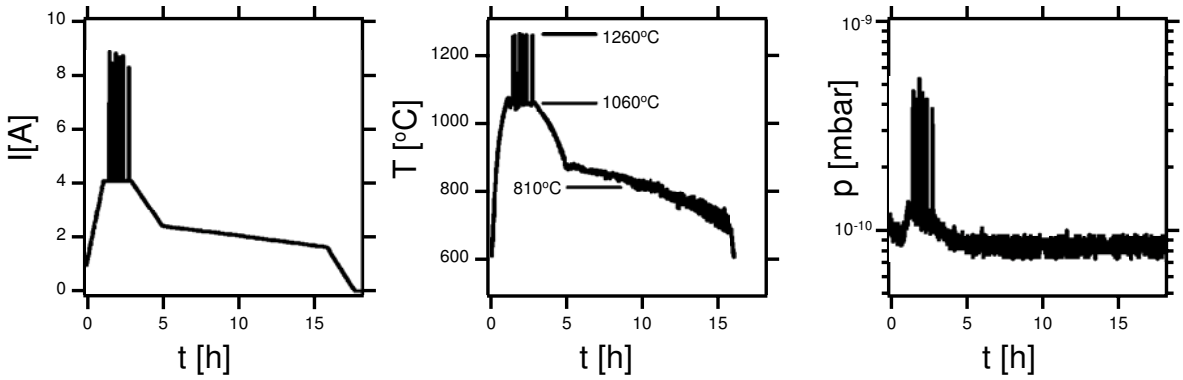

Figure 2.19: Typical preparation cycle for a Si(331) surface. a) current vs time, b) temperature vs time, c) pressure vs time.

ration process. Using a fully automated system, Si surfaces of very high quality are prepared routinely.

To avoid Ni contamination, any contact of silicon with stainless steel must be avoided. Si samples and the Mo sample holders are exclusively handled with teflon tweezers and Mo or Ta tools. All samples are first cleaned for 5 minutes in an acetone ultrasound bath followed by an ethanol ultrasound bath for another 5 minutes. Coming out of the ethanol bath, the samples are dry blown with clean nitrogen gas, mounted on the Mo holder and transferred into vacuum.

During the first preparation step in vacuum, the sample is degassed by passing a direct current through the sample. In our setup a pressure signal from the gauge controller is sent into a feedback loop which controls the sample current while keeping the pressure below 5×10^{-10} mbar. Once the sample temperature attains at 1060^o C, the sample is flashed repeatedly to 1260^o C. The ramp from 1060^o to 1260^o C is performed within 2 seconds, the cool-down back to 1060^o C is completed within 10 seconds during the first flashes in order to keep the pressure during the entire flash below 2×10^{-9} mbar. The cool-down period during the final flashes is 30 s. At 1060^o C single steps on Si(111) have been reported to be stable [95] and we find it to be an ideal base temperature to perform flashing to higher temperature, since it is above the transition temperature for all known Si surface reconstructions. The stress on the wafer, induced by the fixation to the sampleholder, should be minimized to allow the sample to expand freely upon heating.

The cool-down sequence which follows is crucial for the quality and long range order of the surface reconstruction. Ideally one would like to keep the sample for a certain period at the transition temperature to allow long range order to be established. However, transition temperatures reported in the literature are usually accurate to within only 20^o to 30^o C. Additional uncertainties arise due to the difficulty to obtain an absolute calibration for our own pyrometer which works at a single wave length. Uncertainties due to value of the selected emissivity should also not be forgotten. All our measurements on Si surfaces were carried out using an emissivity ϵ

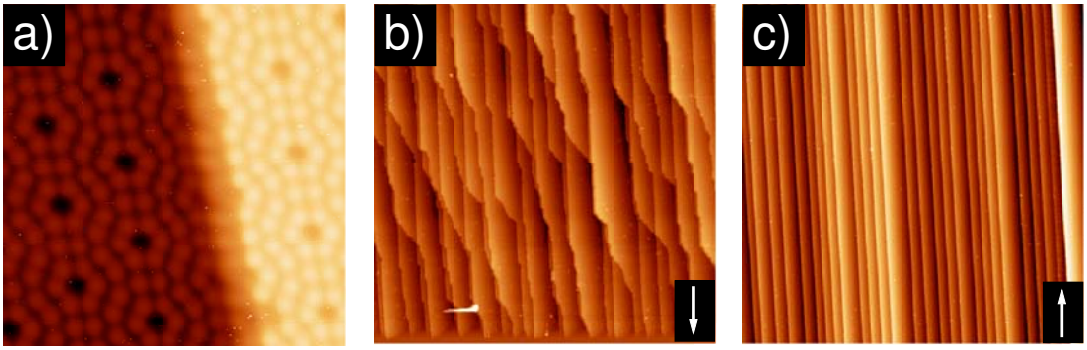

Figure 2.20: a) STM image of an atomically precise single bilayer step on Si(111)-(7×7) (11 nm × 11 nm). Stepped Si(111) surface prepared with the direct current passing in the b) kink-down and c) kink-up direction (500 nm × 500 nm). U=1.8 V, I=0.5 nA. The heating current direction is indicated by the arrows.

of $\epsilon = 0.65$, neglecting the effect of the optical view port.
Our cool-down strategy is simple, but yet highly effective. Instead of annealing the sample at a fixed temperature, we start the annealing sequence at about 50^o C above the transition temperature and slowly cool the sample down to a temperature of about 50^o C below the transition temperature typically within 12 h. The slow cool-down rate guarantees that the sample spends enough time close to the transition temperature to optimize its long range order. Sample preparation is completed by a cool-down of 2 h down to room temperature. With this method we are able to obtain almost defect free, atomically precise surface reconstructions over areas approaching micrometer dimensions.
Fig. 2.19 shows the preparation cycle for a Si(331) surface. For process control purposes it is useful to record not only the current a) and the temperature b) of the sample as a function of time but also the pressure c) during the entire preparation cycle. The three automated steps of the preparation cycle, degassing, flashing and cool-down including annealing, can be clearly distinguished in all three traces. Note that the Si(331)-(12×1) reconstruction forms at a temperature of 810^o C, which lies approximately in the middle of the annealing temperature range.

Si(111) surfaces exhibits a three-fold rotational symmetry. Consequently atomic chains on Si(111), which are the topic of chapter 4, grow in domains with three degenerate orientational variants separated by 120^o with respect to each other. If the domains are relatively large, this does not cause a problem to STM. In contrast, since LEED and ARPES integrate information over macroscopic areas of the surface, the resulting data represents the incoherent addition from all three domains. The three-fold symmetry of the substrate may be broken by using stepped surfaces. In order to stabilize single domain atomic chains, it is important to control the step morphology of the surface. Viernow *et al.* [95] have reported a method to produce regular arrays of atomically straight single bilayer steps on vicinal Si(111) surfaces using slightly vicinal surfaces with an intentional miscut of 1.1^o towards the $[\bar{1}\bar{1}2]$

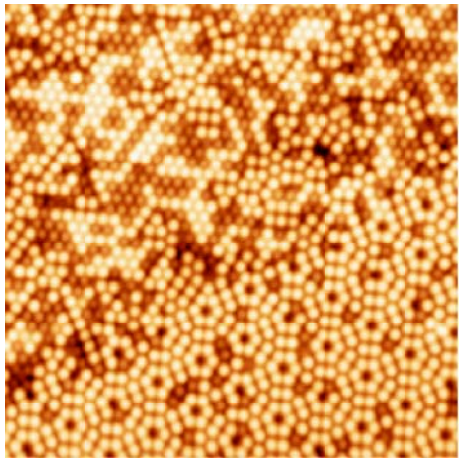

Figure 2.21: STM image of a highly boron doped Si(111) surface exhibiting the Si(111)-(7×7) and the Si(111)-($\sqrt{3} \times \sqrt{3}$)-R30^o reconstruction. $T = 5$ K, $U = 1.9$ V, $I = 0.5$ nA, 25nm×25nm.

direction (see Fig. 2.20a)). Si(111) surfaces with a miscut towards [11$\bar{2}$] have a strong tendency to spontaneous step bunching [96] and do therefore not qualify as candidates. The preparation cycle is similar to the sequence described before. The direct current is passed through the sample parallel to the direction of the steps to avoid step bunching due to electromigration. The most critical part is a quench from 1060^o C to 830^o C to avoid a step tripling regime just below the (1×1) to (7×7) transition temperature at 870^o C. Thermal disorder induced by the quench is removed by postannealing at 830^o C, where the mobility of single steps is too low for the formation of triple steps. If this temperature is too high, some single steps coalesce into triple steps. If the temperature is too low, thermal disorder is not healed out completely.

Fig. 2.20b) presents a STM image of a stepped Si(111) surface. One observes atomically straight single bilayer steps interrupted by a series of kinks. The width of each terrace and each kink is quantified in units of the Si(111)-(7×7) unit cell. The kinks are created by a small miscut in the azimuthal direction away from the [$\bar{1}\bar{1}$2] direction. They are highly undesirable since they serve as nucleation centers for atomic chains with an alternative direction. Yoshida *et al.* [97] have demonstrated that annealing of stepped Si(111) surfaces at 830^o C with the current passing in the kink-up direction enhances the formation of straight step edges over micrometer length (see Fig. 2.20c)), while annealing with a current in the kink-down direction does not. The effect has been explained using a phenomenological model based on electromigration. Since the global miscut of the surface is conserved, kinks accumulate into large kink bunches. This is a relatively cheap price to pay, since these kink bunches only induce small domains of atomic chains with secondary orientation.
There are two possibilities to induce self-assembly of atomic chains on the Si(111)-(7×7) surface. The first method consists in deposition of the adsorbate at room

temperature followed by postannealing slightly below the desorption temperature. In the second method, the adsorbate is deposited on the hot substrate. We find that the second method significantly improves the quality of the single domain atomic chain reconstruction. The reason for this is that during the conversion of the Si(111)-(7×7) reconstruction into the atomic chain reconstruction, some of the Si surface atoms of the Si(111)-(7×7) structure are not required anymore. These Si atoms coalesce into islands, which significantly disorder the regular step array and provoke atomic chains with orientations differing from the main orientation. We also find that atomic chains grow in a chain reaction process. A critical adsorbate density is required to corrode the Si(111)-(7×7) reconstruction locally and to initiate the self-assembly of atomic chains [98] which then proceeds away from the nucleation center by transforming neighboring (7×7) cells into chains. Evidence for this phenomenon comes from the fact that below the ideal adsorbate coverage, we usually observe terraces which are completely covered by atomic chains separated by terraces exhibiting the Si(111)-(7×7) reconstruction.
STM, LEED and ARPES require conductive samples. Especially STM measurements at $T = 5$ K require highly doped semiconductors. Fig. 2.21 shows an STM image of a highly boron doped Si(111) surface (bulk resistivity $\rho = 0.022$ Ωcm at room temperature). Whereas the lower part of the image is still covered by the Si(111)-(7×7) reconstruction, the upper part is converted into the boron induced $(\sqrt{3} \times \sqrt{3}) - R30^o$ reconstruction. During prolonged annealing boron atoms segregate from the bulk and accumulate at the surface. The influence of boron atoms can also be seen on the Si(111)-(7×7) reconstruction, where several adatoms exhibit a markedly lower local density of states. Minor modifications of the surface properties are observed on samples doped with phosphorus impurities (bulk resistivity up to $\rho = 0.001$ Ωcm at room temperature), leaving the Si(111)-(7×7) reconstruction intact. Although phosphorus atoms potentially segregate from the bulk to the surface, they do not accumulate at the surface, but are believed to combine with hydrogen atoms present in the residual gas of the vacuum chamber and to desorb in the gaseous phosphine PH_3 form.

2.9 Experimental setup

Experiments were carried out in a UHV chamber with a residual gas pressure below 3×10^{-11} mbar equipped with a low-temperature STM (Omicron LT-STM ♯057) allowing measurements at temperatures down to 4.5 K (see Fig. 2.22a) and b)). A counter-heating facility (Lakeshore 331) allows to access a wide range of temperatures. Spectroscopy measurements are performed using a lock-in amplifier (Perkin Elmer Signal Recovery DSP lock-in amplifier 7260 and 7265). Before entering the STM electronics (Omicron Scala), the reference modulation signal produced by the lock-in amplifier is going through a passive attenuator box (Texscan BMA-580) in order to enhance the signal-to-noise ratio for small modulation amplitudes. Al-

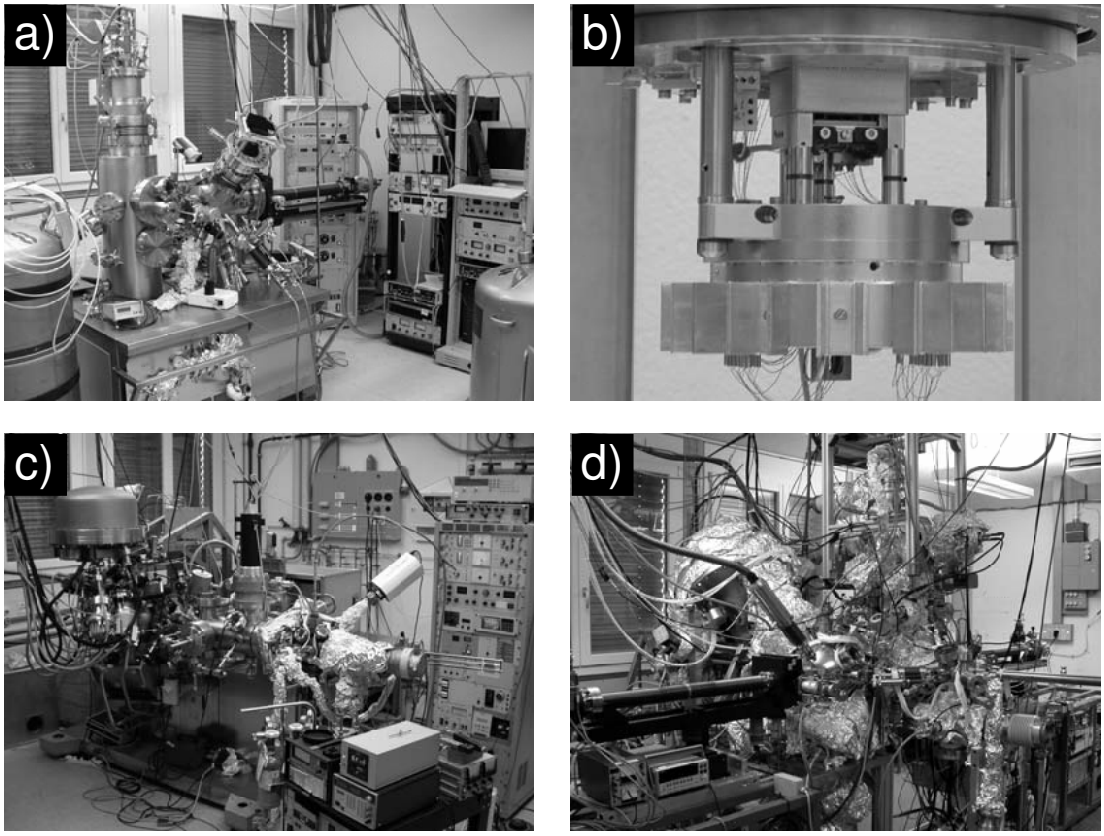

Figure 2.22: a) Picture of the LT-STM lab. b) Close-up view of the LT-STM stage. c) Picture of the ESCA ARPES lab. d) Picture of the Scienta ARPES lab.

though crosstalk is already compensated by the hybrid circuit in the preamp of the STM, residual crosstalk may be suppressed by a homemade passive compensation circuit. A separate chamber connected to the STM chamber via a UHV valve allows preparation of samples on a homemade direct current heating stage, on a homemade e-beam heater or on a resistive heater mounted on the sample manipulator. Sample temperature may be measured by an ex-situ pyrometer (Inficon Ultimax) across an optical view port or in situ using the thermocouple on the sample manipulator. The manipulator with homemade motorized z-translation allows to transfer the sample from the preparation chamber into the analysis chamber for STM measurements. It can be cooled with either liquid N_2 or liquid He. It further allows manual polar rotation of the sample. A sputter gun facility (Omicron ISE 5) and an associated gas line system allow cleaning of the sample by ion bombardment and gas dosing. Two water-cooled e-beam evaporators (Omicron EFM 3 and homemade source) mounted via separate load-locks allow submonolayer deposition of a wide variety of evaporants in the 10^{-10} mbar range. Flux rates may be calibrated using a quartz deposition monitor (Inficon XTM2). A retractable Auger/LEED spectrometer (Omicron Spectaleed) operates in either standard LEED, IV-LEED or Auger spectroscopy mode.

LEED images are photographed via a calibrated 12-bit CCD camera (Photometrics SenSys) with single-stage Peltier cooler. For the IV-LEED and Auger spectroscopy capabilities a home-made control software is used. Most equipment is interfaced (LabView, Igor Pro) allowing complete control and reproducibility in the sample preparation process. A quadrupole spectrometer monitors vacuum quality. Samples are introduced into the preparation chamber via a separately pumped load-lock chamber which contains a homemade tip-heating facility (Didiot).
Full hemispherical ARPES experiments were performed in a separate UHV chamber based on a modified Vacuum Generator ESCALAB Mark II spectrometer with a residual gas pressure below 3×10^{-11} mbar equipped with a Mg K_α ($h\nu = 1253.6$ eV) x-ray anode, a monochromatized He discharge lamp providing He Iα ($h\nu = 21.2$ eV) radiation, and a three channeltron hemispherical electrostatic analyzer kept fixed in space during measurements (see Fig. 2.22c)). The sample is mounted on a homemade manipulator with two motorized and computer controlled rotational axes and may be cooled via a closed cycle refrigerator. High resolution ARPES measurements are performed on a second ARPES setup using a Scienta SES 200 analyzer (see Fig. 2.22d)).
Stepped silicon surfaces having an intentional misscut of 1.1^o towards $[\overline{11}2]$ were provided by the Institute of Electronic Materials Technology. All other silicon wafers were bought from Crystec. Teflon tweezers were used exclusively for handling silicon samples in order to avoid Ni contamination. Sample holders and the homemade sample mounting tool are made of Mo. Crystal alignment was checked using a single crystal x-ray diffractometer (Philips). Four-point probe resistivity measurements were carried out at the Centre Suisse d'Electronique et Microtechnique (CSEM).

Chapter 3

Silicon surface reconstructions

The determination of the structure of the Si(111)-(7×7) reconstruction has been a formidable challenge and a cornerstone of surface science due to its high complexity. A second well studied surface reconstruction is the (2×1) reconstruction of the technologically important Si(100) surface. A few other surface orientations are known to stabilize planar surface reconstructions. In section 3.1 we first discuss the reasons which cause semiconductor surfaces to reconstruct. In sections 3.2, 3.3 and 3.4, we review the structural models of important reconstructions and identify structural building blocks. In section 3.5 we present our experimental results on the Si(331)-(12×1) reconstruction, which lead us to propose a new structural model. A roadmap for future investigations on Si(331)-(12×1) given in section 3.6 concludes this chapter.

3.1 Why do semiconductor surfaces reconstruct?

Silicon crystallizes in the diamond structure with space group Fd-3m (227). The cubic lattice constant is a=5.4310Å [94]. In the bulk of the diamond structure, each of the tetrahedrally coordinated atoms forms four covalent bonds with its four nearest neighbors. Each bond contains two paired electrons. When a surface is formed, some of these bonds will be broken, leading to unsaturated orbitals, the so-called dangling bonds, containing only one unpaired electron. The lack of electron pairing makes dangling bonds unstable. The atoms in the surface region will move away from their bulk positions trying to minimize the surface energy. When this happens, the surface is said to relax or reconstruct depending on how the surface atoms seek new coordinates. Surface relaxation refers to the case when surface atoms are displaced from their bulk positions, but there is no change in the surface periodicity. Surface reconstruction on the other hand refers to atomic displacements causing the symmetry parallel to the surface to be lower than that of the bulk. At metal surfaces, the electrons are free to rearrange their distribution in space. Relaxation by adjustment of the interlayer spacing of the first few atomic planes is often sufficient to minimize the surface energy. At semiconductor surfaces, the

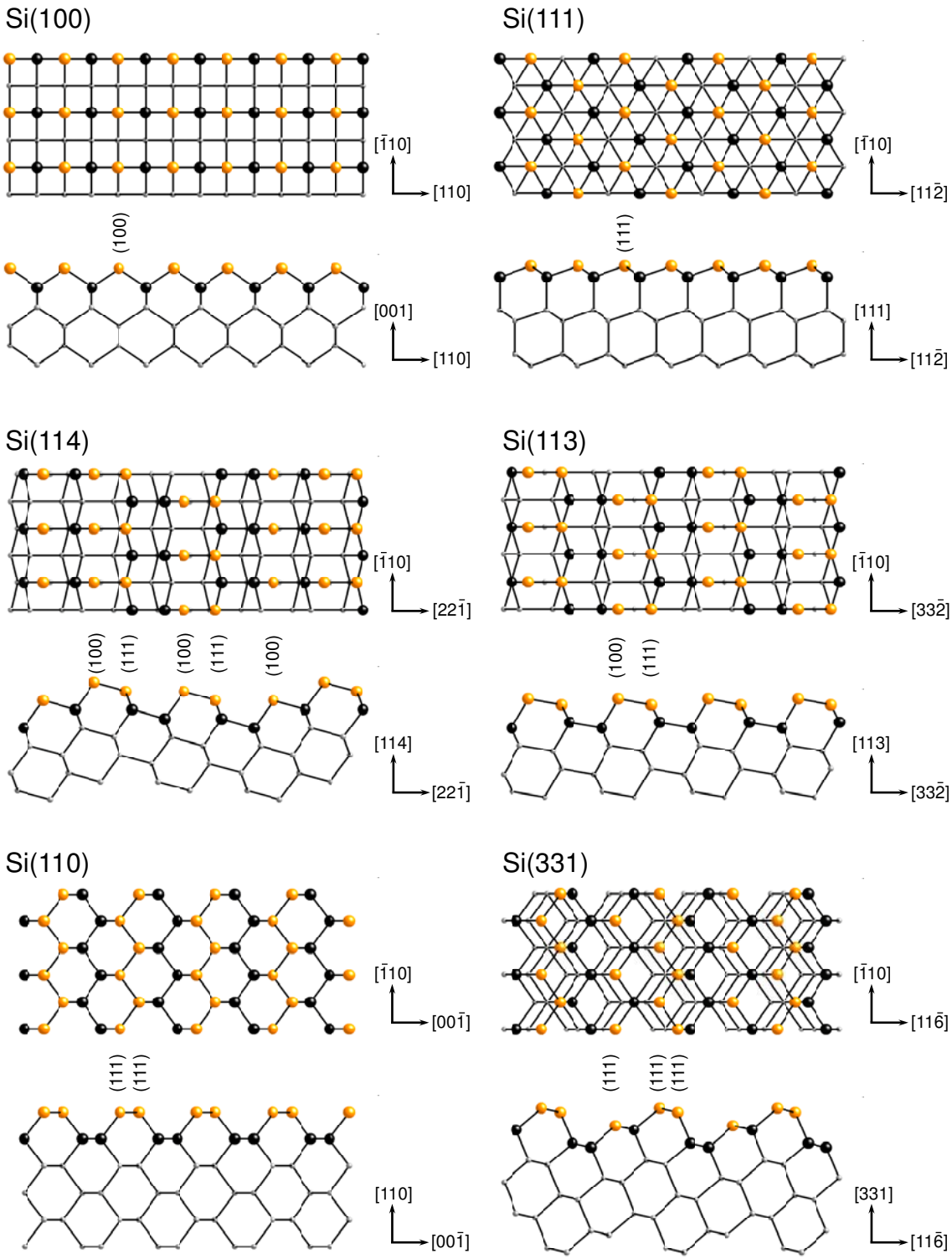

Figure 3.1: Dangling bond configuration of bulk-truncated silicon surfaces. Yellow atoms are surface atoms with unsaturated orbitals. Note that there are two types of surface atoms: (100)-type atoms with two dangling bonds and two backbonds and (111)-type atoms with one dangling bond and three backbonds. Black atoms are sub-surface atoms in the first bulk layer.

Surface	Surface atoms per unit cell	Dangling bonds per unit cell N	Unit cell area A [Å^2]	Dangling bond density n [Å^{-2}]
Si(100)	1	2	$a^2/2 = 14.75$	0.136
Si(114)	4	7	$3a^2/\sqrt{2} = 65.57$	0.112
Si(113)	2	3	$\sqrt{11}a^2/4 = 24.46$	0.123
Si(5512)	7	10	$3\sqrt{3}a^2/(2\cos 24.23^o)$ =84.03	0.119
Si(111)	1	1	$\sqrt{3}a^2/4 = 12.77$	0.078
Si(331)	3	3	$\sqrt{19}a^2/4 = 32.14$	0.093
Si(110)	2	2	$a^2/\sqrt{2} = 20.86$	0.096

Table 3.1: Dangling bond densities of bulk-truncated silicon surfaces.

truly directional chemical bonds between atoms lead to considerable elastic strain which increases the total energy of the surface. Stable surface reconstructions are obtained when the strain energy is compensated by the energy gain which results from the reduction of dangling bonds. Since stress and broken bonds cost energy, the most stable structure is not necessarily the one which minimizes the number of dangling bonds. Other factors such as the electronic structure must be considered as well, when trying to find the lowest energy configuration. A reconstruction, which produces a metallic surface, with fractional occupation of electronic states, is likely to be unstable. The instability may be removed by the opening of an energy gap via a Jahn-Teller type distortion or the formation of a charge density wave. When the number of surface atoms in the reconstruction differs from the one of the ideal bulk-truncated surface, the reconstruction may be kinetically limited by the transport of material from or to surface steps, which act as reservoir. At high temperatures, surface diffusion may play an important role. Due to the interplay of various factors, semiconductor surface reconstruction commonly yields structures that are much more complex than the ideal bulk-like surface termination.

The energy needed to break a silicon bond can be estimated from the cohesive energy, which is $E_c = 4.6$ eV per atom [99]. The cohesive energy of a solid is the energy per atom required to break the atoms of the solid into isolated atomic species. Since a bond is formed by two atoms and each silicon atom makes four bonds, the energy required to break a bond is half the cohesive energy, i.e. $E_b = 2.3$ eV per bond [85]. The surface formation energy E_s can now be estimated by multiplying the bond energy E_b by the density of broken bonds n. The latter is the number of broken bonds N per total surface area A, $n = N/A$. Thus $E_s = NE_b/2A$. The factor of 2 takes into account that two surfaces are created.

Table 3.1 summarizes the dangling bond densities n of some bulk-truncated silicon surfaces. Ball and stick models of the bulk-truncated surfaces are shown in Fig. 3.1. Since Si(111) exhibits the lowest dangling bond density, it is the preferred cleavage plane of silicon. It is interesting to note that on bulk-truncated silicon surfaces two types of atoms with unsaturated dangling bonds may occur. On Si(111) for instance,

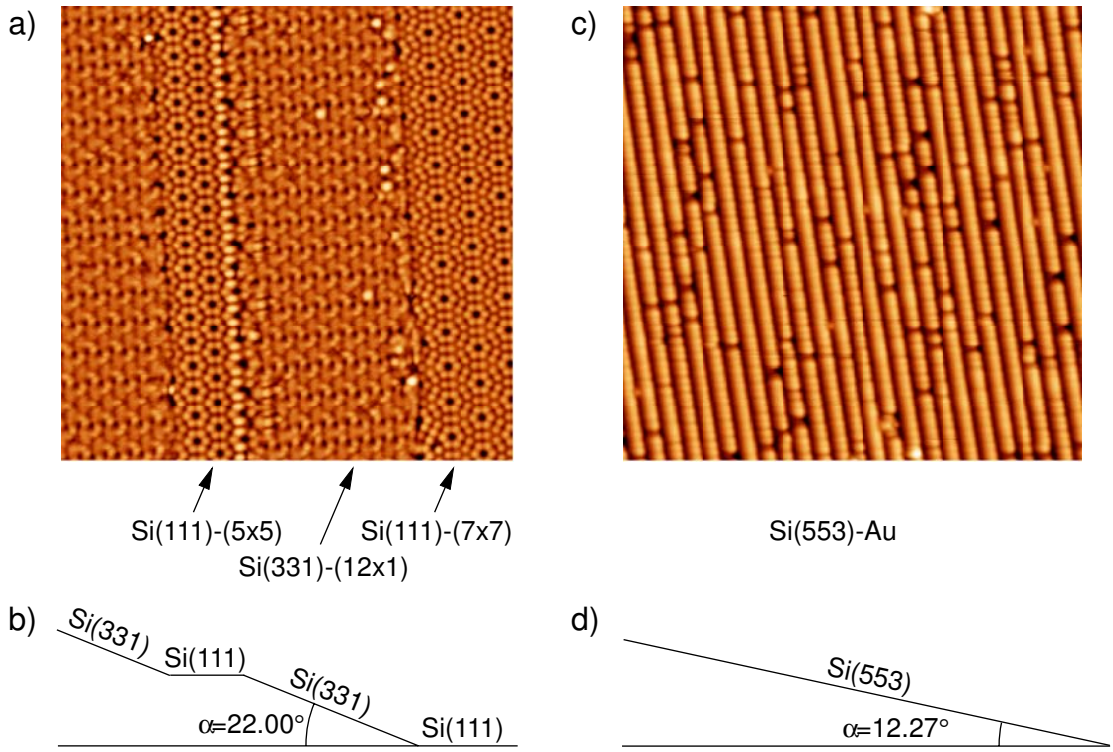

Figure 3.2: a) High-pass filtered STM image of the Si(553) surface exhibiting facets with (111) and (331) orientation. Note the coexistence of (111) facets covered with the Si(111)-(7×7) and the Si(111)-(5×5) reconstruction. b) Sketch of the profile of image a). c) STM image of the Si(553) surface stabilized by Au deposition. d) Sketch of the profile of image c). Both STM images measure 35 nm × 35 nm.

each surface atom remains bonded to three sub-surface atoms and thus exhibits one dangling bond. On Si(100) on the other hand, each surface atom exhibits two dangling bonds and is therefore bonded only to two sub-surface atoms. On Si(113) and Si(114) both types of surface atoms occur side by side.
Table 3.1 lists all known silicon surfaces with a stable planar surface reconstruction between (100) and (110). The structural models for the reconstructions observed on Si(100), Si(114), Si(113) and Si(111) may be considered as generally accepted and are discussed in the following sections. Structural models were also proposed for the Si(5512), Si(110) and Si(331) surface. However even their basic structural backbones are still strongly debated. Only little is known about surfaces with orientations away from this plane.

What happens when the surface is not oriented exactly along one of the directions allowing a planar reconstruction? For small deviations from some stable orientation, the surface consists of planar terraces oriented along the stable orientation separated by steps. The steps are responsible for compensating the small deviation. When

the deviation is increased, the step density increases and steps coalesce into step bunches. Increasing further the deviation, the crystal facets into planar terraces of alternating orientation in a way such that the macroscopic orientation is preserved. An example is given by the Si(553) surface shown in Fig. 3.2. After flash-cleaning and annealing in ultra-high vacuum, the surface facets into (111) and (331) planes easily observable with STM (Fig. 3.2a) and b)). For the precise determination of the facet angles LEED is very useful. Adsorption of foreign atomic or molecular species may modify the energetics of the surface and may stabilize other orientations. An example is provided by the planar Au induced reconstruction of the Si(553) surface shown in Fig. 3.2c). Whereas the pristine Si(553) surface facets into (111) and (331) areas, Au deposition allows to stabilize the Si(553) surface. It is also possible that deposition of foreign species on the surface induces the faceting of an otherwise stable surface. This is the case for the Si(331) surface, which breaks into the (111) and (110) facets upon Ag deposition [100].
Bulk-terminated vicinal silicon surfaces with orientations within the (100)-(110) plane or equivalently the (111)-(11$\bar{2}$) plane, may be classified within a simple scheme illustrated in Fig. 3.3. Let (n,n,n+2m) be a general direction lying in the (111)-(11$\bar{2}$) plane. Using the scalar product, the angle α between (n,n,n+2m) and (111) is easily determined

$$\alpha = \arccos \frac{3n + 2m}{\sqrt{3(3n^2 + 4m^2 + 4mn)}}.$$

Surfaces with $m > 0$ are lying between (111) and (100), surfaces with $m < 0$ are lying between (111) and (110). The number of (111)-like bilayer steps per period is given by $|m|$. The terrace width in the (11$\bar{2}$) direction, given in units of $\frac{1}{2}\sqrt{\frac{3}{2}}a$, is $n + \frac{2}{3}m$.
In what follows we discuss the structure of various silicon surface reconstructions. Each surface pursues a different strategy in order to minimize its total energy. As we will see there are a few universal building blocks which are often encountered in surface reconstructions.

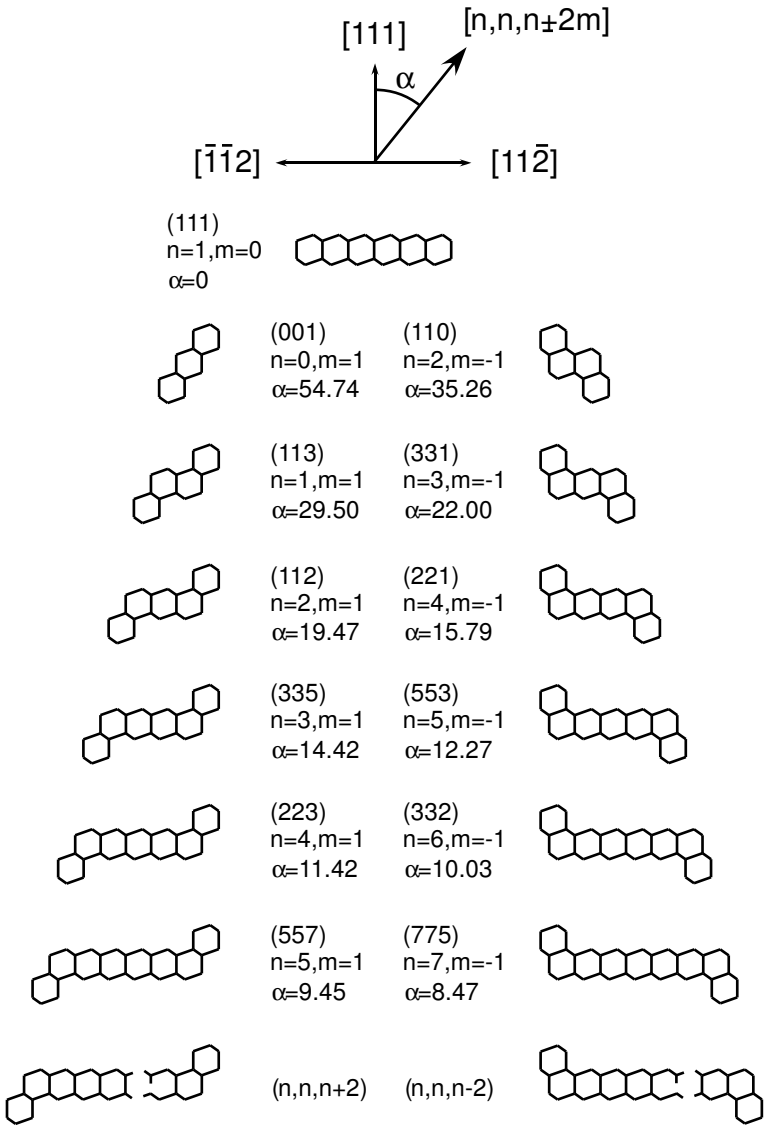

Figure 3.3: Overview on the family of bulk-truncated silicon surfaces viewed along $[\bar{1}10]$ exhibiting a single bilayer step per period ($|m| = 1$). For $|m| > 1$ terraces of different width are alternating.

3.2 Dimers

Dimers are found on Si(100)-(2×1). Si(100) is at the same time the simplest and currently the only technologically relevant surface of silicon. In 1958 Farnsworth *et al.* [23] reported that LEED of clean Si(100) produces half-integral diffraction spots indicating a two-domain (2×1) periodicity in real space. However, it was not before 1992, after the publication of the first low-temperature STM images [101], that a general consensus about its detailed atomic structure emerged. The history of the evolution of the atomic structural model of Si(100)-(2×1) and the many controversies that appeared in the course of time are retraced in Ref. [102]. Here we limit ourselves to the description of the generally accepted structural model. As can be seen from Tab. 3.1, the dangling bond density on the bulk-truncated Si(100) surface is high and thus the ideal (1×1) surface is structurally unstable. In order to minimize their energy, surface atoms on clean Si(100) move pairwise towards each other and form a new bond. This results in the symmetric dimer model shown in Fig. 3.4a). Remember that every surface atom on bulk-truncated Si(100) carries two dangling bonds. Thus the formation of the dimers reduces the number of dangling bonds by a factor of two, but each atom constituting the dimer carries a remaining dangling bond.

Dimerized Si(100)-(2×1) surfaces are obviously strained. The surface is under tension in the direction parallel to the dimer and under compression perpendicular to them [54]. Upon dimer formation the band structure energy is lowered by approximately 4 eV. However, the lattice distortion adds an elastic energy of the order of 2 eV, leading to a total reduction of the total energy of about 2 eV per dimer [54]. Using the dimer model two orthogonally oriented (2×1) domains are explained by dimers on terraces which are separated by single-layer steps. LEED diffraction patterns, which show one (2×1) domain only, should then be observed with samples which exhibit either no steps or bi-layer steps. Experimentally, single-domain Si(100) surfaces were obtained with vicinal surfaces, which were intentionally misoriented by more than 4^o towards [110].

Low-temperature STM images [101, 103] clearly showed that the dimers on Si(100) are buckled, i.e. the two atoms of the dimer have a different height above the surface plane. This observation confirmed the asymmetric or buckled dimer model (see Fig. 3.4b) and c)). Asymmetric dimers are also supported by LEED [79] and other techniques. Asymmetric dimers prefer higher periodicities, (2×2) and c(4×2), which appear because the direction of buckling of neighboring dimers is correlated. Unless stabilized by surface defects, correlation is partially destroyed around 200 K. Above this temperature LEED usually sees an average (2×1) order. At room temperature, dimers appear symmetric in STM images, since thermal vibrations flip the buckling direction of a dimer faster than what can be observed by STM.

The calculated electronic structure of the symmetric dimer model is metallic. ARPES however, clearly found an energy gap [104]. Subsequent calculations for the asymmetric dimer model indicated that buckling opens a gap between occupied and

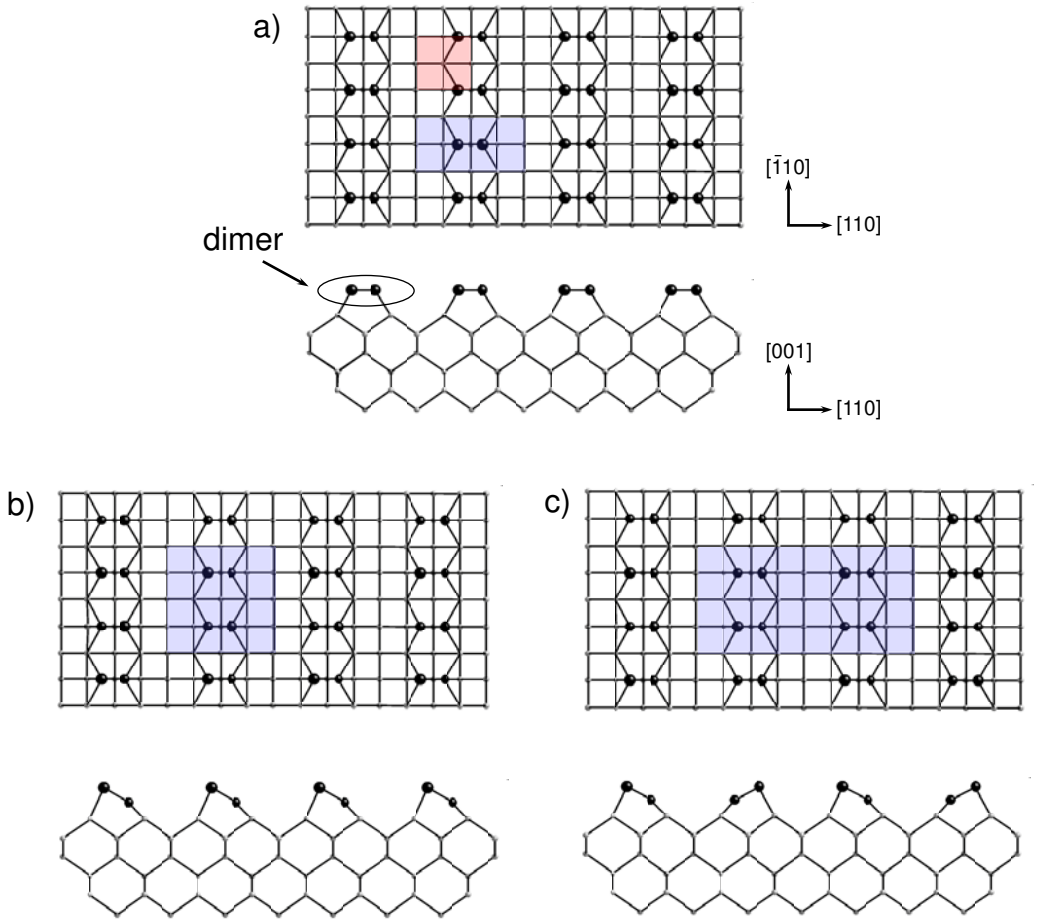

Figure 3.4: Models for the reconstructed Si(100) surface. a) Symmetric dimer model with (2×1) periodicity, b) asymmetric dimer model with (2×2) periodicity, c) asymmetric dimer model with c(4×2) periodicity. The (1×1) unit cell of the bulk-truncated surface is shown in red. The unit cell of the reconstruction is shown in blue.

empty surface states and lowers the surface energy by 0.46 eV per dimer [105].

3.3 Adatoms and restatoms

Besides the formation of dimers, adatoms saturate dangling bonds and thus contribute to a reduction of the total energy. Adatoms are observed on (111) surfaces of silicon and germanium. Here we first discuss the Ge(111)-c(2×8) reconstruction, because it is less complex than the famous Si(111)-(7×7) reconstruction. The Ge(111)-c(2×8) was identified in 1967 [106,107] by LEED. Its atomic model is shown in Fig. 3.5a). Whereas on bulk-truncated (100) surfaces each surface atom carries

two dangling bonds, surface atoms on bulk-truncated (111) surfaces only exhibit one dangling bond. Atoms with dangling bonds are arranged in a hexagonal layer and are only second-nearest neighbors (see Fig. 3.1). Their nearest neighbors are three subsurface atoms, with which they share a bond. These are also arranged in a hexagonal layer but shifted with respect to the surface layer. Together with their nearest neighbor subsurface atoms, the surface atoms form a bilayer with trigonal symmetry. Successive bulk bilayers are stacked in an ABC sequence. An additional atom, called an adatom (blue balls in Fig. 3.5a)), may saturate three adjacent dangling bonds, by forming three bonds, called backbonds, with the three nearest neighbor surface atoms. Its fourth orbital points towards the vacuum and is half-occupied. Thus an adatom reduces the number of dangling bonds by a factor of three. STM images (not shown) [108] clearly show four protrusions per c(2×8) unit cell corresponding to the four adatoms. Adatoms may occupy two types of sites. These geometries are distinguished as hollow (H_3) and atop (T_4) sites depending on whether the substrate atom below the adatom is found in the fourth or second layer. In H_3 sites the adatom is three-fold coordinated, in T_4 sites the adatom is approximately four-fold coordinated due to the substrate atom directly below in the second layer. The unambiguous discrimination between adatoms in T_4 and and H_3 sites was finally achieved by x-ray diffraction in 1990 [109] favoring the T_4 sites.
Of the 16 dangling bonds per c(2×8) unit cell on the bulk-truncated Ge(111) surface, the four adatoms saturate 12. However each adatom still carries one remaining dangling bond. So the number of dangling bonds per reconstructed c(2×8) unit cell is 8. The four surface atoms, whose dangling bonds have not been saturated by adatoms are called restatoms (green balls in Fig. 3.5a)).
The balance between the lowering in energy due to the reduction of dangling bonds and the energy increase caused by the bond distortion is very delicate. Compared to the Ge(111)-c(2×8) reconstruction, the Si(111)-(7×7) reconstruction is much more complex. Since its discovery in 1959 using low energy electron diffraction (LEED) [110], the (7×7) reconstruction of Si(111) has become the prototype for studying the complex reconstructions occurring at semiconductor surfaces. The intricate (7×7) LEED pattern is easy to reproduce and the sharpness of the LEED spots indicates exceptional long range order.
A mystery for many years, the atomic structure of Si(111)-(7×7) has been resolved by Takayanagi *et al.* in 1985 [41,42] on the basis of transmission electron diffraction (TED) data, assisted in part by the observation of adatoms in scanning tunneling microscopy images by Binnig *et al.* [111]. Their now widely accepted dimer-adatom-stacking fault (DAS) model consists of twelve adatoms (blue balls) in the first layer, a stacking fault bilayer (second and third layer), within which 9 dimers (small black balls) in the third layer border the triangular faulted and unfaulted subunits (see Fig. 3.5b)). The dimers observed on Si(111)-(7×7) are not the same as the ones observed on Si(100)-(2×1). Whereas the two atoms of a (100)-type dimer carry each one remaining dangling bond, the (111)-type dimers are completely saturated. It should be noted that dimers within the DAS model are not located at the top layer

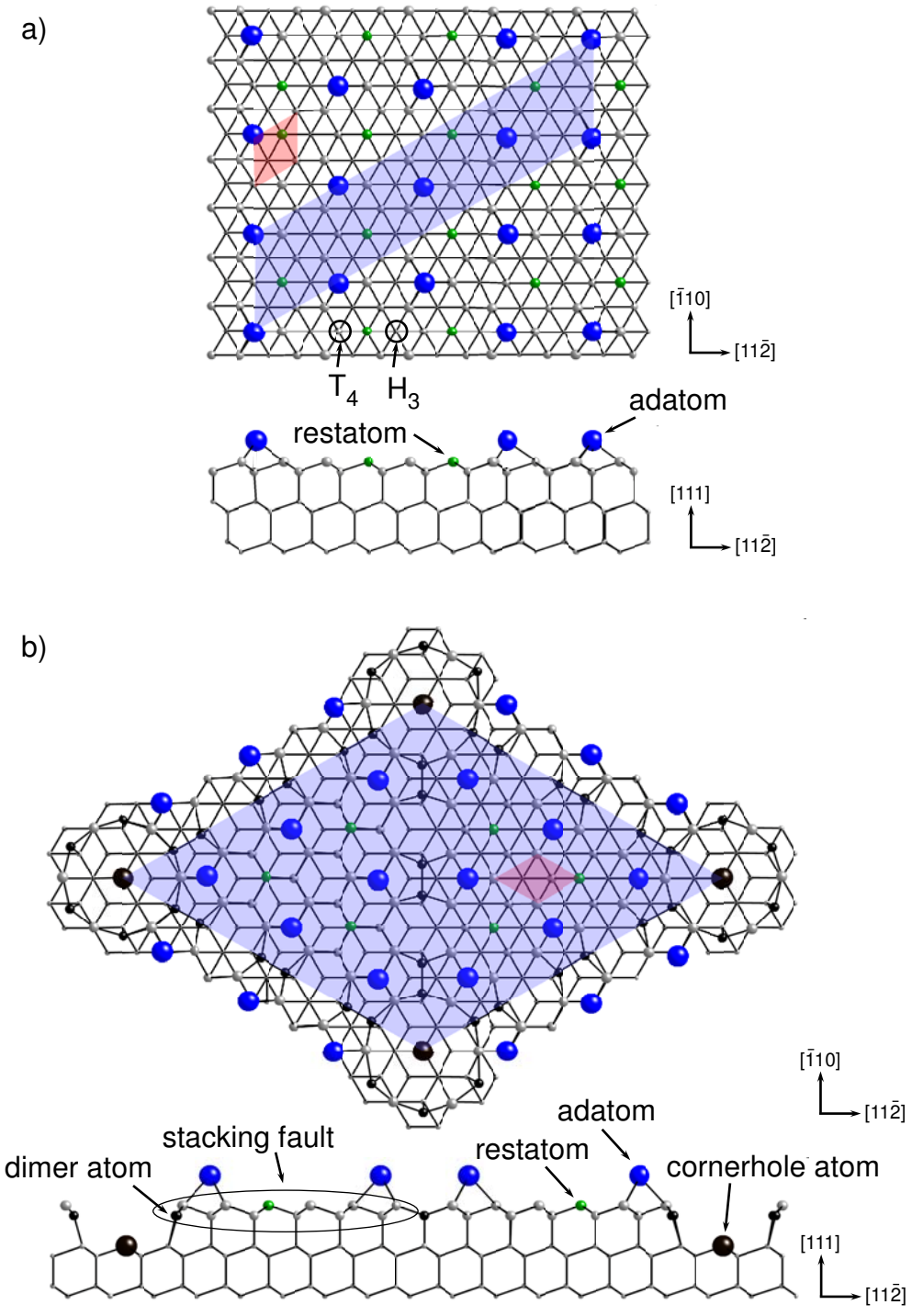

Figure 3.5: Atomic models for the (111) surface reconstructions of group IV semiconductors. a) Ge(111)-(2×8) and b) the DAS model for Si(111)-(7×7). Blue and green balls represent adatoms and restatoms respectively. The large black atoms represent the atoms below the corner hole. Small black atom are parts of dimers.

of the surface but within the third layer at the borderline between faulted and unfaulted areas. It is also interesting to note that it is the presence of the stacking fault which allows the formation of dimers by the atoms at the borderline, since atoms of the third layer in the interior of the faulted and unfaulted units exhibit bulk-like four-fold coordination. A deep vacancy, called the corner hole (above the large black atom) is located at each apex of the unit cell. The 6 three-fold bonded atoms (green balls) in the second layer falling in between the adatoms of each triangular subunit are rest atoms. Each unit cell contains 102 surface atoms, giving a coverage of $\Theta = 2.08$ ML with respect to the unreconstructed bulk-like surface.

The reconstruction of the surface is accompanied by the formation of a number of surface states lying within the bulk bandgap. The DAS model reduces the number of potential dangling bonds from 49 for the unreconstructed (7×7) unit cell to 19 (12 dangling bonds for the adatoms, 6 dangling bonds for the rest atoms and one dangling bond for the atom below the corner hole). These 19 dangling bonds deliver 19 electrons which fill the surface states. In order to reduce the energy of the surface, 14 electrons are transferred to fill the energetically more favorable rest atom and corner hole states. The remaining 5 electrons remain in the adatom bands at -0.2 eV, which have been observed by photoemission [56, 112–114] (see also Fig. 2.16). Furthermore a surface state at -0.8 eV has been identified with the restatom states, while the state at -1.8 eV arises from the backbonds between the adatoms and the first full atomic layer. Inverse photoemission shows a band at 0.5 eV associated with the adatoms and a higher lying unoccupied state at 1.5 eV.

Local tunneling spectroscopy measurements at specific locations allow to verify this identification [43] (see also Fig. 2.3 and Fig. 2.4). At room temperature the adatoms of the (7×7) cell give rise to substantial tunneling currents down to very low bias, indicating that they have a high density of states near E_F and are the origin of the metallic surface state observed in photoemission.

In addition to the well-known (7×7) reconstruction, regions of DAS-like (5×5) and (9×9) symmetry may be observed on highly stepped surfaces [115] (see for instance Fig. 3.2a)), on laser-annealed, sputter-annealed [116, 117], cleaved and annealed [118] samples as well as on surfaces grown by low-temperature molecular beam epitaxy [119]. This is evidence for the delicate energy balance between the reduction in energy due to the elimination of dangling bonds and the induced strain.

3.4 Tetramers and pentamers

Tetramers and pentamers are more complicated schemes to eliminate dangling bonds. Tetramers are found on Si(114) and Si(113). We first discuss the conceptually simpler Si(114)-(2×1) reconstruction shown in Fig. 3.6a).

The Si(114)-(2×1) reconstruction was first reported in 1993 [120]. A structural model was proposed by Erwin *et al.* in 1996 [121]. On the bulk-truncated Si(114)

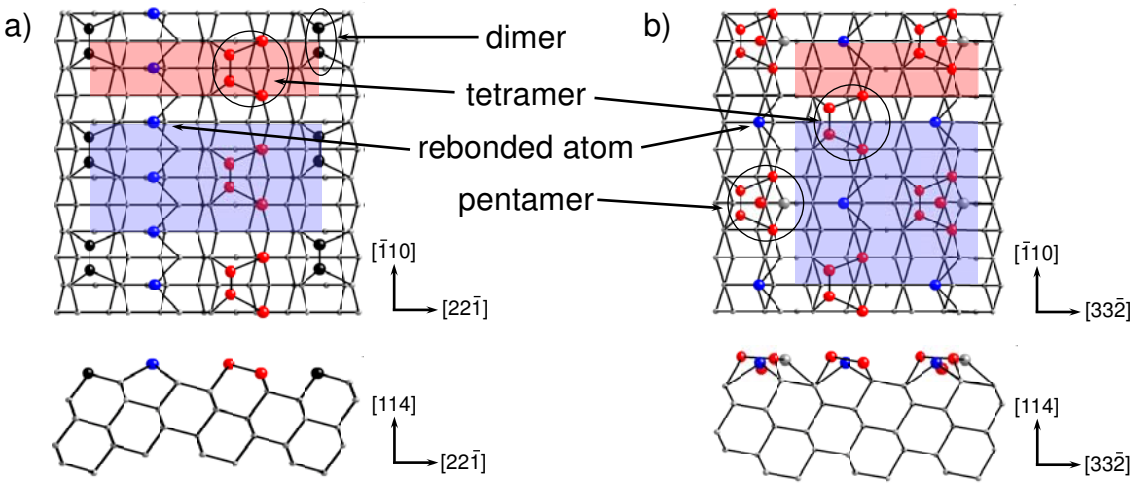

Figure 3.6: Atomic model for the reconstruction of the a) Si(114) and b) Si(113) surface. Red atoms are members of a tetramer or a pentamer. Blue atoms are rebonded atoms and the black atoms are part of a dimer.

surface both the (111)-like and the (100)-like surface atoms are observed carrying one and two dangling bonds respectively (see Fig. 3.1). Pairs of adjacent (100)-like surface atoms dimerize. The resulting structure formed by the (100)-like dimer and two neighboring (111)-like non-rebonded surface atoms is called a tetramer (red balls). It is topologically equivalent to the unit of a non-rebonded B-type step edge on Si(100) [121]. Its four dangling bonds result in two occupied states rendering the tetramer semiconducting. Furthermore the Si(114)-(3×1) structure contains a simple (100)-like dimer (black balls). The remaining two surface atoms per (2×1) unit cell, a (111)-type and a (100)-type, are replaced by an adatom (blue atom), sometimes called a rebonded atom, with three backbonds and one dangling bond.
The Si(113) surface reconstruction, reported in 1985 by Gibson *et al.* [122], has already been observed earlier by Olshanetsky *et al.* [123]. However, the later study appears to be based on Ni contaminated silicon samples.[1] The model proposed by Dabrowski *et al.* in 1994 [124] is shown in Fig. 3.6b). It shares several building blocks with the Si(114)-(2×1) surface. At room temperature Si(113) exhibits a (3×2) periodicity. Above 800 K, it changes into (3×1) [125]. The (113) bulk-truncated surface consists of alternating rows of (111)-like and (100)-like surface atoms. Pairs of adjacent (100)-like surface atoms dimerize and form tetramers together with the two neighboring (111)-like surface atoms. The remaining two surface atoms per (3×1) unit cell, a (111)-type and a (100)-type, are replaced by an adatom. These rebonded adatoms induce significant tension. One of the backbonds is stretched by

[1]The periodicity of the Si(331) reconstruction is known to change from (12×1) to (13×1) upon Ni contamination. Furthermore the (115) and (112) surfaces reported to be reconstructed are also expected to be Ni stabilized. See Ref. [115] for a complete overview of stable surfaces between (100) and (111).

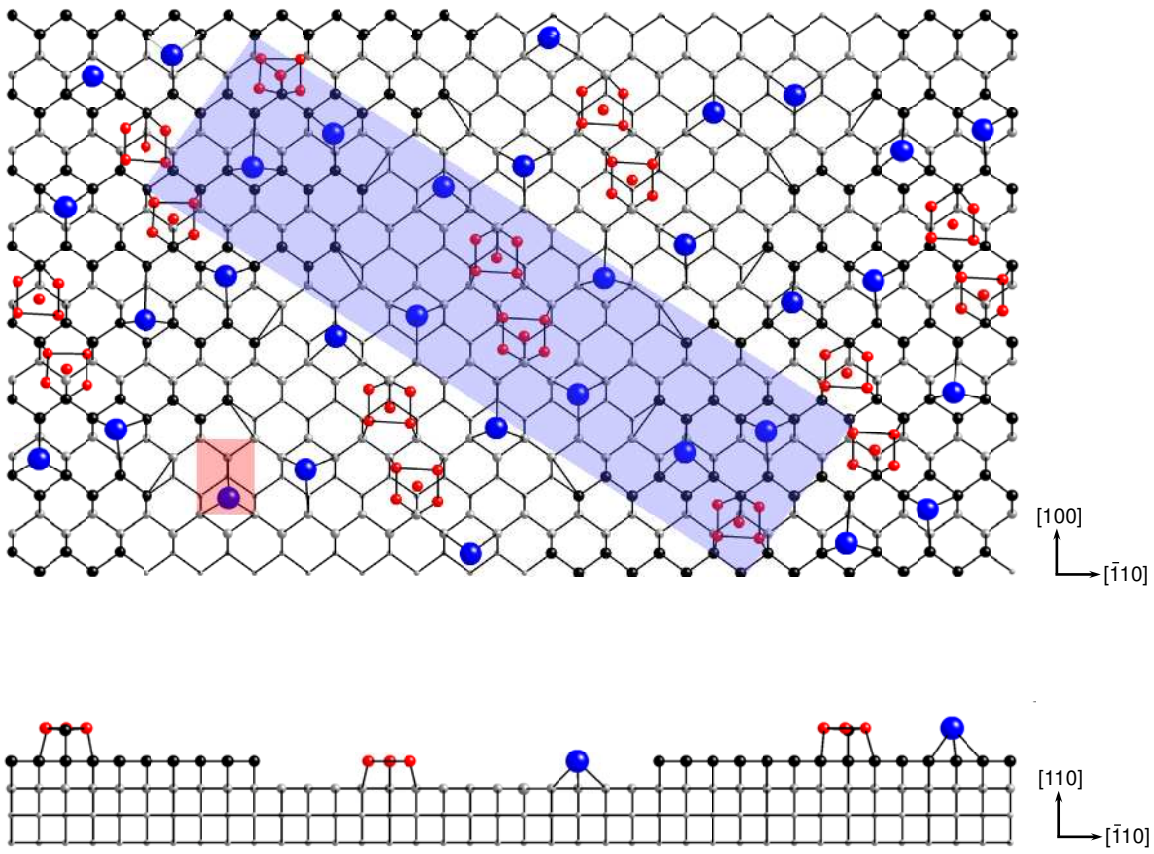

Figure 3.7: ATI model for the Si(110)-(16×2) reconstruction.

more then 5% [126]. Adatoms and tetramers may be arranged in a (3×1) order such that they alternate along [1̄10]. Taking into account the adatom, we now get 5 dangling bonds per unit cell, thus the structure is expected to be metallic. As noted before, metallic surfaces are unlikely to be stable. To solve this problem every second tetramer captures a Si interstitial atom (red ball) leading to the (3×2) periodicity observed at room temperature [102,124]. The interstitial affects the electronic structure of Si(113), changing the metallic (3×1) into a semiconducting (3×2) surface. The interstitial atom induces considerable compressive strain. The tension around the adatoms helps to compensate its lateral component. The vertical component of the strain is relieved as the structure relaxes strongly towards the vacuum, elevating a pentagonal ring of atoms. This pentamer, formed by the original tetramer and the common neighbor of the two (111)-like surface atoms is almost flat and parallel to the surface. Above 800 K, interstitial atoms may hop from one tetramer to the other [125]. Due to the missing correlation between hopping interstitial atoms, the periodicity observed by LEED is (3×1).
An atomic structural model containing a slightly different pentamer has been pro-

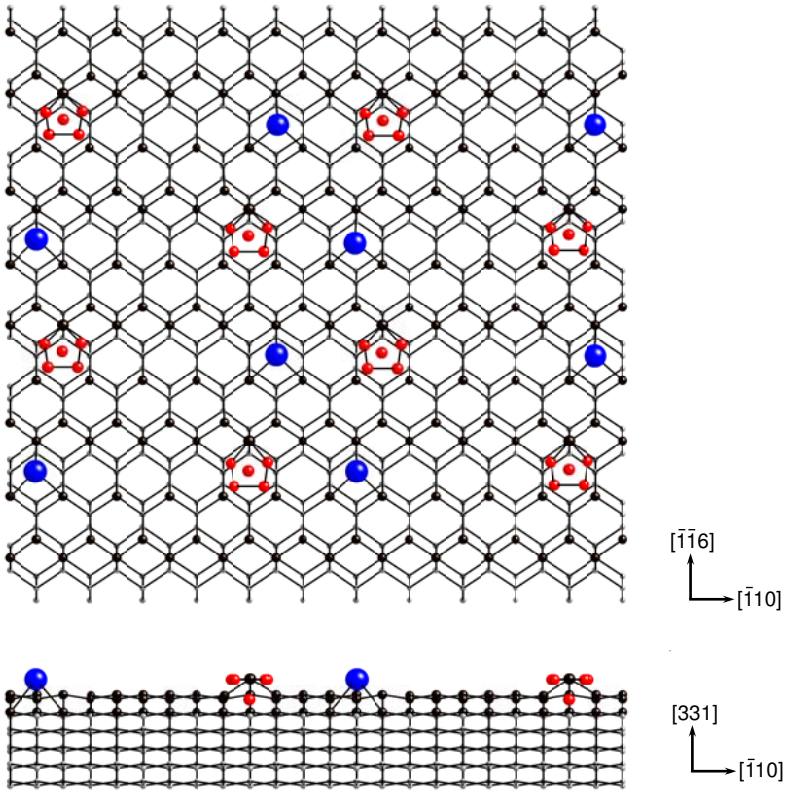

Figure 3.8: Our model for the Si(331)-(12×1) reconstruction.

posed [127] for the reconstruction of the Si(110) surface characterized by a $\begin{pmatrix} 11 & -5 \\ 2 & 2 \end{pmatrix}$ periodicity, usually denoted as (16×2). The bulk-truncated Si(110) surface consists of double rows of (111)-like surface atoms running along the [$\bar{1}$10] direction. Since all surface atoms of the bulk-truncated Si(110) surface are (111)-like, i.e. exhibiting three back-bonds and one dangling bond, the original pentamer must be modified. In the adatom-tetramer-interstitial (ATI) model [127, 128] shown in Fig. 3.7, pentamers, formed by four additional tetramer atoms and one additional interstitial atom, which must be provided by the steps, are used to interlink the double rows of surface atoms in a complex and beautiful way. In addition several adatoms and a surface step are required to account for the experimental observations. A total of 30 surface atoms of the bulk-truncated surface must be removed in order to create the step. 28 of these atoms are required to form the 8 adatoms and the four pentamers. 12 restatoms remain unsaturated. The ATI model remains to be verified by complementary experimental techniques. ARPES measurements including core-level spectra were recently published by Kim *et al.* [129].
In the next section, new experimental results for the Si(331)-(12×1) reconstruction

are presented, leading to a new structural model shown in Fig. 3.8. Similarly to Si(110), the bulk-truncated Si(331) surface consists exclusively of (111)-like surface atoms. These are arranged in alternating single and double rows running along the $[\bar{1}10]$ direction. This is a slightly different starting configuration compared to the bulk-truncated Si(110) surface on which all dangling bonds are arranged in double rows. However, locally the Si(331) can be viewed as consisting of (110) like terraces separated by steps running along the $[\bar{1}10]$ direction. On the bulk-truncated Si(331) surface, the presence of steps breaks the two-fold rotation symmetry of the (110) surface, only a mirror plane perpendicular to the steps is retained. This symmetry breaking is responsible that all pentamers on Si(331) point towards the $[\bar{1}\bar{1}6]$ direction, whereas on Si(110) pairs of pentagons pointing in opposite directions are observed.

3.5 A new structural model for Si(331)-(12×1)

C. Battaglia,[1] K. Gaál-Nagy,[2] C. Monney,[1] C. Didiot,[1] E.F. Schwier,[1] M. G. Garnier,[1] P. Aebi,[1]

[1] *Institut de Physique, Université de Neuchâtel, 2000 Neuchâtel, Switzerland*
[2] *Dipartimento di Fisica and ETSF, Università di Milano, 20133 Milano, Italy*

To be published

A new structural model for the Si(331)-(12×1) reconstruction is proposed. Based on scanning tunnneling microscopy images of unprecedented resolution and low energy electron diffraction data, we demonstrate that the reconstructed Si(331) surface shares the same elemental building blocks as the Si(110)-(16×2) surface, establishing the pentamer as an additional universal building block for silicon surface reconstructions.

The study of semiconductor surface reconstructions has been an area of active research for many years and has gained tremendous importance with the advent of low-dimensional heteroepitaxial semiconductor nanostructures such as quantum dots and quantum wires [130]. Due to the creation of broken bonds, called dangling bonds, a bulk-truncated surface is highly unstable. In order to lower its surface energy, the surface adopts a variety of strategies allowing to reduce the number of dangling bonds. Two of the most important mechanisms, encountered for instance in the prototypical Si(111)-(7×7) reconstruction [41], are the formation of dimers, where two surface atoms pair up to eliminate their dangling bonds, and the formation of adatoms, which bond to three surface atoms thus transforming three dangling bonds into one. An important step towards the understanding of high-index group IV surfaces with a surface normal in between the (111) and (100) direction was the introduction of an additional reconstruction element by Dabrowski *et al.* [131], a six-fold coordinated surface self-interstitial which is captured by a conglomerate of surface atoms [125, 132]. This concept was subsequently adapted by An [127] and theoretically analyzed by Stekolnikov [128, 133] to explain the pair of pentagons observed in scanning tunneling microscopy (STM) images of the reconstructed Si(110) surface.

Here we focus on the atomic structure of the Si(331)-(12×1) reconstruction. Its surface normal is located 22.0^o away from the (111) direction towards (110) (see Fig. 3.9a). Si(331)-(12×1) is an important surface since it is the only confirmed planar silicon surface with a stable reconstruction located between (111) and (110). In this report, we present high resolution STM images resolving for the first time rows of pentagons very similar to the ones observed on Si(110)-(16×2). Since its discovery more than 17 years ago [24] several structural models containing dimers

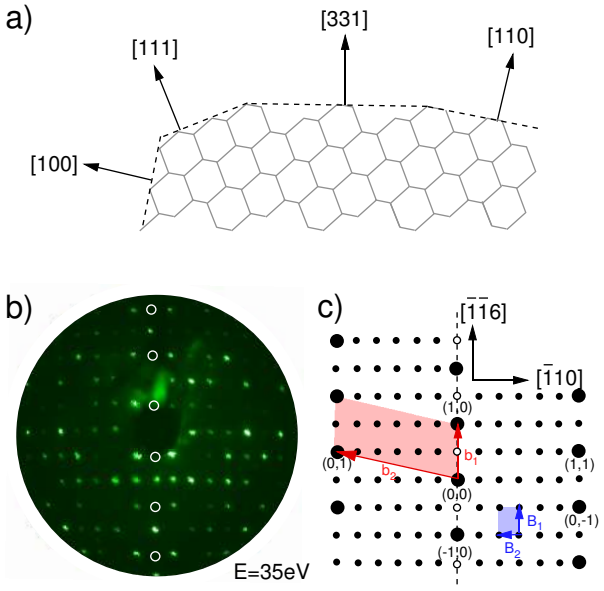

Figure 3.9: (Color online) a) Side cutaway showing the crystal lattice of silicon in the $(\bar{1}10)$ plane. The dashed line follows the bulk-terminated surface for several important orientations. b) Experimental LEED pattern at beam energy 35 eV. The position of missing spots is indicated by the white circles. c) Sketch of the LEED pattern with (1×1) (red) and (12×1) (blue) reciprocal unit cell and spot labels (black). The bulk directions are also given. The position of the missing spots is indicated by empty black circles. The orientation of the glide plane is indicated by a dashed line.

and adatoms have been proposed [134, 135]. However, none of these models is able to explain the pentagons observed in our STM images. Combining the complementary strength of STM and low energy electron diffraction (LEED), we derive a new structural model containing surface self-interstitials as basic building blocks.

Sample preparation and experiments were carried out in an ultra-high vacuum chamber with a residual gas pressure below 3×10^{-11} mbar equipped with an Omicron LT-STM and Omicron Spectaleed LEED/Auger optics. Boron doped Si(331) samples from CrysTec with a resistivity of 0.1-30 Ω cm were slowly degassed by direct current heating up to 1060^{o}C while keeping the pressure below 5×10^{-10} mbar, followed by subsequent cleaning via repeated flashing to 1260^{o}C and slow cooling across the (1×1) to (12×1) phase transition at 810^{o}C [24]. This procedure gives an almost perfectly ordered surface with a very low number of defects. Special care was taken in order to avoid Ni contamination. STM measurements were performed at 77 K using etched W tips.

Figure 3.9b) presents a normal incidence LEED pattern of the Si(331)-(12×1) reconstruction along with a sketch in Fig. 3.9c) containing reciprocal lattice vectors and spot labels (h, k) choosing the bulk-terminated surface as the reference for in-

dexing. The reciprocal unit cell vectors $\mathbf{B}_1$ and $\mathbf{B}_2$ of the reconstructed surface can be expressed using the reciprocal unit cell vectors $\mathbf{b}_1$ and $\mathbf{b}_2$ of the bulk-terminated (331) surface.

$$\begin{pmatrix} \mathbf{b_1} \\ \mathbf{b_2} \end{pmatrix} = \begin{pmatrix} 2 & 0 \\ 1 & 6 \end{pmatrix} \begin{pmatrix} \mathbf{B_1} \\ \mathbf{B_2} \end{pmatrix}$$

However, since in general we find 11 satellite spots in between the integer spots along the $[\bar{1}10]$ direction, the reconstruction is conventionally called the (12×1) reconstruction. Inspecting the spot intensities in the LEED patterns in Fig. 3.9b) we immediately notice the mirror symmetry of the LEED pattern along the $[\bar{1}\bar{1}6]$ direction. Furthermore, a careful analysis of the LEED spot intensities as a function of energy (not shown) reveals that systematically *all* half-order spots $(\pm nh/2, 0)$, n being an odd integer, are missing for *all* beam energies (see empty circles in Fig. 3.9b) and c). Although spot intensities vary as a function of energy and even vanish at some energies due to diffraction effects, the $(\pm nh/2, 0)$ spots exhibit no intensity at *all* beam energies. Such missing spots indicate the existence of a glide plane along $[\bar{1}\bar{1}6]$ in real space [136]. Intuitively this can be understood in the following way. Since the scattering phase shifts of atoms are functions of energy, the presence of missing spots at all energies implies that the unit cell of the surface structure must contain two or more identical groups of atoms related by the glide plane symmetry, because electron waves scattered from different groups of atoms can not cancel one another for some reflection at all energies [137]. Furthermore, if the incident wave vector lies in a plane parallel to the glide plane, as is trivially true at normal incidence, the glide plane in real space results in a reflection symmetry for the LEED intensities (though not for the amplitudes) [138]. Thus LEED firmly establishes the presence of a glide plane in the structure.

We now turn to our STM data. The large scale topography image presented in Fig. 3.10a) shows the high quality of the surface. Besides the perfect long range order only a few local defects are present on the surface. As observed already by other groups [135, 139–143], the Si(331)-(12×1) reconstruction consists of similar mounds arranged into zigzag chains running along the $[\bar{1}\bar{1}6]$ direction separated by trenches. Focusing now on the high resolution image in Fig. 3.10b) we see that each of the mounds is formed by five protrusions forming a pentagon. A further protrusion may be identified linking two successive pentagons within the same chain. Pentagons with the same dimensions were already observed on Ge(110)-c(8×10) [144, 145] as well as on Ge(110)-(16×2) [144] and on Si(110)-(16×2) [127]. However, we would like to point out that this is the first observation of such pentagons on a surface away from the (110) orientation, indicating their high stability and confirming their fundamental role as an elemental building block in semiconductor surface reconstructions.

Inspired by structural elements encountered on reconstructed Si(113) and Ge(113) surfaces [125, 131], An *et al.* [127] have proposed an adatom-tetramer-interstitial (ATI) model for the pentagons observed on the (110) surfaces. Its stability has subsequently been tested theoretically by means of first-principles total energy cal-

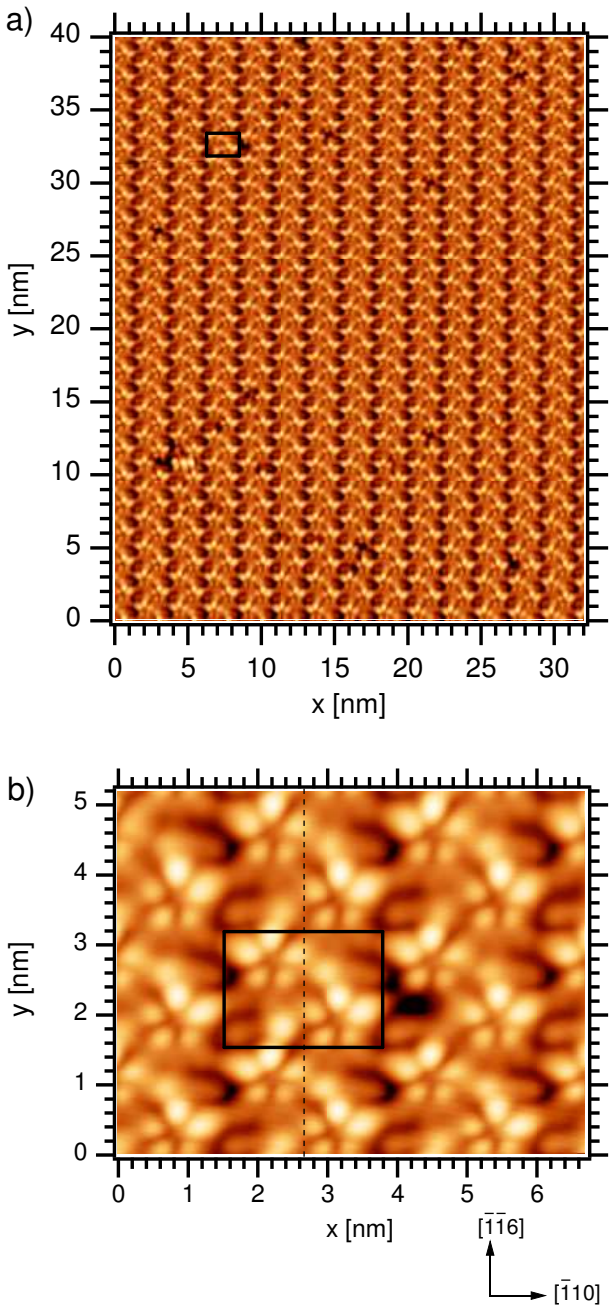

Figure 3.10: (Color online) a) Large scale STM topography of the annealed Si(331) surface. b) High resolution image with unit cell (full line) and the glide plane (dashed line) indicated. Bias voltage 2.0 V, set-point current 0.06 nA.

culations [133]. Recently Stekolnikov *et al.* [128] proposed a coherent structural model for the Si(110)-(16×2) reconstruction obtained by combining the ATI model with a regular step arrangement.

In what follows, we develop a coherent structural model for the Si(331)-(12×1) reconstruction based on the ATI model and discuss similarities and differences with the (110) case. In a first step we need to determine the registry of the surface reconstruction with respect to the bulk. Here the occurrence of the glide plane symmetry gives us the clue. Inspection of Fig. 3.10b) shows that a glide plane is found at the center of the zigzag chain (dashed line) consistent with the observation of missing spots in the LEED pattern. The glide plane found on the surface must also be a glide plane of the bulk, since the space group of the bulk contains all symmetry elements of the surface. The top layer of the bulk terminated Si(331) surface is shown in Fig. 3.11b) along with a side view in Fig. 3a). The dashed line represents the glide plane. Fig. 3.11c) offers a graphical proof for the existence of the glide plane in the bulk. After mirror reflection along the glide plane line, a translation by half the unit vector $-\mathbf{A}_1/2$ is necessary to obtain the original registry.

After determining the registry of the surface reconstruction with respect to the $[\bar{1}10]$ direction we now need to study the registry with respect to the $[\bar{1}\bar{1}6]$ direction. Here we benefit from a comparison with the Si(110) surface shown schematically in Fig. 3.11e) and f). For a sketch of the complete model for the Si(110)-(16×2) reconstruction including the steps along $[\bar{1}12]$ see Ref. [128]. According to the ATI model for the Si(110) surface, the pentagon seen in STM images consists of four adatoms (*a*,*b*,*c*,*d*, empty circles) forming the tetramer and one surface atom (*e*, black dot) belonging to the first atomic layer (see Fig. 3.11d)). The six-fold coordinated interstitial atom (*f*, empty circle) is located at the center of the pentagon slightly below the tetramer plane and consequently not directly visible in STM images (see simulated STM images in Ref. [128]). The resulting structural element formed by tetramer, atom *e* and *f* combined is called a pentamer [128].

In order to integrate the pentamer building block into our model we note that the arrangement of dangling bonds represented by black dots and marked by the double headed arrows in Fig. 3.11 differs between the Si(110) and Si(331) surface. Whereas dangling bonds on the Si(110) surface occur in double rows running along $[\bar{1}10]$, double rows alternate with slightly lower lying single rows of dangling bonds on the bulk-terminated Si(331) surface. For the Si(110) structure, atom *e* actually belongs to one of these dangling bond double rows. Consequently we also anchor the two pentamers per (12×1) unit cell required by STM on the double dangling bond row of the bulk-terminated Si(331) surface. It is important to note that anchoring the pentamers in this way provides exactly the same local binding configuration as on the Si(110) surface, since careful comparison of the sideviews in Fig. 3.11a) and e) reveals that the bulk-truncated Si(331) surface can be viewed as a highly stepped Si(110) surface. The position of the pentagons selected that way agrees with the position observed in the STM images (see STM image behind the model in Fig. 3.11b). Note also that the single dangling bond row is slightly lower lying

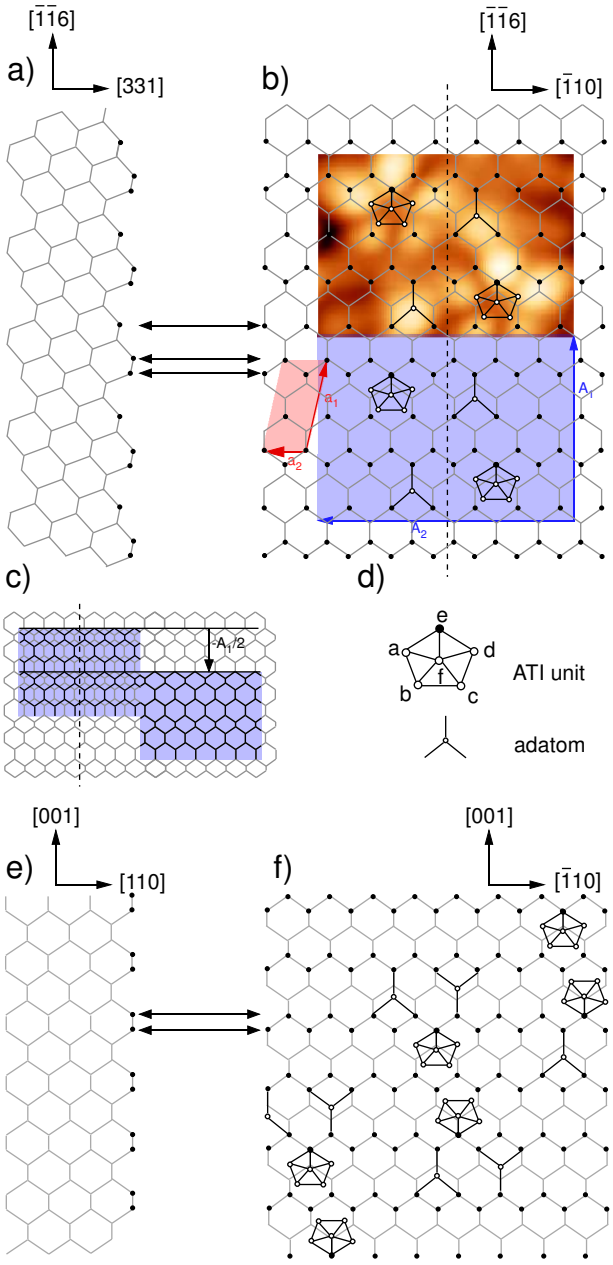

Figure 3.11: (Color online) a) Side and b) top view of the Si(331) surface. Black dots indicate the position of dangling bonds, some of which are saturated by pentamers and adatoms (empty circles). The (1×1) (red) and (12×1) (blue) unit cells are shown. For comparison with experiment an STM image is underlaid. The dashed line represents the glide plane. c) Graphical proof for the existence of the glide plane. d) Sketch of the pentamer and the adatom with atom labels. e) Side and f) top view of the Si(110) surface.

in agreement with the lower intensity of the lobes associated with adatom b and c in the STM image of Fig. 3.10b).
Each pentamer saturates five of the surrounding dangling bonds [133]. By introducing two pentamers per Si(331)-(12×1) unit cell, the number of dangling bonds has been reduced from 36 to 26. Some of the remaining dangling bonds are saturated by simple adatoms as in the case of the Si(110) surface. In the STM image in Fig. 3.10b) the additional protrusion linking two successive pentamers may indicate the location of a first adatom. After placing these adatoms there are a total of $26 - 2 \times 3 = 14$ restatoms per unit cell (the factor of two is due to the glide plane symmetry). Stekolnikov *et al.* [128] have noted that it is energetically more favorable to leave some restatoms unsaturated than to introduce the maximum number of adatoms into the model. This allows further energy minimization by electron transfer from the adatom to the restatom as in the Si(111)-(7×7) reconstruction.
It is clear that at this point total energy calculations are required in order to determine the optimum adatom arrangement and the relaxed coordinates of each atom. Going back to the high resolution STM image in Fig. 3.10b), we see for instance that an individual pentagon does not exhibit a mirror symmetry along the $[\bar{1}\bar{1}6]$ direction indicating a distortion of the pentagon in order to reduce internal strain. It is also interesting to note that on the Si(110) surfaces, pentamers always occur in twin pairs rotated by 180^o with respect to each other, whereas on Si(331) all pentamers point into the same direction and are further apart from each other. Comparing the transition temperature of 810^oC [24] for Si(331)-(12×1) with 730^oC [146] for Si(110)-(16×2), it appears that it is actually the Si(331) which is the more favorable surface for pentamer formation (for comparison the transition temperature of 870^oC [95] for the Si(111)-(7×7) reconstruction is slightly higher). Here again, total energy calculations allow to quantify the trade-off between surface dangling bond reduction and induced surface stress and to analyze the details of the bonding configuration.
In summary, by combining our LEED and STM data and by comparing similarities and differences between the Si(331)-(12×1) and Si(110)-(16×2) reconstruction, we have derived a complete structural model for the Si(331) surface containing the pentamer as an essential ingredient. Thus besides adatoms, dimers and tetramers, pentamers emerge as a universal building block for silicon surface reconstructions.

Stimulating discussions with Antje Schmalstieg, Georg Held, Pascal Ruffieux and Oliver Gröning are gratefully acknowledged. Skillfull technical assistance was provided by our workshop and electric engineering team. This work was supported by the Fonds National Suisse pour la Recherche Scientifique through Div. II and MaNEP.

3.6 Open questions and conclusion

Due to the high complexity of silicon surface reconstructions, the determination of their structure remains a formidable challenge. Based on our experimental results and lessons learned from other reconstructions, we are able to propose a new structural model for the Si(331)-(12×1) reconstruction involving pentamers and adatoms as elementary building blocks. This model now has to be tested by complementary methods. DFT calculations to determine relaxed coordinates and the lowest energy adatom configuration for our model are underway. Due to the large unit cell of the Si(331)-(12×1) reconstruction, these calculation are very demanding in computer resources. Once relaxed coordinates are obtained, IV-LEED calculations can be started. High quality IV-LEED data has already been acquired and is ready for analysis. But due to the large unit cell, it is not clear if these calculations may be performed on our own computers.
Results from DFT will also enable to compare the calculated electronic bandstructure with experiment providing a further test for the structural model. ARPES measurements are currently performed. Furthermore preliminary STS data has also been acquired at room temperature and at $T = 77$ K. At room temperature a surface state at 0.5 eV and at -0.8 eV has been identified separated by a small gap. The precise localization of these states in real space has not yet been determined. With the current boron concentration of 10^{15}-10^{16} cm^{-3} the spectra are already strongly shifted at $T = 77$ K making it impossible to image the surface at negative bias and even for a bias of -10 V no tunneling current is obtained. It is not clear if measurements at $T = 5$ K are feasible, since the increased doping concentration necessary at low temperature might disorder the reconstruction. Varying the dopant type and dopant concentration will also answer the question, if the Fermi level at the surface is pinned.

Chapter 4

Atomic chain reconstructions

In the following sections we discuss structural and electronic properties of atomic chains. Section 4.1 gives a quick overview over the two main classes of atomic chains. Our work mainly focuses on the first class of atomic chains, the semiconducting silicon honeycomb and Seiwatz chains, which are stabilized by a large number of adsorbates. In sections 4.2, 4.3 and 4.4 we review the literature of these atomic chain systems and highlight open questions. In section 4.5 we present new results on the Gd induced chain system which show that these chains also belong to the honeycomb and Seiwatz chain family. This is an important result, since Gd is the first adsorbate in a trivalent valence state, which is shown to stabilize these chains. Combining information from the literature for monovalent and divalent adsorbates with our results on trivalent adsorbates, we discovered a new systematics in the self-assembly process, which is discussed in detail in section 4.6. The stability of the various chain systems is tested using first-principles methods in section 4.7. Finally in sections 4.8 and 4.9 we discuss implications of our results on the second class of atomic chain systems induced by In and Au respectively. We conclude with an outlook to further investigations in section 4.10.

4.1 Adsorbate induced atomic chains

When a foreign atom or molecule is adsorbed on a surface, the energetics of the surface is modified and a new structure may be stabilized. Deposition of adsorbates on semiconductor surfaces generates a rich variety of low-dimensional surface structures. Surface orientation, adsorbate type, coverage, deposition and annealing temperature may all be chosen and determine the final structure. Most experimental efforts concentrate on structures grown on Si(111) and Si(100) surfaces. In recent years however, more and more studies include also high-index surfaces [27, 28, 147–188]. Possible adsorbates range from atomic species such as hydrogen atoms [189–196] up to the heaviest of all rare earth metals, lutetium [197], but also complex molecules [198–200] may be considered. A compilation of known

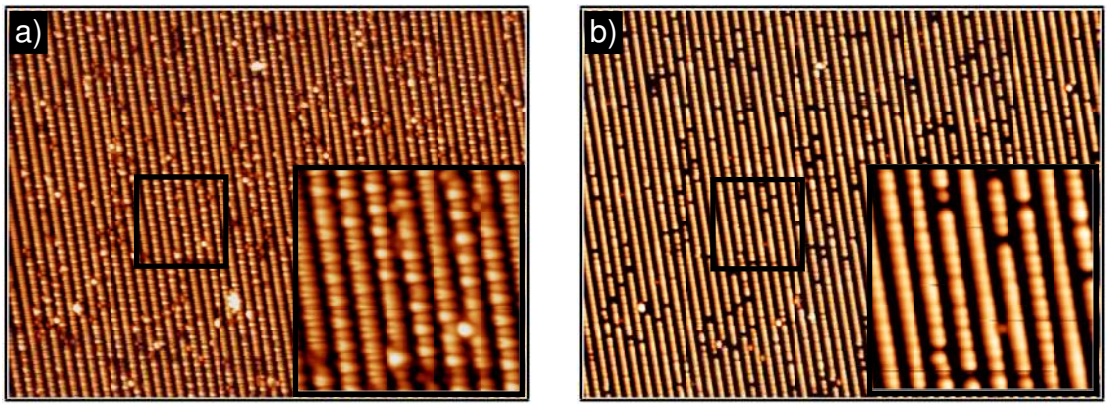

Figure 4.1: STM images of the Au/Si(553) atomic chain system recorded in dual mode at T=77 K. a) U=1V, b) U=-1V, I=0.1 nA, 60 nm × 45 nm, inset 10 nm × 10 nm.

surface phases on silicon surfaces up to 1994 may be found in Ref. [201].
Atomic chains belong to the class of adsorbate induced surface reconstructions. As for the reconstruction of pristine silicon surfaces, adsorbate induced surface reconstructions may stabilize large unit cells involving a highly complex atomic architecture. Due to the lack of a chemically sensitive probe with atomic resolution, the determination of the structure of adsorbate induced surface reconstructions adds an additional challenge compared to the determination of the structure of the pristine silicon surface reconstructions. A given adsorbate may induce several different reconstructions. The crucial parameters selecting a given reconstruction are usually the local coverage and deposition temperature. A certain activation temperature is often required before the pristine silicon surface reconstruction breaks down and transforms into the new adsorbate induced reconstruction.

Among hundreds of known adsorbate induced surface reconstructions, self-assembled atomic chains have attracted immense interest due to their quasi one-dimensional electronic properties. Atomic chains may be separated in two different classes. The first class of atomic chain systems consists of the honeycomb and Seiwatz chain family induced by a large number of adsorbates. These chains are semiconducting and exhibit a series of different translational periodicities depending on the adsorbate type and coverage. The second class consists of the Au induced chain systems Au/Si(111), Au/Si(553), Au/Si(775), Au/Si(110), Au/Si(335), Au/Si(557) and the In/Si(111) system. Some of these chains are metallic at room temperature, but undergo complicated metal-insulator transitions upon cooling. In Fig. 4.1 we present STM images of the Au/Si(553) chains measured at T=77 K. In the empty state image in a), one clearly observes local ×2 or ×3 modulations along the chains, which can be correlated with the opening of an energy gap at the Fermi energy in a half and one third filled electronic band due to a Peierls transitions. More details on this system are given in section 4.9 .

In the next three sections the literature of the the alkali metal, alkaline earth metal and rare earth metal induced atomic chains, belonging to the first class, is reviewed followed by new results obtained during this thesis.

4.2 Alkali metal induced chains

When deposited at temperatures close to the desorption regime, 1/3 ML of monovalent alkali metals (AM=Li, Na, K, Rb, Cs) [202–205] as well as the noble metal Ag [204, 206] induces a (3×1) reconstruction on Si(111) and Ge(111) surfaces.[1] The first structural models proposed for the (3×1) phase featured single rows of adsorbates at a coverage of 1/3 ML, with the adsorbate located on top of the Si surface atoms or in three-fold coordinated H_3 or four-fold coordinates T_4 sites of the bulk-terminated surface [203, 211–214]. These seemed to be able to explain first STM images presented in 1987 [215]. Since the unreconstructed surface consists entirely of six-member rings of Si atoms in the [$\bar{1}$10] direction, these models have a surface layer, which is denoted by (666666). One of these models studied by Erwin in Ref. [118] is shown in Fig. 4.2a).
In 1989, Fan and Ignatiev [204, 216] noted the similarity of IV-LEED curves for the (3×1) structures induced by different adsorbates and concluded that the superstructure is not just due to an ordered overlayer of adsorbates but that the adsorbates serve to induce a surface reconstruction of the substrate. They proposed a missing-row model (660660) [216] built exclusively from silicon atoms to account for the double rows observed in STM images [215]. Although most studies determined a coverage of 1/3 ML, the precise coverage remained controversial for a long time [217–220]. Only around 1996 a consensus seemed to be reached that the coverage is 1/3 ML. An adapted missing row model with a coverage of 1/3 ML is shown in Fig 4.2b).
In 1994 several groups independently suggested a structure which is a variant of the Seiwatz chain model [221], originally proposed for the Si(111)-(2×1) reconstruction. It consists of parallel π-bonded chains formed by five-member rings of Si atoms, separated by empty channels (500500) accommodating the adsorbate (see Fig. 4.2c)). This model, sometimes also called the missing top layer model has been proposed with a coverage of 1/3 ML [222–224] but also with 2/3 ML [210]. In 1995, Erwin proposed to extend Pandey's π-bonded chain model (575757) [225], which is now widely accepted as the atomic geometry of the clean Si(111)-(2×1) reconstruction, by the insertion of a six-member ring (567567) [118] (see Fig. 4.2d)). This is essentially the same model as the one proposed by Okuda *et al.* [226]. LDA total energy calculations showed that the extended Pandey model with 1/3 ML is energetically only slightly more favorable than the Seiwatz model with 1/3 ML [118, 227]. How-

[1] The Ag system is a more complicated since the (3×1) structure changes into (6×1) followed by c(12×2) when cooling below approximately 500 K [207] and 100 K [208, 209] respectively. For Ag, even a (5×2) reconstruction has been observed [210], probably at a coverage below 1/3 ML.

ever, in an alternative LDA study, the Seiwatz model was favored over the extended Pandy model [228].
STM studies [229, 230] revealed that the formation of the (3×1) reconstruction is accompanied by pronounced mass transport, which implies that the number of Si atoms in the (3×1) and (7×7) phase is different. In 1998, based on a Si mass transport analysis during the transformation of the clean (7×7) into the (3×1) reconstruction using STM, Saranin and coworkers [231–233] determined the Si surface atom density of the (3×1) reconstruction to be 4/3 ML, a value compatible with neither the Seiwatz model nor the extended Pandey model. Based on this observation, Saranin *et al.* [232] proposed a new structural model, the so-called double-π-bonded chain model DπC shown in Fig. 4.2e), containing two π-bonded Seiwatz-like chains, which are connected by the adsorbate atoms.
Today's widely accepted honeycomb chain-channel (HCC) model shown in Fig. 4.2f) was proposed independently in 1998 by Collazo-Davila *et al.* [234] based on transmission electron diffraction data and Lottermoser *et al.* [227] who performed LEED and surface x-ray diffraction experiments. LDA total energy calculations by Erwin and Weitering and others [227, 235–237] showed that this model is by far the most stable of any proposed so far and calculated electronic properties are in agreement with data from ARPES [208, 223, 238–242], core-level spectroscopy [208, 242, 243] and STM [209, 210, 215, 229–233, 244–252]. The HCC reconstruction consists of consecutive five-member and six-member rings separated by a channel (560560) accommodating the adsorbate atoms. There are four inequivalent Si surface atoms (labeled *a*, *b*, *c*, *d*) which form a honeycomb chain lying in a plane parallel to the surface. Each of these surface Si atoms is threefold coordinated: outer atoms *a* and *d* roughly tetrahedrally, inner atoms *b* and *c* in a planar configuration. Atoms *b* and *c* are only weakly bonded to the Si atom *e* below, but are linked to each other by a Si double bond, which is primarily responsible for the stability of the HCC model. The alkali metal atom sits in a channel formed by neighboring honeycomb chains and is fully ionized. It thus plays the role of an electron donor. The adsorbate density is 1/3 ML. The density of top Si atoms in the HCC model is 4/3 ML consistent with the experimental results of Saranin and coworkers [231, 232].

The HCC model has five unsaturated surface orbitals, and so should give rise to five surface states. There are six electrons to fill these states: four from the Si surface atoms (*a*, *b*, *c*, *d*), one from the alkali metal atom, and one from atom *e*. We thus expect three filled and two empty surface states in agreement with ARPES and LDA results.

4.3 Alkaline earth metal induced chains

Divalent alkaline earth metals (AEM=Mg, Ca, Sr, Ba) [238, 253–257] as well as divalent rare earth metals (RE=Sm, Eu, Yb) [258–260] induce a coverage dependent series of reconstructions on Si(111) differing in periodicity. In order of increasing

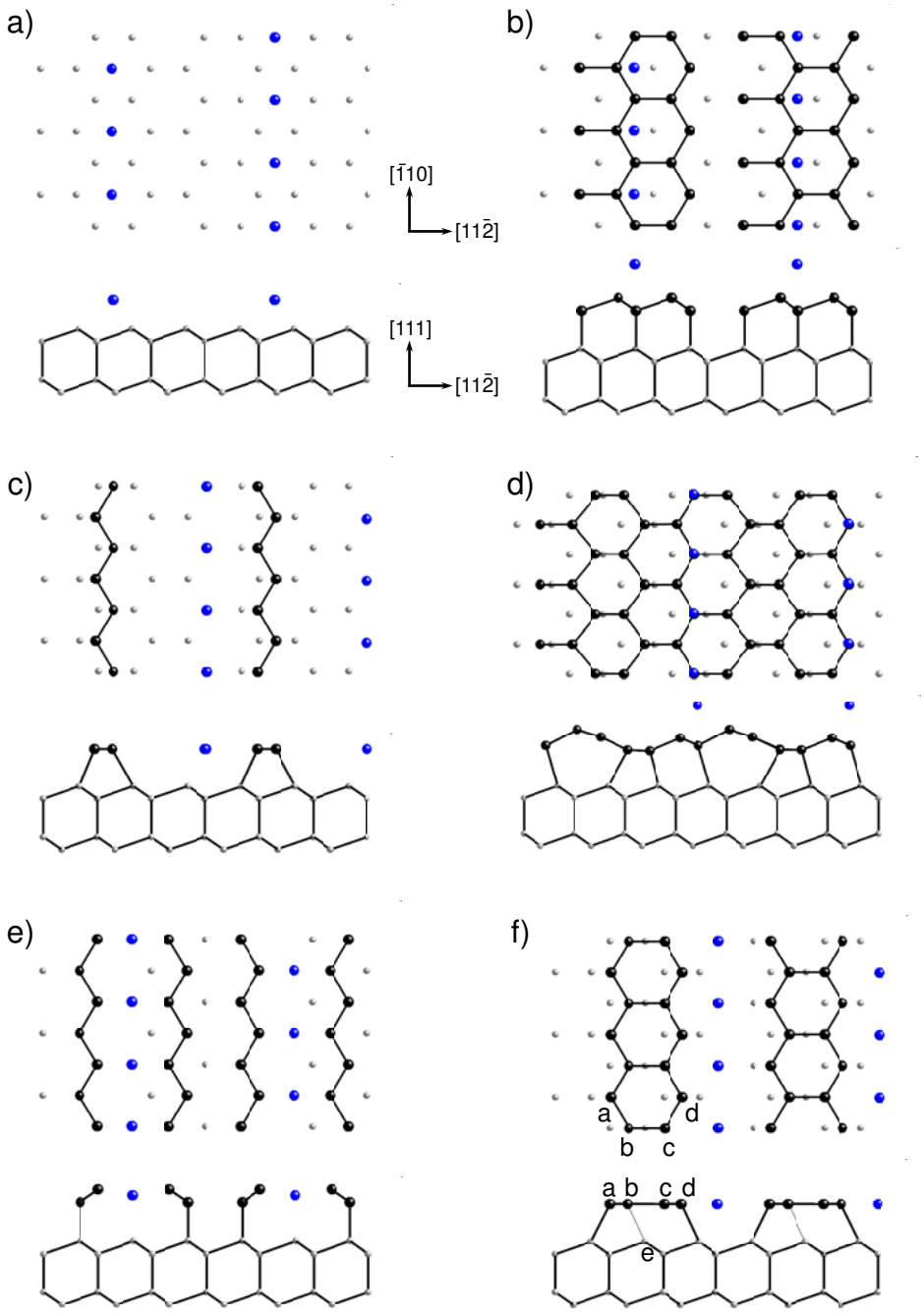

Figure 4.2: Structural models for the alkali metal induced (3×1) reconstruction: a) ordered overlayer model (666666), b) missing row model (660660), c) Seiwatz chain model (500500), d) extended Pandey model (567567), e) DπC model, f) honeycomb chain-channel model (560560).

coverage a (3×"2"), (5×"2"), (7×"2"), (9×"2"), (2×1) phase is found. The apostrophes indicate the presence of half-order streaks observed by LEED [258,261–268] and RHEED [269, 270]. The associated period doubling may also be observed in STM images [233, 261, 269, 271, 272]. For Ca and Eu even a (5×"4") symmetry has been observed [268].
The lowest coverage structure with (3×"2") periodicity has the structure of the HCC model. Saranin *et al.* [233,262] determined the Si atom density to be 4/3 ML. Medium-energy ion scattering (MEIS) experiments performed by Lee *et al.* [272], a high resolution version of Rutherford backscattering spectroscopy, revealed that the adsorbate coverage is 1/6 ML, i.e. only half the alkali metal coverage. They concluded that only every second site within the HCC channels is occupied as shown in Fig. 4.3a). The same conclusion was found independently in Ref. [263] for the Ba system and in Ref. [264,265,273] for the Ca system. It is important to note that the number of electrons donated by the divalent AEMs per (3×1) unit cell is the same as for the monovalent alkali metals. This may imply that the Si(111) surface tends to reconstruct into the (3×1) surface with the HCC structure provided that the correct amount of electrons is supplied. The deformation of the honeycomb chain and the period doubling in case of the AEM adsorbates can be regarded as a minor perturbation from the basic (3×1) HCC structure. A coverage of 1/6 ML explains well the ×2 period seen in STM images. Random registry shifts between neighboring AEM chains, i.e. a mixture of zig-zag type (3×2) and ladder type c(6×2) configurations, result in the "×2" streaks observed by LEED [262, 264, 274, 275]. STM [233, 260, 261, 269, 270, 272, 273, 275–278], ARPES [263, 264, 266, 273, 279], core-level photoemission spectroscopy [242, 265, 267, 280, 281], IV-LEED [282] and DFT calculations [269, 274, 276, 282, 283] support this generalized HCC model.
At a coverage of 1/2 ML, a (2×1) phase is found. In the case of Ba, a (2×8) pattern is found instead of the (2×1) structure, but with similar short range atomic structure [280]. Baski *et al.* [269] and independently Sekiguchi *et al.* [270] proposed a Seiwatz chain model (505050) with (2×1) periodicity for this reconstruction (see Fig. 4.3b)), which has been confirmed by LDA total energy calculations [283, 284]. The derived bandstructure and simulated STM images agree well with experimental ARPES [264, 266, 279] and STM [257, 260, 269, 270, 278] results. Results from core-level photoemission spectroscopy [265, 280, 281] are also consistent.

In the intermediate coverage regime, AEM deposition induces (5×"2") [257, 258, 265, 267, 269, 278, 280], (7×"2") [257, 258, 265, 267, 269, 278] and even (9×"2") [257, 265, 278] reconstructions, which are believed to be a simple combination of the honeycomb and Seiwatz chains [269, 270]. The structure for the (5×"2") periodicity is shown in Fig. 4.3c). STM [257, 260, 269, 270, 278, 285], ARPES [266, 268] and core-level photoelectron spectrocopy data [265, 267, 280, 281] are in support of a combined honeycomb and Seiwatz chain model. The precise coverage remains controversial for these intermediate phases. Baski *et al.* [269] and Sekiguchi *et al.* [270] initially suggested a coverage of 2/5 ML for the (5×"2") phase in agreement with the measurement by Kuzmin *et al.* [267]. Sakamoto *et al.* [265, 268] favored a coverage of

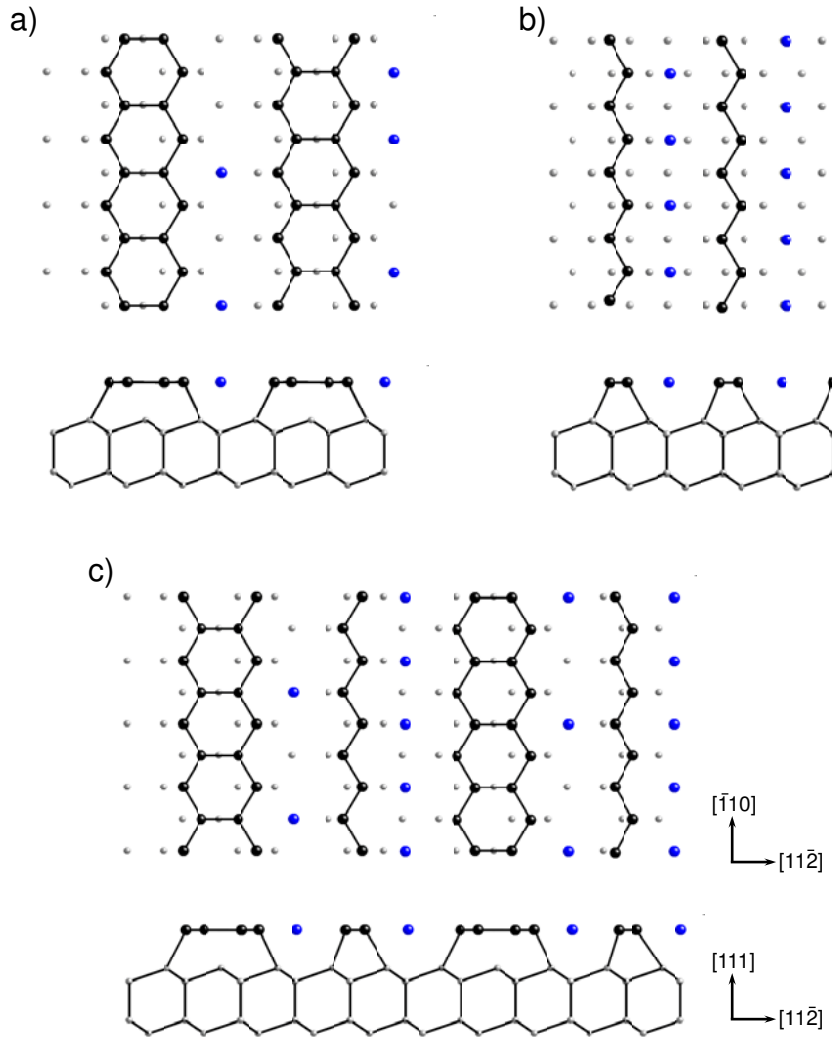

Figure 4.3: Proposed models for the alkaline earth metal induced reconstructions: a) (3×"2") honeycomb chain-channel model with every second site in the channel occupied, b) (2×1) Seiwatz chain model with every site in the channel occupied, c) (5×"2") combined honeycomb chain plus Seiwatz chain model for the intermediate coverage phase.

3/10 ML. Sekiguchi [270] further proposed a model for the (7×"2") phase with a coverage of 3/7 ML, whereas Kuzmin suggests 9/20 ML [267].

4.4 Rare earth metal induced chains

In 2002, Kirakosian *et al.* [286, 287] published their results on the newly discovered Gd chains with yet unknown atomic structure obtained with a Gd coverage of 1/5 to 2/5 ML. Since Gd diffuses into the bulk above 600^o C and segregates back to

the surface during cooling, the exact amount of Gd is difficult to determine. The LEED pattern indicates a (5×"2") periodicity. Nd [288], Dy [289], Ho [290,291] and Er [98] were also reported to stabilize (5×"2") reconstructions. The surface state dispersion of Gd chains was determined by Okuda *et al.* [292] via ARPES. They noted the strong similarity of the surface state bandstructure of the (5×"2") reconstructions induced by Ba and Gd and speculated that both surfaces share similar building blocks. However a very weak surface state near the Fermi level rendering the Gd chains metallic was also identified, distinguishing the Gd chains from the alkaline earth metal induced (5×"2") reconstructions. Furthermore Gd does not show any of the other periodicities observed for the Ba system.
This literature overview raises several questions. First of all what is the atomic structure of the Gd chains? What is the nature of the metallic state observed in ARPES for Gd chains? How does the valence state of the adsorbate influence the reconstruction, structurally as well as electronically? Why Nd, Gd, Dy, Ho and Er induce a chain reconstruction with (5×"2") periodicity whereas Sm, Eu and Yb induce the coverage dependent series with (3×"2"), (5×"2"), (7×"2"), (2×1) periodicity.
The first question is answered in section 4.5. There we show that the (5×"2) reconstruction induced by Gd is build from silicon honeycomb and Seiwatz chains. In order to confirm our structural model we inspected our STM images which are fully consistent. Also the two types of configurations of the Gd chains, a zig-zag-type arrangement and a ladder-type arrangement already noted by Kirakosian *et al.* [286] are easily explained within our model. Additional support for our model was obtained via a comparison of LEED intensities from the trivalent Gd induced (5×"2") reconstruction and the divalent Ca induced (5×"2") reconstruction. As expected the two sets of intensities are very similar and the corresponding R-factor is sufficient to assert the existence of a common structural building block. Structures build from honeycomb and Seiwatz chains are semiconducting in contrast to the metallic state reported by Okuda *et al.* [292]. However, in our STS measurements on Gd chains (unpublished), we observe semiconducting behavior. We interpret the weak photoelectron spectral weight at the Fermi level to be due to remaining patches of Si(111)-(7×7) [264] or metallic Gd silicide islands.
In order to answer the third and forth question, we examined the possible valence states of the adsorbate atoms. Commonly rare earth metals occur in a 3+ valence state but because of the greater stability of the empty, half-filled or completely filled 4f shell, it occasionally happens that the ions of Sm, Eu, Tm and Yb exist in a 2+ state [293]. Ce, Pr, Nd, Tb and Dy have also been observed in a tetravalent state [294]. But only the tetravalent state of Ce is easily accessible [295]. In compounds, La, Ce, Pr, Nd, Pm, Tb, Gd, Dy, Ho and Er are very difficult to stabilize in the divalent state [296–298]. Ref. [299] reports anomalous electron spin resonance measurements of Gd, which are explained with a divalent configuration of the Gd ion. However, for Gd to be in a 2+ state the environment must be quite radical so that we may safely assume a trivalent state for Gd embedded in the silicon sur-

face reconstruction [300]. Using core-level photoelectron spectroscopy, Kuzmin *et al.* [267] and Sakamoto *et al.* [281] found that the valence state of Eu ions is 2+ in all observed atomic chain phases. Also Yb [258, 301] was found to be in a divalent state, whereas the Sm valence [258] increases with increasing coverage. From our own experience we know how difficult it is to obtain surfaces without coexisting patches of Si(111)-(7×7) or silicide islands. We interpret the valence change at higher coverage as being due to the beginning of $(\sqrt{3} \times \sqrt{3})$ Sm silicide island formation [302] typical for trivalent adsorbates [303]. So we may assume that Sm, Eu and Yb atoms involved in atomic chain surface reconstructions are divalent, whereas Nd, Gd, Dy, Ho and Er are trivalent. In summary divalent adsorbates, rare earth but also the alkaline earth metals, induce the coverage dependent series, whereas trivalent adsorbates only stabilize the (5×"2") reconstruction.

This systematics may be understood within the framework of a simple electron counting model presented in detail in section 4.6. There we reexamine the available information on the honeycomb chains. There are two ways to stabilize honeycomb chains, either by 1/3 ML of alkali i.e. monovalent metals, or by 1/6 ML of alkaline earth or rare earth i.e. divalent metals. The number of electrons available per (3×1) unit is however always one. A similar analysis can be carried out for the (2×1) Seiwatz chains. This periodicity has been exclusively reported for divalent adsorbates occuring at a coverage of 1/2 ML. Thus there is one divalent adsorbate per (2×1) unit cell implying that a Seiwatz chain requires two electrons per (2×1) unit to be stabilized. One adsorbate per (2×1) completely fills the channel between the Seiwatz chains, no other empty site is available. This explains why Seiwatz chains are only observed for the divalent adsorbates. Within this electron counting model, we are now also able to determine the required number of electrons for the (5×"2") and (7×"2") reconstructions induced by divalent atoms. To stabilize the (5×"2") reconstruction, whose unit cell can be divided into two (3×1) honeycomb unit cell plus two (2×1) Seiwatz chain unit cell, we need a total of 6 electrons. Thus three divalent adsorbates are required, resulting in a coverage of 3/10 ML in agreement with the coverage determined experimentally by Sakamoto *et al.* [265, 268]. It is straightforward to extent these results to the (5×"2") reconstructions observed for the trivalent adsorbates. In order to supply 6 electrons per (5×"2") unit cell we need only two adsorbates resulting in a coverage of 1/5 ML. This value is consistent with the value given by Wood [288] for the Nd chains and the interval estimated by Kirakosian *et al.* [286] for the Gd chains. Furthermore we are now also able to explain why only the (5×"2") reconstruction is observed for trivalent adsorbates, since it is the only reconstruction, where the number of electrons required per unit cell is a multiple of 3. However, one could also imagine a honeycomb chain model, in which every third site of the channel is occupied by a trivalent adsorbate. However such a configuration is not observed in experiment.

In section 4.7 we put our results on a more solid theoretical footing testing the stability of the various chain configurations within density functional theory. Results in the three following sections are published in Ref. [304], [305] and [306].

4.5 Stabilization of silicon honeycomb chains by trivalent adsorbates

C. Battaglia,[1] H. Cercellier,[1] C. Monney,[1] M. G. Garnier,[1] P. Aebi,[1]

[1] *Institut de Physique, Université de Neuchâtel, 2000 Neuchâtel, Switzerland*

Published in Europhysics Letters, **77**, 36003 (2007)

The atomic structure of self-assembled quasi-one-dimensional Gd chains on Si(111) has been investigated by low-energy electron diffraction and scanning tunneling microscopy. Based on comparison between Gd and Ca chains we show that this Gd induced surface reconstruction belongs to the class of honeycomb chain-channel structures. This clearly demonstrates that, besides monovalent and divalent adsorbates, also trivalent adsorbates such as Gd stabilize silicon honeycomb chains. Consequently silicon honeycomb chains emerge as an universal building block in adsorbate induced silicon surface reconstructions.

4.5.1 Introduction

Self-assembled atomic chains on silicon surfaces have been the focus of intense research because of their quasi-one-dimensional (1D) electronic properties and their interesting physics. Recently the fluctuation and condensation phenomena at the metal insulator phase transition of the In/Si(111) system could directly be visualized via scanning tunneling microscopy (STM) [307–310]. Competing periodicities in fractionally filled bands lead to the coexistence of different Peierls distortions for the gold induced reconstructions [161, 169, 178].

Another important class of 1D systems are the alkali metal (AM=Li, Na, K, Rb, Cs) and Ag induced, insulating (3×1) reconstructions formed by the deposition of 1/3 monolayer (ML) onto the Si(111) surface. The AM/Si(111) systems adopt the so-called honeycomb chain-channel (HCC) structure [227, 234, 235] shown in Fig. 4.4a) which is stabilized by the transfer of one electron from the monovalent AM adsorbate into the Si surface states.

A very similar reconstruction with (3×"2") periodicity is formed by adsorption of alkaline-earth metals (AEM=Mg, Ca, Sr, Ba), where the ×"2" notation stands for a ×2 periodicity along the adsorbate chains but missing coherence between adjacent chains [265]. Due to the divalency of the adsorbate only 1/6 ML, i.e. half the AM coverage, is required to stabilize the HCC structure [272]. At 1/2 ML divalent adsorbates induce a (2×1) phase which was proposed to be formed of π-bonded Seiwatz chains shown in Fig. 4.4b) [269, 270]. For intermediate coverages, a series

of 1D (n×"2") reconstructions, with n taking the values 5, 7 and even 9 depending on the adsorbate, is formed which are considered to be composed of an appropriate combination of honeycomb chains and Seiwatz chains (see Fig. 4.6 for the 5×"2" case). Similar series of reconstructions were also observed for the divalent rare earth metals (REM) Sm, Eu and Yb [279]. These REMs more commonly occur in the 3+ valence state, but depending on their chemical surrounding the 2+ configuration is occasionally preferred as in this case. Thus up to now, only monovalent and divalent adsorbates were found to stabilize Si reconstructions containing the honeycomb chain building block.
In this letter we focus on trivalent REMs, which exhibit chain structures with (5×"2") periodicity *only*, but whose detailed atomic structure has not been investigated. Combining low-energy electron diffraction (LEED), STM and recent angle-resolved photoemission spectroscopy (ARPES) results [292], we show for the first time that the structure induced by trivalent adsorbates contains the same honeycomb and Seiwatz chains as in the chain reconstructions induced by divalent adsorbates. The use of multiple complementary surface analysis techniques is mandatory in the present case in order to derive a reliable structural model. Based on electron counting we are also able to explain, why only the (5×"2") periodicity is stabilized for trivalent adsorbates.

4.5.2 Experiment

We choose to investigate the Gd system, since it has recently been demonstrated that predominantly single domain atomic Gd chains can be grown on stepped Si(111) having a slight misscut of 1.1^o towards the $[\bar{1}\bar{1}2]$ direction [286] allowing the use of macroscopic diffraction methods without domain averaging. Qualitatively similar results are expected for the observed (5×"2") reconstruction induced by other trivalent rare-earth metals Dy [289], Er [98] and Ho [290]. Gd was evaporated from a water cooled e-beam evaporator with of flux of 0.5×10^{-4} ML/s at a pressure below 5×10^{-10} mbar onto the clean Si(111)-(7×7) substrate held at 680 ^{o}C. The substrate was heated by passing a direct current along the step direction $[1\bar{1}0]$. Growth and experiments were carried out in an ultra high vacuum chamber with a residual gas pressure of 3×10^{-11} mbar equipped with an Omicron LT-STM and Omicron Spectaleed LEED/Auger optics. For STM measurements we used etched W tips.

4.5.3 Results and Discussion

Figure 4.5a) shows the LEED pattern of a typical Si(111)-(5×"2")-Gd surface with one dominant domain and insignificant contributions from the two others and the Si(111)-(7×7) reconstruction. Only the (5×1) spots sketched in Fig. 4.5b) are clearly visible. The ×2 periodicity along the chains manifests itself through faint half-order streaks parallel to the ×5 spots (not shown) observed only at certain energies. Similar streaks were reported in studies of divalent adsorbate systems and

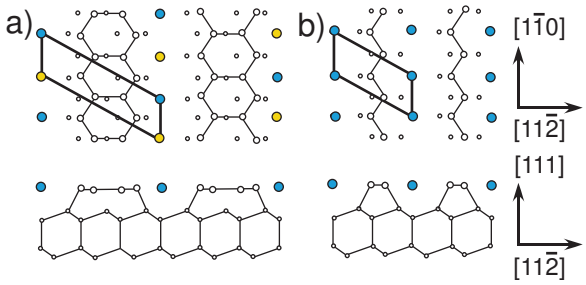

Figure 4.4: (Color online) a) Honeycomb chain and b) Seiwatz chain model with adsorbates lying in the channels between the chains. To stabilize the honeycomb chains, monovalent atoms are required to occupy every site in the channels (blue and yellow circles), whereas divalent adsorbates only occupy every second site (blue circles only). Seiwatz chains are stabilized by divalent adsorbates. Open circles are Si atoms. The (3×1) and (2×1) unit cells are also shown.

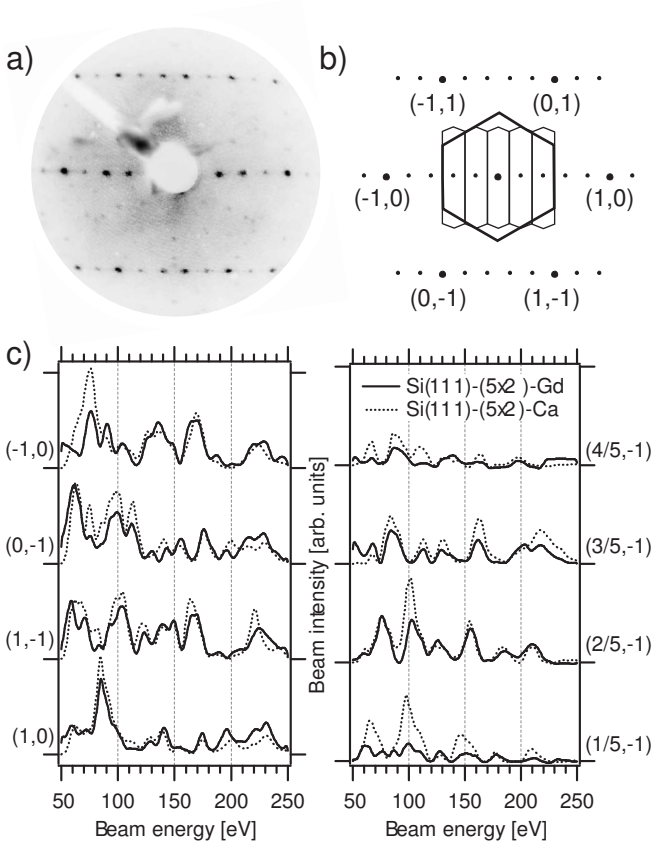

Figure 4.5: a) LEED pattern of Si(111)-(5×"2")-Gd at 48 eV. b) Sketch of the 5×1 LEED pattern in reciprocal space with beam indices. In real space the chains are running along the vertical axis. c) Comparison between experimental LEED IV curves of Si(111)-(5×"2")-Gd (full lines) and Si(111)-(5×"2")-Ca (dotted lines).

explained in terms of a stochastic distribution of adjacent chains with random registry shifts leading to a (5×"2") spot pattern with its characteristic weak half-order streaks [264, 265, 267].
Whereas the LEED spot positions only determine the type of Bravais lattice of the surface structure, i.e. its translational symmetry properties, the point symmetries can be determined by a symmetry analysis of the intensity vs voltage (IV) curves. The threefold symmetry of the unreconstructed Si(111) surface termination is broken by the growth of the chains. Whereas the (0,-1) and (-1,1) beams are still equivalent as for the substrate, the (1,0) beam exhibits a distinctive spectral signature as can be seen from Fig. 4.5c). Thus only a mirror plane perpendicular to the chains is retained.
To obtain information about the atomic positions we compare LEED IV curves from Si(111)-(5×"2")-Gd to the curves from Si(111)-(5×"2")-Ca in Fig. 4.5c). IV-LEED fingerprinting has played a crucial role in establishing the equivalence between different AM induced (3×1) HCC reconstructions, since it was recognized that the Si(111)-(3×1)-AM reconstruction is predominantly a substrate reconstruction with a common structure independent of the adsorbate species [204]. Visual inspection of Fig. 4.5c) already shows that the agreement between the Gd induced and the Ca induced reconstruction containing one honeycomb chain and one Seiwatz chain is surprisingly good. Most peak positions of the Gd chains fall on the same energies as for the Ca chains with comparable relative intensities. To obtain a quantitative measure for the agreement between the two structures we calculated Pendry's R factor R_p [77], which takes into account the peak positions but also the relative intensities between the peaks. For the integral order spots we obtain $R_p = 0.29$. For the fractional order beams we obtain $R_p = 0.35$. These values are similar to $R_p = 0.36$ obtained by Lottermoser [227] comparing theoretical curves to experimental data for the HCC model. The good agreement between the two experiments suggests that both structures share the same structural building blocks. Deviations may be due to the difference in atomic number and the associated scattering characteristics between Gd and Ca, differences in the precise adsorption geometry and coverage.
Adsorbate coverage is an important parameter for the determination of any structural model. The exact amount of Gd at the surface is difficult to determine accurately due to the fact that Gd diffuses into the bulk above 600 ^{o}C [286]. The ideal adsorbate coverage can however be determined when considering the electron count required to stabilize the honeycomb and Seiwatz chains. The HCC structure is known to be stabilized by the donation of one electron per (3×1) unit cell [235, 272]. Similarly the Seiwatz chain requires two electrons per (2×1) cell, since it may be stabilized by 1/2 ML of divalent adsorbates. This is consistent with the number of surface states observed in ARPES [281]. The (5×2) unit cell can be thought of as being build from two (3×1) and two (2×1) cells, thus requires six electrons to be stabilized. Since Gd is trivalent, the ideal coverage is two Gd atoms per (5×2) cell or 1/5 ML. This is in agreement with the estimate of 0.2-0.4 ML given in Ref. [286]. The proposed model for the Si(111)-(5×"2")-Gd surface is shown in Fig. 4.6 consist-

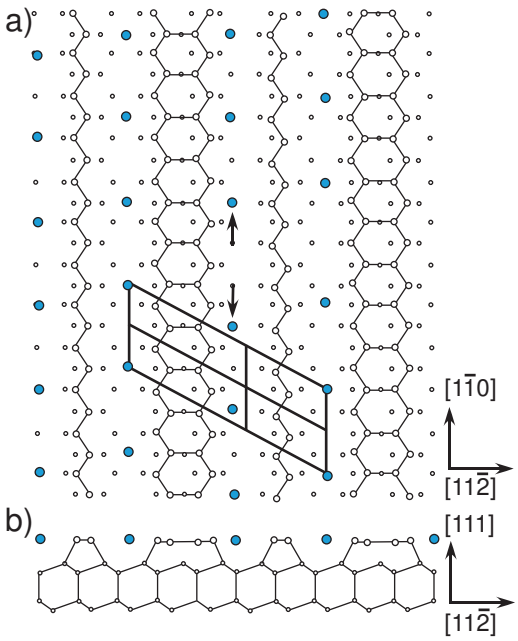

Figure 4.6: (Color online) Structural model for the Si(111)-(5×"2")-Gd surface. Open circles are Si atoms, filled blue circles are Gd atoms. The (5×2) unit cell divided into two (3×1) and two (2×1) unit cells is also shown. Arrows indicate a registry shift of the adsorbates in the channel.

ing of alternating hexagonal honeycomb chains and zig-zag Seiwatz chains made of Si. The adsorbates are expected to form chains in the channels in between. Due to the weak sensitivity of IV-LEED to the adsorbate itself, we can not decide which absorption site is favored. Any structural model must be consistent with results from other experimental techniques. Fig. 4.7 presents STM images of the Gd chains. The overview a) shows long, parallel chains running along the [1$\bar{1}$0] direction. The separation between the rows is consistent with the ×5 periodicity observed in LEED patterns. High magnification empty and filled state images acquired in the same scan to preserve their mutual registry are shown in Fig. 4.7b) and c) respectively. The structural model is superimposed. Based on simulated STM images derived from local density approximation (LDA) calculations for the HCC structure [235, 272], we identify the dark rows in the empty state image with the location of the honeycomb chains. High intensity in the empty state image is found along the adsorbate channels for both the honeycomb and the Seiwatz chain structure [272, 284]. This is easily understood by noticing that the empty orbitals are necessarily located on the adsorbate atom, since it donates its electrons to the silicon chains. The filled state image c) appear as triple rows of protrusions with ×2 periodicity along the rows. The third row located along the Seiwatz chain (marked by S in Fig. 4.7c) appears to lie slightly lower than the two main rows (marked by H in Fig. 4.7c), which we identify with the honeycomb chains. In a previous STM study only the

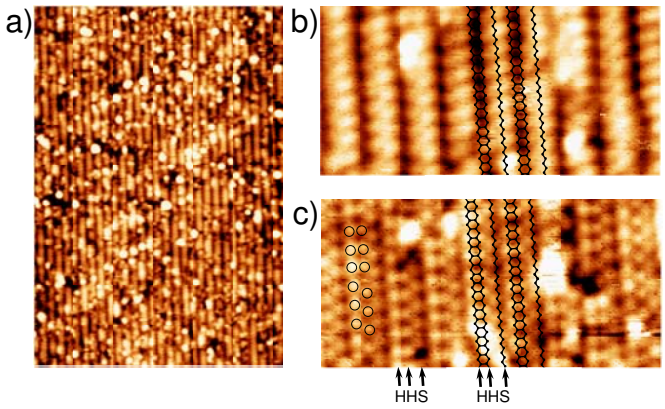

Figure 4.7: (Color online) a) STM topography overview (U= 1.9 V), 60 nm × 90 nm, b) and c) high resolution topography of empty (U=1.9 V) and filled states (U=-1.9V), 18 nm × 9 nm, I=0.18 nA. Arrows indicate the location of the honeycomb chain (H) and Seiwatz chain (S). Empty circles mark the two possible configurations of the honeycomb chain caused by a registry shift of the Gd atoms in the adjacent channel as indicated by arrows in Fig. 4.6.

two main rows H were resolved [286]. The pairing of protrusions causing the ×2 periodicity along the chains has been found to be rather electronic in origin than geometric [275]. The electrostatic attraction between a positive adsorbate ion and the electrons in the neighboring saturated dangling bonds give rise to such paired protrusions. We also remark that the registry of neighboring chains is correct in our model. Careful inspection of the filled state STM image shows that the honeycomb chain comes in two configurations, either as two parallel rows of protrusions or in a zig-zag configuration, indicated by empty circles in Fig. 4.7c). Such a registry shift of only one period between the two rows of the honeycomb chain is illustrated by the arrows in Fig. 4.6 and is simply due to a missing adsorbate and a consecutive shift of all the following adsorbates by one period along the chain direction. The local mixing of these two arrangements with poor long range order is responsible for the ×2 streaks seen in LEED patterns [264]. Furthermore this kind of defect leads to a local charge imbalance. It has been suggested that additional Si adatoms are able to supply electrons that dope the parent chain structure [311] and may be able to compensate for such missing charge. Additional Si atoms are necessarily present since the formation of the HCC structure and consequently also of the (5×"2") structure is accompanied by significant Si mass transport at the surface [231] due to the fact that the Si atom surface density of the (5×"2") structure is not equal to that of Si(111)-(7×7). Although steps may serve as a reservoir for reintegrating ejected Si atoms into the surface, electromigration due to dc current heating parallel to the steps does not favor the Si atoms to wander towards the steps, resulting in a large number of randomly distributed protrusions on top of the chains.

We now turn to the discussion of recent ARPES results from Si(111)-(5×"2")-

Gd [292], which provide additional confirmation for our structural model. At least three semiconducting surface states are observed at binding energies between 1 and 2 eV, whose dispersions, band widths and symmetry properties are very similar to those of the AM and AEM induced (3×1) and (3×"2") reconstructions [263] supporting a honeycomb chain based structure. Furthermore ARPES data for the AEM induced (5×"2") structure resembles the one from the (3×"2") reconstruction. Very weak intensity is observed at the Fermi energy, but has been interpreted as being due to defect states. A small contribution to the spectral weight at the Fermi energy was also observed in the semiconducting Si(111)-(3×"2")-Ca system [264], but was attributed to remaining (7×7) regions of pure silicon. Additionally, prolonged annealing of the Gd induced reconstruction at 680 ^{o}C leads to the nucleation of metallic Gd silicide islands at the expense of the chain reconstruction, which might possibly be responsible for the observed photoelectron signal at the Fermi energy. However, from STM measurements we do not find evidence for a metallic surface state localized on the chains. We conclude that the Gd induced structure is semiconducting and consequently requires an even number of valence electrons per unit cell in agreement with the coverage of two Gd atoms per (5×2) unit cell. Therefore all ARPES results fully support our structural model.

A peculiar experimental finding to be explained is that Gd and other trivalent REMs stabilize chain structures with the (5×"2") symmetry exclusively, whereas the monovalent adsorbates stabilize only the genuine (3× 1) HCC structure and the divalent adsorbates induce a series of (n×"2") reconstructions. Monovalent adsorbates must occupy every site along the channel between the honeycomb chains to satisfy the doping criterion. For lower coverages only parts of the Si(111)-(7×7) are transformed, whereas higher coverages induce different surface structures. The stabilization of Seiwatz chains requiring two electrons per unit cell is not possible. Divalent adsorbates in turn must occupy every second site to satisfy the doping balance. For higher coverages however, additional adsorbates may be incorporated in the channels at the expense of reducing every second honeycomb chain into a Seiwatz chain. For trivalent adsorbates, charge balance requires that every third site in the channel is occupied, if one wants to build a structure exclusively formed by honeycomb chains. This is apparently energetically unfavorable compared to an occupation of every second site, which requires the combination of a honeycomb chain with a Seiwatz chain resulting in the (5×"2") symmetry. The stabilization of a (5×"2") period requires a total of six electrons, a condition easily satisfied by taking two trivalent adsorbates per unit cell. (7×"2") and (9×"2") reconstructions are not observed for the trivalent adsorbates. Consisting of one honeycomb chain and two respectively three Seiwatz chains, they require 10 respectively 14 electrons per unit to be stabilized, a condition which can not be satisfied by trivalent donors. Electron counting thus provides a simple intuitive picture for the occurrence of the various phases.

4.5.4 Conclusion

Driven by the elimination of dangling bonds and relief of surface stress, silicon surfaces reconstruct in strikingly diverse ways. Among the large variety of adsorbate induced reconstructions, the honeycomb chain emerges as a most stable building block allowing maximum reduction of the surface energy. The fact that only silicon atoms participate in the formation of the honeycomb chains allows a variety of adsorbates to adopt the HCC structure by donating the correct number of electrons to the substrate. Combining the complementary strength of IV-LEED fingerprinting, STM and ARPES, we demonstrated for the first time that next to monovalent and divalent adsorbates, *trivalent adsorbates are also able to stabilize the honeycomb chains*. Based on a intuitive electron counting model, we are further able to explain, why only the (5×"2") symmetry is stabilized by trivalent adsorbates. Our conclusions allow to enlarge the range of honeycomb chain stabilizing adsorbates to the trivalent elements.

Helpful conversations with Celia Rogero, Laurent Despont, Christian Koitzsch and José A. Martin-Gago are gratefully acknowledged. Skillfull technical assistance was provided by our workshop and electric engineering team. This work was supported by the Fonds National Suisse pour la Recherche Scientifique.

4.6 Unveiling new systematics in the self-assembly of atomic chains on Si(111)

C. Battaglia,[1] H. Cercellier,[1] C. Monney,[1] L. Despont,[1] M. G. Garnier,[1] P. Aebi,[1]

[1] *Institut de Physique, Université de Neuchâtel, 2000 Neuchâtel, Switzerland*

Published in J. Phys.: Conf. Ser. 100, 052078 (2008)
Proceedings of the 17th International Vacuum Congress (IVC-17),
13th International Conference on Surface Science (ICSS-13) and
International Conference on Nanoscience and Technology (ICN+T 2007)
2−6 July 2007, Stockholm, Sweden

Self-assembled arrays of atomic chains on Si(111) represent a fascinating family of nanostructures with quasi one-dimensional electronic properties. These surface reconstructions are stabilized by a variety of adsorbates ranging from alkali and alkaline earth metals to noble and rare earth metals. Combining the complementary strength of dynamical low-energy electron diffraction, scanning tunneling microscopy and angle-resolved photoemission spectroscopy, we recently showed that besides monovalent and divalent adsorbates, trivalent adsorbates are also able to stabilize silicon honeycomb chains. Consequently silicon honeycomb chains emerge as a most stable, universal building block shared by many atomic chain structures. We here present the systematics behind the self-assembly mechanism of these chain systems and relate the valence state of the adsorbate to the accessible symmetries of the chains.

4.6.1 Introduction

Stimulated by their huge potential for next generation electronic, magnetic, optical and chemical devices, research on ordered nanostructures has attracted tremendous interest. Their fabrication remains a challenging task. Spontaneous self-assembly represents a promising bottom-up approach, which allows to fabricate nanostructures in a massively parallel fashion. Understanding the mechanisms underlying spontaneous nanostructure formation is crucial for establishing control over their dimensions, spatial distribution and uniformity.

Here we address the self-assembly of macroscopic arrays of atomic chains on silicon surfaces which have been the focus of intense research because of their fascinating quasi one-dimensional electronic properties [161, 169, 178, 309]. A large variety of adsorbates ranging from alkali and alkaline earth metals to noble and rare earth metals is known to induce a reconstruction of the Si(111) surface into atomic chains. Most chain structures are based on a common structural backbone formed by silicon

atoms. The role of the adsorbate is to stabilize these silicon chains by donating the correct number of electrons. We recently showed that besides monovalent and divalent adsorbates, trivalent adsorbates are also able to stabilize Si atomic chains [304]. In this paper we first review the structure for the monovalent and divalent adsorbates and then introduce the extension to the trivalent adsorbates. This new piece of information allows us to understand new aspects of the systematics behind the self-assembly process, from which we can draw conclusions about the accessible symmetries of the chains.

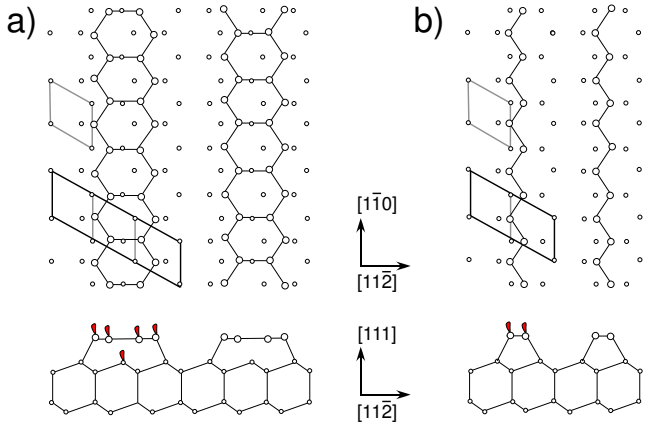

Figure 4.8: Top (upper part) and side (bottom part) view of the two prototypical silicon chains separated by the channels which accommodate the adsorbate atoms (not drawn): a) honeycomb chain with (3×1) unit cell and b) Seiwatz chain with (2×1) unit cell. The (1×1) unit cell of the (111) oriented substrate is shown in grey. The dangling bonds of under-coordinated silicon atoms are schematically indicated in the side view by the red symbols. The crystallographic directions of the substrate are also drawn.

4.6.2 Monovalent adsorbates

Monovalent adsorbates such as alkali metals (Li, Na, K, Rb, Cs) together with Ag are known to induce a chain reconstruction on Si(111) exhibiting a (3×1) superstructure. The widely accepted structural model, the so-called honeycomb chain-channel (HCC) model [227,234,235], is shown in Fig. 4.8a). The (3×1) unit cell (black) and its relation to the (1×1) surface unit cell (grey) of the (111) oriented substrate is shown as well. The HCC model consists of Si honeycomb chains running along the [1$\bar{1}$0] direction separated by empty channels. The structure contains five threefold coordinated, thus under-coordinated, silicon atoms per (3×1) unit cell. Each of the five associated silicon dangling bonds, marked schematically by the red symbols in Fig. 4.8a), gives rise to a surface state. A total of five electrons, one from each dangling bond, is available to fill these states. Since each surface state is able to accommodate a maximum of exactly two electrons, we get two completely filled surface states below the Fermi energy, one half-filled metallic surface state crossing

the Fermi energy and two empty states. However, in order to stabilize the HCC structure one more electron is required. This additional electron, which is provided by the adsorbate atom, allows an enormous energy gain by completely filling the metallic state, rendering it insulating by bringing it below the Fermi energy [235]. The adsorbate atoms, represented by blue disks in Fig. 2a), are occupying the sites inside the channels. Since one electron per (3×1) unit cell is required, there is one monovalent adsorbate per (3×1) unit cell and thus the adsorbate coverage is 1/3 monolayer (ML).

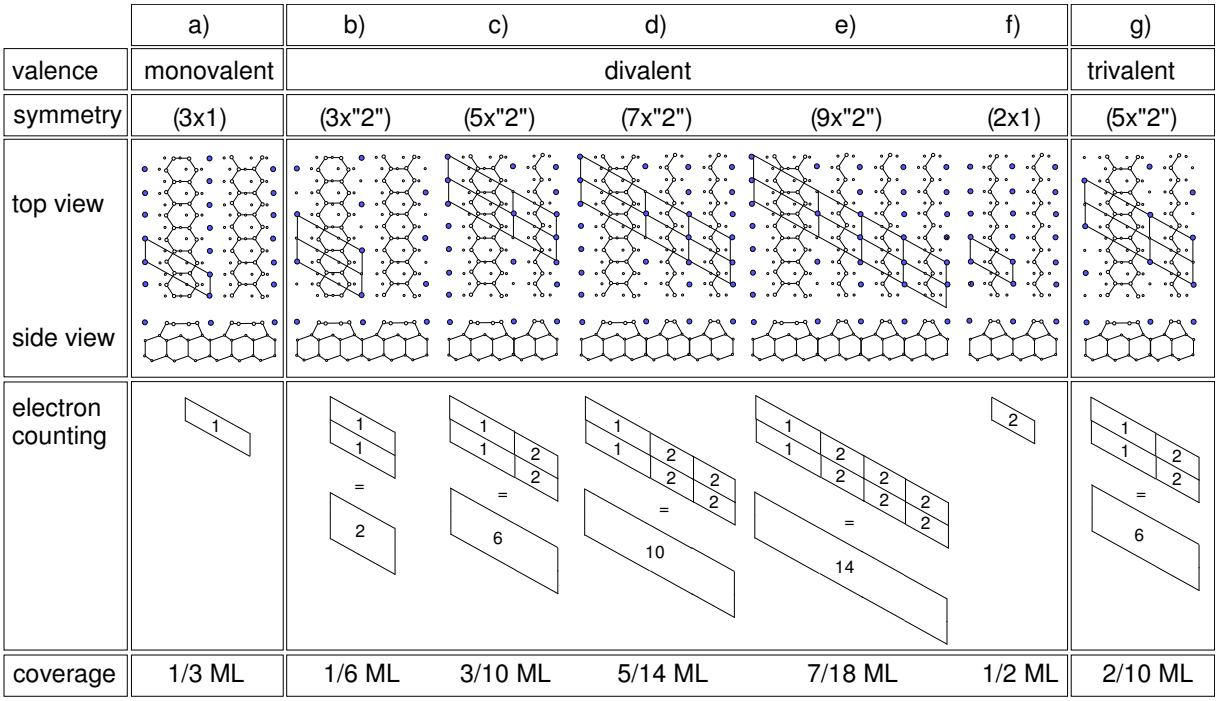

Figure 4.9: Systematics of adsorbate induced silicon chains. Adsorbate atoms are drawn in blue. Valence of the adsorbate, symmetry of the unit cell, top and side view of the atomic structure are shown. The line labeled electron counting, shows how the final unit cell can be decomposed into the basic building blocks. The number inside each unit cell gives the number of electrons required to stabilize each building block. The last line gives the adsorbate coverage for each structure.

4.6.3 Divalent adsorbates

Silicon honeycomb chains may also be stabilized by divalent adsorbates such as the alkaline earth metals (Mg, Ca, Sr, Ba) and rare earth metals (Sm, Eu, Yb) [281]. Although these rare earth metals commonly occur in a +3 valence state, a +2 configuration is occasionally preferred as in this case. Since a divalent adsorbate provides twice as many electrons compared to a monovalent adsorbate, only 1/6 ML, i.e. half the monovalent adsorbate coverage is required [272]. Consequently only every

second site in the channel is occupied leading to a doubling of the unit cell size along the chain direction (see Fig. 4.9b). Thus for divalent adsorbates the unit cell has a (3×2) symmetry. In LEED patterns however, instead of sharp ×2 spots, only faint half-order streaks parallel to the ×3 spots are observed. These are caused by the occurrence of two consecutive empty sites in the channel. Such a defect leads to a registry shift of the adsorbate sequence in one channel with respect to adsorbates in the adjacent channel by one period along the chain direction. Since adsorbates in adjacent channel are only very weakly coupled, the two configurations are energetically almost degenerate. The local mixing of these two arrangements with poor long range order is responsible for the ×2 streaks seen in LEED patterns. To indicate the presence of half-order streaks one uses the notation (3×"2") where the ×"2" stands for a ×2 periodicity with missing coherence between adjacent chains [265].
Besides the prototypical silicon honeycomb chains, divalent adsorbates induce a second type of silicon chain structure at higher coverage, the so-called Seiwatz chains [269, 270] characterized by a (2×1) unit cell as shown in Fig. 4.8b). Seiwatz chains consist of zig-zag chains of silicon atoms separated by empty channels. Seiwatz chains require two electrons per (2×1) unit cell, since they are stabilized by 1/2 ML of divalent adsorbates. Consequently every available site in the channel must be occupied by a divalent adsorbate as shown in Fig. 4.9f). Monovalent adsorbates instead are not able to stabilize Seiwatz chains, since they are not able to donate the required amount of electrons.
At intermediate coverages, divalent adsorbates stabilize chain structures with (5×"2"), (7×"2") and even (9×"2") depending on the adsorbate. These are considered to be composed of an appropriate combination of honeycomb chains and Seiwatz chains. For the (5×"2") symmetry for instance shown in Fig. 4.9c), a honeycomb chain alternates with a Seiwatz chain. The (5×"2") unit cell can be thought of as being composed of two honeycomb unit cells with (3×1) symmetry plus two Seiwatz unit cells with (2×1) symmetry as schematized in Fig. 4.9c). The adsorbates have to donate one electron for each of the two honeycomb units plus two electrons for each of the two Seiwatz units. Thus the adsorbates have to provide a total of six electrons per (5×"2") unit cell. This condition is easily satisfied by placing three divalent adsorbates per (5×"2") in between the Si chains resulting in a coverage of 3/10 ML. For the (7×"2") and the (9×"2") symmetry shown in Fig. 4.9d) and 4.9e) a honeycomb chain alternates with two respectively three successive Seiwatz chains, requiring the adsorbates to provide 10 respectively 14 electrons, resulting in an adsorbate coverage of 5/14 respectively 7/18 ML. Note that these intermediate symmetries are not accessible to monovalent adsorbates, since it requires the stabilization of Seiwatz chains.

4.6.4 Trivalent adsorbates

For trivalent adsorbates such as Gd [286], but also Dy [289], Er [98], Ho [290] chain reconstructions with (5×"2") symmetry have been observed. To construct

the (5×"2") unit cell, we combine once again a honeycomb chain with a Seiwatz chain (see Fig. 4.9g). The required six electrons are easily obtained by placing two trivalent adsorbates per unit cell in the channels. Note that for the divalent adsorbates, we had to take three adsorbates to satisfy the doping criterion. The resulting coverage for the trivalent adsorbates is 2/10 ML, a value which is consistent with experiment [286]. It is important to emphasize that besides the (5×"2") symmetry no other symmetry has been observed for the trivalent adsorbates. Our model gives an easy explanation: the (7×"2") and the (9×"2") symmetry require 10 respectively 14 electrons to be stabilized - a condition which can not be satisfied by a trivalent adsorbate. Thus electron counting provides an intuitive picture for the occurrence of the various allowed symmetries.

4.6.5 Conclusion

Self-assembly of atomic chains on silicon surfaces is driven by the elimination of dangling bonds. Most chain structures share a common building block formed by silicon atomic chains. The fact that only silicon atoms participate in the formation of the chains allows a variety of adsorbates to adopt these one-dimensional nanostructures. Using a simple electron counting model, we are able to relate the valence state of the adsorbate to the accessible symmetries of the chains.

Stimulating discussions with Christian Koitzsch and Pascal Ruffieux are gratefully acknowledged. Skillfull technical assistance was provided by our workshop and electric engineering team. This work was supported by the Fonds National Suisse pour la Recherche Scientifique through Div. II and MaNEP.

4.7 Stability and structure of atomic chains on Si(111)

C. Battaglia,[1] P. Aebi,[1] S.C. Erwin,[2]

[1] *Institut de Physique, Université de Neuchâtel, 2000 Neuchâtel, Switzerland*
[2] *Center for Computational Materials Science, Naval Research Laboratory, Washington D.C. 20375, USA*

Submitted to Phys. Rev. B

We study the stability and structure of self-assembled atomic chains on Si(111) induced by monovalent, divalent and trivalent adsorbates, using first-principles total-energy calculations and scanning tunneling microscopy. We find that only structures containing exclusively silicon honeycomb or silicon Seiwatz chains are thermodynamically stable, while mixed configurations, with both honeycomb and Seiwatz chains, may be kinetically stable. The stability and structure of these atomic chains can be understood using a surprisingly simple electron-counting rule.

4.7.1 Introduction

Understanding and controlling the structure of surfaces on the atomic level is of tremendous technological importance. This is especially true for the growth of semiconductor nanostructures, where the competition between thermodynamics and kinetics can play a decisive role. The reconstruction of semiconductor surfaces is driven by the elimination of dangling bonds and the minimization of surface stress, with a striking diversity of outcomes. Despite this variety, even very elaborate architectures are generally comprised of a small number of elementary structural building blocks. Dimers and adatoms on Si(100) and Si(111), respectively, are the best known strategies for reducing the number of dangling bonds. Tetramers and pentamers, encountered on Si(114) [121], Si(113) [125], Si(110) [127,128], and Si(331) [305] constitute more complex units. For adsorbate-induced surface reconstructions of the Si(111) surface, honeycomb [227, 234, 235] and Seiwatz chains [221] have recently emerged as universal building blocks [304] (see Fig. 4.10). These form the basis of a large class of atomic chain reconstructions which have been the focus of intense research because of their fascinating quasi one-dimensional electronic properties [161,169,178,309]. The fact that only silicon atoms participate in the formation of the honeycomb and Seiwatz chains means that a number of different adsorbates can induce a chain reconstruction, simply by donating the correct number of electrons to the substrate.

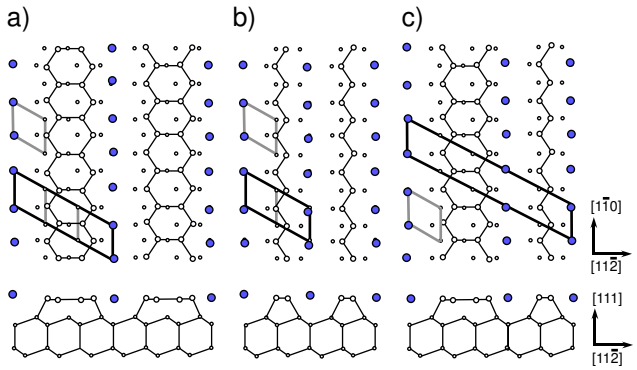

Figure 4.10: (Color online) Top (upper) and side (bottom) view of the two prototypical silicon chains separated by channels that accommodate the adsorbate atoms (filled blue circles). (a) Honeycomb chain with (3×1) unit cell. (b) Seiwatz chain with (2×1) unit cell. (c) Mixed chain structure with (5×1) unit cell. The (1×1) unit cell of the (111)-oriented substrate is indicated in grey. The crystallographic directions of the substrate are also indicated.

We have recently revealed remarkable systematics in this class of adsorbate-induced reconstructions, relating the valence state of the adsorbate to the allowed coverages and periodicities of the resulting adsorbate chains [312]. All experimentally observed phases satisfy a simple electron-counting rule: the adsorbates must provide either one electron (to stabilize a (3×1) honeycomb-chain unit), or two electrons (to stabilize a (2×1) Seiwatz-chain unit). [304] For monovalent adsorbates the only experimentally observed configuration is obtained with an adsorbate coverage of 1/3 ML.[2] This corresponds to one adsorbate donating one electron per (3×1) honeycomb chain unit as shown in Fig. 4.10(a) , in agreement with the electron-counting rule. For divalent adsorbates, only 1/6 ML (half the monovalent adsorbate coverage) is required to stabilize honeycomb chains, since a divalent adsorbate donates two electrons. The pure Seiwatz chain structure shown in Fig. 4.10(b) is stable for 1/2 ML of divalent adsorbates, resulting from two donated electrons per (2×1) Seiwatz chain unit. A mixed chain phase, alternating between honeycomb and Seiwatz chains as shown in Fig. 4.10(c), observed for divalent adsorbates, at intermediate coverage of 3/10 ML, also satisfies the electron-counting rule. Here the divalent adsorbates supply one electron to the honeycomb chain unit and two electrons to the Seiwatz chain unit. Similarly, trivalent adsorbates at a coverage of 2/10 ML donate the same number of electrons, allowing the same mixed phase to be stabilized.

In this report we subject these observed systematics, and the electron-counting rule deduced from them, to more detailed theoretical scrutiny. Specifically, we examine theoretically the thermodynamic and kinetic stability of several chain reconstructions of Si(111) using first-principles total-energy methods. We compare the resulting pictures that emerge for three prototypical adsorbates: monovalent (Na),

[2]We define 1 ML as the atom density of the bulk-terminated Si(111) surface of 7.8×10^{14} cm^{-2}.

divalent (Ca), and trivalent (Gd). For each adsorbate we compare a number of reconstructions with different adsorbate coverage, including the bare Si(111)-(7×7) reconstruction and, for Ca and Gd adsorbates, the silicide phase experimentally observed at higher coverage. For each candidate reconstruction we determine the surface energy as a function of adsorbate chemical potential, and thereby determine the energy ordering of our candidate reconstructions at any thermodynamically allowed value of chemical potential. We find that the thermodynamically stable chain reconstructions are formed exclusively from either honeycomb or Seiwatz chains, with mixed phases slightly higher in energy. We also argue that for Gd adsorbates the experimentally observed mixed phase, which combines honeycomb and Seiwatz chains, while not thermodynamically stable, is kinetically stable.

4.7.2 Methods

We used first-principles total-energy calculations to determine equilibrium geometries and relative surface energies. The calculations were performed in a slab geometry with up to six layers of Si plus the reconstructed surface layer. All atomic positions were relaxed except for the bottom layer, which was passivated. Total energies and forces were calculated within the generalized-gradient approximation to density-functional theory (DFT), using projector-augmented-wave (PAW) potentials [313,314]. We checked that the slab thickness, plane-wave cutoff, and sampling of the surface Brillouin zone were each sufficient to converge the relative surface energies to within 1 meV/Å^2.

For calculations with Gd adsorbates, the seven $4f$ electrons were treated explicitly as valence states. The possibility of magnetic order among Gd atoms within a single fully occupied channel was investigated in one case, with the result that ferromagnetic ordering was slightly preferred, by 0.1 eV, to antiferromagnetic ordering. Based on this finding we assumed ferromagnetic order for all Gd phases. We also found that putting the $4f$ electrons in the core led to only insignificant changes to the calculated absolute surface energies. This establishes that magnetic order among the Gd atoms plays no substantive role in the stability of different surface phases.

Growth and STM experiments were carried out in a ultra-high vacuum chamber with a residual gas pressure of 3×10^{-11} mbar equipped with an Omicron LT-STM. Boron-doped Si(111) with a resistivity of 5 Ω·cm was heated by passing a direct current. Gd was evaporated from a water-cooled e-beam evaporator.

We consider first the stability of atomic chains induced by monovalent adsorbates such as the alkali metals Li, Na, K, Rb, and Cs. These are known to induce a chain reconstruction on Si(111) exhibiting simple (3×1) periodicity. The widely accepted structural model, the so-called honeycomb chain-channel (HCC) model [227, 234, 235], is shown in Fig. 4.10(a). The HCC model consists of Si honeycomb chains aligned along the $[1\bar{1}0]$ direction, separated by empty channels. The adsorbate atoms occupy sites within these channels.

The presence of an adsorbate, such as Na, in the HCC model does not allow direct comparison between its surface energy and the surface energy of clean reconstructed Si(111)-(7×7). The proper way to compare energies of structures differing in stoichiometry is via the chemical potentials μ_{Si} and μ_{Na} of the constituents [315], which are the energy per atom available in the reservoirs with which the surface is assumed to be in equilibrium. The surface energy (per unit area) is then

$$\gamma = E_{\mathrm{surf}}/A = (E_{\mathrm{tot}} - n_{\mathrm{Si}}\mu_{\mathrm{Si}} - n_{\mathrm{Na}}\mu_{\mathrm{Na}})/A, \tag{4.1}$$

where E_{tot} is the total energy of a double-sided slab whose unit cell, with total area A, contains n_{Si} Si atoms and n_{Na} Na atoms. Since the surface is in equilibrium with the bulk Si substrate, μ_{Si} is the energy per atom in bulk Si. The adsorbate chemical potential, μ_{Na}, however, corresponds to a real physical variable that can be externally tuned by, for example, varying the partial pressure of Na. Intuitively, increasing the Na partial pressure will increase the stability of structures with higher Na coverage. This is evident from recasting Eq. 4.1 as

$$\gamma = \gamma_0 - \theta_{\mathrm{Na}}\mu_{\mathrm{Na}}, \tag{4.2}$$

where θ_{Na} is the adsorbate coverage. From Eq. 4.2 it is clear that reconstructions with larger θ_{Na} are increasingly favored as μ_{Na} increases. For a given value of μ_{Na} the reconstruction with the lowest surface energy γ will be realized in an experiment, if it is performed under conditions of thermodynamic equilibrium. Phase transitions can thus occur as μ_{Na} is changed.
Thermodynamics places an upper bound on the adsorbate chemical potential, $\mu_{\mathrm{Na}} \leq \mu^0_{\mathrm{Na}}$, given by the energy per atom in the ground-state (body-centered cubic) phase of elemental Na. Exceeding this limit in an experiment would result in precipitation of elemental Na, because that phase would then be energetically preferable to any adsorbed phase. When making the chemical potential sufficiently low, by turning the partial pressure to a very small value, the bare surface will be the most stable phase. The more interesting question is what happens in between these two extremes.

4.7.3 Results & Discussion

Monovalent adsorbates

The calculated DFT surface energies, as a functional of chemical potential, are shown in Fig. 4.11(a) for several reconstructions of Si(111) induced by the monovalent adsorbate Na. All surface energies are given relative to that of the bare Si(111)-(7×7), which we place at γ=0.[3] The colored lines with non-zero slopes represent the surface energies for various Na-induced reconstructions. Results for two HCC phases

[3]The surface energy for the Si(111)-(7×7) reconstruction was determined by calculating the surface energy of the Pandey model [225] for Si(111)-(2×1) and subtracting the published DFT energy difference of 60 meV per (1×1) unit cell [316].

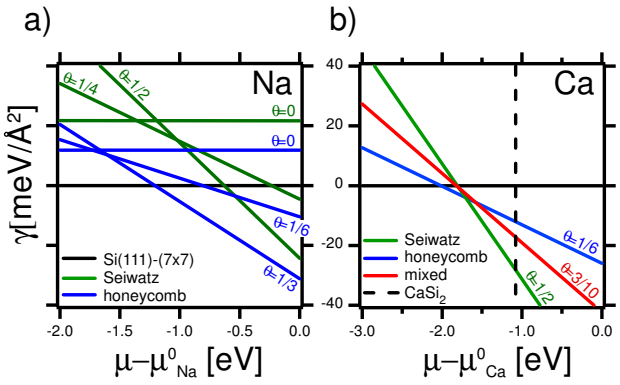

Figure 4.11: (Color online) (a) Surface-energy diagram for monovalent Na adsorbates. We compare pure honeycomb chains (θ=1/3, 1/6 and 0 ML, blue lines) and pure Seiwatz chains (θ=1/2, 1/4 and 0 ML, green lines). The surface energy of Si(111)-(7×7) (θ=0 ML, black line) is also shown. (b) Surface-energy diagram for divalent Ca adsorbates. We compare pure honeycomb chains (θ=1/6, blue line), pure Seiwatz chains (θ=1/2, green line) and a mixed chain configuration with alternating honeycomb and Seiwatz chains (θ=3/10, red line). The vertical dashed line represents the bulk $CaSi_2$ silicide.

are shown (blue lines), with θ_{Na}=1/3 and 1/6 ML corresponding to fully occupied (3×1) and half-filled (3×2) channels, respectively. Also shown are results for two Seiwatz-chain phases (green lines), with θ_{Na}=1/2 and 1/4 ML, corresponding to fully occupied (2×1) and half-filled (2×2) channels, respectively. Finally, results for "empty" HCC and Seiwatz reconstructions (i.e. without adsorbates) are shown as flat lines.

From the energy ordering of these various reconstructions, it is evident that over the allowed range of μ_{Na} only two phases are thermodynamically stable: the clean Si(111)-(7×7) surface and the (3×1) HCC phase with θ_{Na}=1/3, in agreement with experiment. We find, but do not here show, very similar results for other monovalent adsorbates (Li, K), and conclude that for monovalent adsorbates the only thermodynamically stable phase is the HCC with every site in the channel occupied.

Divalent adsorbates

We turn now to reconstructions induced by divalent adsorbates, such as the alkaline earth metals (Mg, Ca, Sr, Ba) and rare earth metals (Sm, Eu, Yb). From experiments we know that at a coverage of 1/6 ML, divalent adsorbates stabilize (3×"2") honeycomb chains. At a coverage of 1/2 ML, the (2×1) Seiwatz chains are experimentally observed. [269, 270] At intermediate coverages, divalent adsorbates are known to stabilize mixed chain structures with higher periodicity consisting of a combination of honeycomb chains and Seiwatz chains. The simplest combination alternates between honeycomb and Seiwatz chains, resulting in (5×1) unit cell, as

shown in Fig. 4.10(c). The (5×"2") periodicity observed for divalent adsorbates may be thought of as being built from two (3×1) honeycomb-chain units and two (2×1) Seiwatz-chain units.
We have calculated the surface energies of a variety of candidate reconstructions based on the divalent adsorbate Ca, including pure honeycomb chains with coverages θ=1/3 and 1/6 ML, pure Seiwatz chains with coverages θ=1/2 and 1/4 ML, and the mixed configuration alternating between honeycomb and Seiwatz chains with adsorbate coverages θ=2/10, 3/10, and 4/10 ML. A new consideration arises for Ca, because Si and Ca can form a variety of stable bulk silicides, such as $CaSi_2$ and Ca_2Si. To prevent precipitation of these bulk phases, the Ca and Si chemical potentials must also satisfy the inequalities

$$\mu_{\mathrm{Ca}} + 2\mu_{\mathrm{Si}} \leq \mu(\mathrm{CaSi_2}), \tag{4.3}$$
$$2\mu_{\mathrm{Ca}} + \mu_{\mathrm{Si}} \leq \mu(\mathrm{Ca_2Si}), \tag{4.4}$$

where $\mu(CaSi_2)$ is the energy per formula unit of $CaSi_2$, and likewise for Ca_2Si. Since μ_{Si} is fixed, these constraints have the effect of further lowering the highest allowed value of μ_{Ca}.
The resulting surface energies for Ca-induced reconstructions are shown in Fig. 4.11(b). To keep the figure uncluttered we have only plotted the phases that are stable, or close to stable, for some allowed value of μ_{Ca}. Two Ca-induced phases are thermodynamically stable: the HCC reconstruction with θ=1/6 ML (blue) and the Seiwatz-chain reconstruction with θ=1/2 ML (green). The mixed HCC+Seiwatz configuration with θ=3/10 ML (red line) is energetically just above these two phases, but passes so close (within 1 meV/Å^2) to their intersection point that its formation cannot be ruled out. Experimentally, the mixed configuration is indeed found at coverages between those of the two pure phases.

Trivalent adsorbates

Experiments using trivalent adsorbates (Gd, Dy, Er, Ho) reveal a mixed configuration with (5×"2") periodicity consisting of alternating honeycomb and Seiwatz chains, as shown in Fig. 4.10(c). Pure honeycomb or pure Seiwatz chain structures are not observed. We have calculated the surface energies of a number of hypothetical Gd-induced configurations, including pure honeycomb chains with every channel site occupied (θ=1/3 ML), every second site occupied (θ=1/6 ML), and every third site occupied (θ=1/9 ML), as well as of Seiwatz chains with every channel site occupied (θ=1/2 ML), and every second site occupied (θ=1/4 ML). We also considered three mixed configurations with θ=2/10, 3/10, and 4/10 ML. Finally, we also calculated the surface energy for the well-studied epitaxial $GdSi_2$ silicide, which consists of 1 ML of Gd on Si(111) in the so-called "B-T4" structure. [303, 317]
The resulting surface energies for Gd-induced reconstructions are shown in Fig. 4.12(a). As before, we plot only the phases that are stable, or nearly so. There are

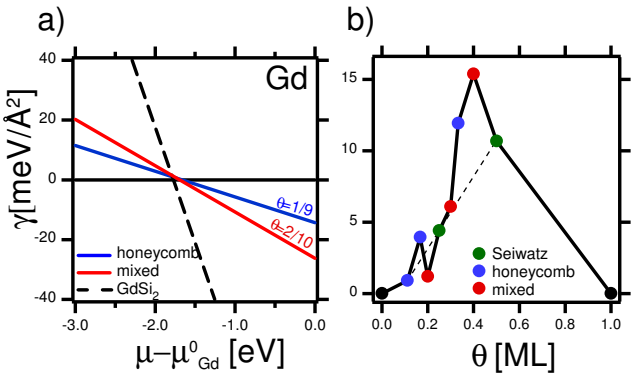

Figure 4.12: (Color online) (a) Surface-energy diagram for the trivalent adsorbate Gd. We compare pure honeycomb chains (θ=1/9, blue) and a mixed chain configuration with alternating honeycomb and Seiwatz chains (θ=2/10, red). The horizontal line represents Si(111)-(7×7) (θ=0 ML, black), and the dashed line represents the $GdSi_2$ silicide film (θ=1 ML). (b) Surface energies of Gd phases plotted as a function of coverage. Only the points have meaning; the lines are added for clarity.

two thermodynamically stable phases, the bare Si(111)-(7×7), and the $GdSi_2$ silicide phase with θ_{Gd}=1. None of the Gd-chain reconstructions is thermodynamically stable within DFT.

To investigate the possibility that the experimentally observed phases are kinetically stable, we examine in more detail the energetics of all phases with intermediate Gd coverage. In particular, we are interested in the tendency of an adsorbate phase with intermediate coverage θ_{Gd} to separate into two stable phases, one with lower coverage θ^{-}_{Gd} and one with higher coverage θ^{+}_{Gd}. Let x denote the fraction of the total surface area occupied by the higher coverage phase. Then the average coverage of the two phases is simply $x\theta^{+}_{Gd} + (1-x)\theta^{-}_{Gd}$. If x is chosen such that this average coverage is equal to the coverage θ_{Gd} of the homogeneous phase, then the surfaces energies of the homogeneous and inhomogeneous phases can be compared directly, without the need for specifying a chemical potential. To make this comparison simple we return to Eq. 2 and now regard the surface energy gamma as a function of coverage θ_{Gd} for a fixed, arbitrary value of chemical potential μ_{Gd}. Although the surface energies for the individual phases depend explicitly on μ_{Gd}, the energy difference between the two alternative scenarios (the homogeneous phase versus the phase-separated phase) with the same average coverage does not. For display purposes we choose a value for which the two endpoint phases have equal surface energies.

The resulting surface energies, for all the Gd chain phases we have considered, are plotted in Fig. 4.12(b) relative to the endpoint phases, as a function of Gd coverage. For intermediate Gd coverages, the surface energy is always higher than at the endpoints. Thus, a surface prepared with intermediate coverage will, under conditions of thermodynamic equilibrium, phase separate into an appropriate mixture of the two endpoint phases. But what about conditions under which thermodynamic

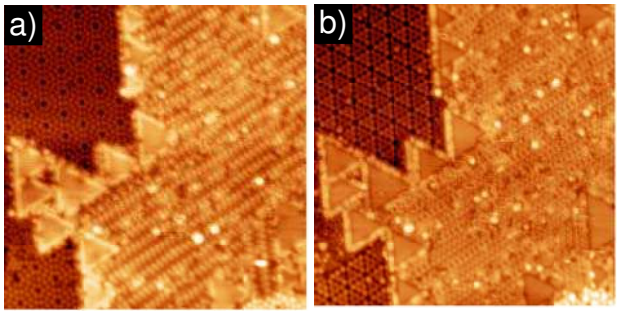

Figure 4.13: (Color online) (a) Empty and (b) filled-state STM image of Si(111) surface after Gd deposition and subsequent annealing. Atomic chains coexist with clean areas with the Si(111)-(7×7) reconstruction separated by triangular $GdSi_2$ islands. U=±1.8 V, I=0.18 nA, 45 nm×45 nm.

equilibrium cannot be achieved?
There are good reasons to consider this scenario. The conversion of an intermediate phase to a combination of bare (7×7) and the $GdSi_2$ silicide phase requires a considerable rearrangement of the top several atomic layers; this restructuring may be kinetically hindered. On the other hand, the structural differences among the various Gd-chain phases are relatively minor: for example, all are quasi-one dimensional with similar underlying building blocks. Thus, the thermodynamically favored endpoint phases may be kinetically inaccessible, even though equilibrium is achieved among the subset of structurally similar chain phases with intermediate coverage.

To analyze the consequences of this hypothesis, we apply the Maxwell construction to the phases with intermediate Gd coverage. This geometrical analysis allows one to answer the question of which, if any, intermediate phases are stable against phase separation into appropriate mixtures of other phases. We consider again the results in Fig. 4.12(b) and construct an analogous plot (not shown), this time with the (7×7) and $GdSi_2$ endpoints excluded. Of the remaining phases, only one is stable with respect to phase separation into all possible other pairs: the (5×2) mixed HCC+Seiwatz phase with θ_{Gd}=2/10. This conclusion is easy to visualize in Fig. 4.12(b) by simply drawing straight lines between all possible pairs of phases; the dotted line shows one such example, demonstrating the stability of the θ_{Gd}=2/10 phase with respect to separation into the two endpoint phases, with θ_{Gd}=1/9 and θ_{Gd}=1/2.
These findings are indeed consistent with our experimental observations. Starting with the deposition of 2/10 ML Gd onto the substrate held at 680^o C, followed by short annealing still at 680^o C and a cool-down to room temperature, one obtains a surface uniformly covered with atomic chains. After annealing for a slightly longer period or at slightly higher temperatures, phase separation may directly be observed in STM images (see Fig. 4.13): triangles of $GdSi_2$ silicide form together with regions of clean Si(111)-(7×7) coexisting with the chains. Further annealing completely transforms the chains into silicide islands and areas with Si(111)-(7×7).

4.7.4 Conclusion

We used first-principles total-energy calculations and scanning tunneling microscopy to study the stability and structure of atomic chains of monovalent, divalent, and trivalent adsorbates on Si(111).
For monovalent adsorbates the theoretical and experimental results are in excellent agreement, both identifying the honeycomb-chain channel (HCC) reconstruction with adsorbate coverage $\theta = 1/3$ as the only stable chain phase.
For divalent adsorbates three chain phases are found experimentally, corresponding to coverages 1/6, 1/2, and intermediate values. These findings are corroborated by our total-energy calculations, which identify the three lowest-energy phases as a half-occupied HCC phase, a fully occupied Seiwatz-chain phase, and a simple combination of these.
For trivalent adsorbates, our total-energy calculations indicate that the observed combination of HCC and Seiwatz phases with adsorbate coverage 2/10 is kinetically stable with respect to phase separation into other, thermodynamically stabler phases.
For all adsorbates, the thermodynamically (or kinetically) stable phases all obey a surprisingly simple electron-counting rule proposed earlier [304, 312].

Acknowledgments

We thank Franz J. Himpsel for stimulating discussions. The help of Leslie-Anne Fendt, Samuel Hoffmann, Claude Monney and Christoph Walther is gratefully acknowledged. Skillful technical assistance was provided by our workshop and electric engineering team. This work was supported by the Fonds National Suisse pour la Recherche Scientifique through Div. II, MaNEP and the US Office of Naval Research. Computations were performed at the DoD Major Shared Resource Center at ASC.

4.8 Indium induced chains

Deposition of 1 ML of indium on Si(111) induces a chain reconstruction with (4×1) symmetry reported for the first time by Lander and Morrison in 1965 [318]. Structural models for the Si(111)-(4×1)-In system were proposed by Collazo-Davila *et al.* [319], Saranin *et al.* [320–322] and others [323]. The now widely accepted structural model has been proposed by Bunk *et al.* [324] in 1999 based on surface x-ray diffraction data. This model has been confirmed by IV-LEED [325] and its bandstructure derived within DFT [326–339] is consistent with experimental photoemission data [310, 340–349]. At room temperature three partially filled bands cross the Fermi energy. The respective band fillings are 11%, 38% and 50%. Thus a total of two electrons fill the three metallic surface states. Simulated STM images also agree with experiment [307–309, 320, 321, 328, 330, 346, 350–354] and results from other techniques [348, 355–361] are consistent with the model proposed by Bunk.
Bunk's model consists of Si Seiwatz chains separated by a large channel in which the four In adsorbates per unit cell are located. The structure can be understood as being composed of alternating Si and In Seiwatz chains separated by standard channels in which the remaining In atoms are found. From an electron counting perspective, we know that Si Seiwatz chains require two additional electrons to be stabilized. How about the In Seiwatz chains? In has one valence electron less than Si. From this point of view we need four additional electrons if one wants to stabilize Seiwatz chains using In atoms. Two more In atoms are found in the channel providing exactly six electrons. However, this picture is not consistent with the two electrons found in the three metallic surface states. Seiwatz chains formed by In atoms may require less than four electrons for bonding leaving two electrons in partially filled metallic states. A character analysis of the surface state bands by Cho *et al.* [327] shows that the electrons in the bands with filling 11% and 38% are located on the In Seiwatz chain.
In 1999, Yeom *et al.* [344] reported a temperature induced phase transition around 120 K [362] from the metallic state into a semiconducting state with (8×2) symmetry. Initially Yeom *et al.* [344] proposed a single band Peierls type nesting scenario for the half-filled band, being responsible for the opening of a gap at the Fermi energy and the ×2 modulation along the chains. In a later paper [310], they proposed that also the other two bands open an energy gap through an interband charge transfer mechanism. The basic idea of a Peierls instability for the In chains was recently challenged by an explanation based on dynamic structural fluctuations put forward by Gonzáles *et al.* [335]. The subject is currently hotly debated in the community [336, 338, 339, 348, 362, 363].

4.9 Gold induced chains

Au induces an atomic chain reconstruction on the Si(111) surface at a coverage of 2/5 ML. Early LEED studies [364, 365] already observed the (5×"2") pattern, and

the ×"2" streaks were already correctly interpreted as being due to random registry shifts between adjacent chains [365]. Early models considered chains formed by Au atoms [365, 366]. STM images however indicated a more complicated structure [367–370]. Based on a combination of high resolution electron microscopy and transmission electron diffraction Marks and Plass [371] suggested a reconstructed model with two Au rows in between silicon trenches. Early ARPES results suggested the presence of a one-dimensional electron band, which has been reported to be metallic [372]. A subsequent ARPES study revealed the opening of a Peierls-like pseudogap at low temperature [156, 373]. A reinvestigation of the electronic bandstructure in 2003 revealed that even at room temperature the Si(111)-(5×"2")-Au reconstruction is semiconducting questioning the proposed Peierls scenario [374]. Bennewitz *et al.* [375–377] were able to identify the protrusions seen in STM images on top of the chains as Si adatoms by evaporating additional Si atoms onto the chains. These form a (5×4) superlattice at saturation coverage [378]. Erwin [311] proposed a new structural model containing a Si honeycomb chain and a mixed Si-Au honeycomb chain which is decorated by additional Si adatoms. The role of the additional Si adatoms is to stabilize the mixed Si-Au honeycomb chain by doping the associated electronic bands with electrons. The model is able to reproduce all main features observed in STM and ARPES. In 2004 Yoon *et al.* [379, 380] demonstrated using STS that the chains consist of a series of alternating metallic and semiconducting segments. Segments free of additional Si adatoms are metallic, whereas segments with Si adatoms are semiconducting. In 2005 Riikonen and Sánchez-Portal [381] revisited existing structural models for the Si(111)-(5×"2")-Au reconstruction within DFT. They also reconsidered the model proposed by Marks and Plass [371] and noted that silicon honeycomb chains spontaneously form during structural relaxation. However the model of Marks and Plass was rejected since neither the simulated STM images nor the calculated bandstructure compares satisfactorily with the experimental data. They also studied in detail the model proposed by Erwin [311]. In addition they found another model to be relatively stable. This model is similar to the model proposed by Erwin and also contains honeycomb chains, but the position of the surface dislocation is different. The calculated bandstructures without additional adatoms are quite similar and are in reasonable agreement with experiment. However as a function of the concentration of additional silicon adatom, the two models behave differently. Whereas the surface energy of Erwin's model decreases with the addition of adatoms, the addition of adatoms is always unfavorable for the alternative model. Based on total energy calculations Ren *et al.* [382] found another alternative candidate with a low energy obtained by the removal of one silicon atom per unit cell from the model proposed by Riikonen and Sánchez-Portal. In this model, the addition of Si adatoms correctly reproduces the transition from a metallic to an insulating state. However, the Si surface atom density of 13 ± 1 Si atoms per (5×2) unit cell determined by Chin and Men [383] via a mass transport analysis by STM is not able to discriminate between these models. Choi *et al.* [384] have just published a paper where they study the electronic

bandstructure as a function of Si adatom concentration with ARPES. Increasing the adatom coverage, the one-dimensional electronic band changes from a fully metallic character to a semiconducting one with a band gap increasing above 0.3 eV. They suggested that the band gap opening is related to the ordering of the Si adatoms. Au also stabilizes atomic chain reconstructions on high-index Si surfaces [154, 155, 160]. In 1999 Segovia *et al.* [147] from Prof. Baer's group in Neuchâtel published first ARPES results on the Au/Si(557) atomic chain system obtained at a coverage of 0.2 ML. A one-dimensional, metallic state was found on that surface at $T \approx 10$ K, suggesting that the threat of a Peierls transition could be avoided by rigidly anchoring the chain atoms on the Si substrate via covalent bonds. They further observed a splitting of the surface state near the Fermi energy leading them to suggest the possibility for the existence of spin-charge separation in this system. This publication triggered intense research in the field of atomic chains. In 2001, Losio [157] optimized the surface quality with the help of STM. Using ARPES with a photon energy of $h\nu = 34$ eV, which is the optimum energy for a strong cross section of the surface state, they showed that the splitting persists up to the Fermi level and can therefore not be attributed to the spinon-holon splitting in a Luttinger liquid. Instead, they proposed that the splitting between the two almost degenerate bands may be explained by the double chain structure observed in their STM images. For a photon energy of $h\nu = 21.2$ eV used by Segovia [147], the Fermi edge becomes so weak that the splitting of bands at the Fermi energy could not be observed. A structural model based on surface x-ray diffraction measurements was proposed in Ref. [385]. It consists of a silicon honeycomb chain (see Fig. 2 in Ref. [163] for a good representation) adjacent to the step edge. Gold atoms are located inside a channel on the other side of the honeycomb chain. A row of additional Si adatoms is found between the Au channel and the silicon honeycomb chain of the upper terrace. Sánchez-Portal *et al.* [159, 386] independently proposed a very similar model and tested the influence of the position of the Au channel on the total energy, but finally also selected the location next to the silicon honeycomb chains in agreement with the model presented in Ref. [385]. In 2003 Ahn *et al.* [162] reinvestigated the electronic structure by ARPES. They observed that only one of the two surface bands is metallic, whereas the second almost degenerate surface band exhibits a band gap of 50 meV at room temperature. Upon cooling, the metallic branch was found to undergo a metal-insulator transition with a band gap saturating at 80 meV. Furthermore using STM, they observed period doubling in real space of one of the chains across the phase transition, whereas the periodicity of the first chain is already doubled at room temperature. The surface conductivity of the chains has been measured by a microscopic four-point probe method using an independently driven four-tip STM [387] showing semiconducting behavior with a gap of 55 mV as a function of temperature. In 2004 Sánchez-Portal *et al.* [28] included spin-orbit coupling into their DFT calculations resulting in a Rashba splitting of the one-dimensional surface state, which agrees nicely with the splitting observed in ARPES, initially attributed to spin-charge separation. The apparent Peierls-like

transition observed by Ahn *et al.* [162] is explained as being the result of dynamical fluctuations of the step-edge structure, which are quenched as the temperature is decreased. A reinvestigation of the chains using STS by Yeom *et al.* [170] denied this mechanism based on the fluctuation of the step-edge buckling. In 2007, based on ARPES measurements on the related Au/Si(553) atomic chain system, Barke *et al.* [186] concluded that the observed pattern of avoided crossings in the band structure is consistent with the Rashba picture. In principle spin-resolved ARPES could resolve the question, but the requirements of high energy and angle resolution are difficult to combine with the low count rate imposed by spin detection. Support for the Rashba picture comes also from the measurement of the one-dimensional plasmon dispersion [175]. The fact that only one band is metallic at room temperature as suggested by the ARPES data from Ahn *et al.* [162] is however difficult to explain within the spin-orbit picture. A discussion on this problem is given in Ref. [184] and further investigations are required to arrive at a consistent picture.
Au stabilizes atomic chain systems on several more high-index silicon surfaces. In 2003, Crain *et al.* [161] discovered atomic chains on the Si(553) surface, which was shown in an earlier study [160] to be stabilized by the adsorption of Au atoms. Due to its high perfection this system is very popular. A structural model based on DFT calculations comparing over 40 structural candidates has been proposed in Ref. [163]. The model with the lowest energy surprisingly does not contain a silicon honeycomb chain. However it is interesting to note that the hypothetical model proposed for the related Au/Si(775) system in the same paper contains the honeycomb chain building block. A more recent DFT study by Riikonen and Sánchez-Portal [171] again favored a structure build around the honeycomb chain over the model proposed in Ref. [163]. In 2005, Ghose [167] presented a new model based on surface x-ray diffraction. It consists of silicon adatoms and a double row of gold atoms at the step edge. However, calculated properties for this model are not in agreement with experiment and the structure is unstable within the local density approximation [336]. In 2007 Ryang *et al.* [182] calculated and compared the energetics of various structural models proposed so far and concluded that the most stable structure is composed of a single Au row in a channel on the terrace and the Si honeycomb chain at the step edge. This model further excellently reproduces the observed STM images. Riikonen and Sánchez-Portal [388] further submitted a new paper, where they consider more than 200 structural candidates. Finally the most stable model contains again the honeycomb structure at the step edge and simulated STM images and the derived bandstructure agree well with experiment.
In analogy with the Au/Si(557) chains, the Au/Si(553) system also exhibits a doublet of 1/2-filled one-dimensional surface bands, but in addition, Au/Si(553) shows an extra, nearly 1/3-filled, band. At low temperature STM revealed the intriguing coexistence of a triple- and double period lattice distortion [169, 178] (see Fig. 4.1). ARPES [169] observed both the nearly 1/3- and 1/2-filled bands to gradually open energy gaps. These unusual findings have been interpreted as being due to the occurrence of two successive Peierls distortions with different transition temper-

atures on two different chain elements [169, 178]. The surface conductivity of the Au/Si(553) system has been measured by the four-tip STM [181] showing a metal-insulator transition at around 160 K in agreement with other experimental data.
A similar chain system which also exhibits three bands has been found on Si(775) [163]. The flat bands near the Fermi energy are however nearly filled, suggesting a semi-metallic bandstructure. Atomic chains on Si(335), with two bands, resemble more the Au/Si(557) system but with different fillings [163]. Further Au induced chain systems have been found and studied on Si(995) [163], Si(13,13,7) [163], Si(5,5,12) [155, 158, 164, 389] and Si(110) [163, 390]. Most of these atomic chain systems are believed to consist of the honeycomb chain unit allowing to adjust the interchain coupling and the band-filling systematically by varying the substrate vicinality [163]. Thus Au induced atomic chains make a highly flexible family of solids approaching the one-dimensional limit.

4.10 Open questions and conclusion

Atomic chains on silicon surfaces have proved to be an important playground for the exploration of one-dimensional physics. Interestingly the basic structural building blocks for the construction of atomic chains are always the same, namely silicon honeycomb and Seiwatz chains. Our results presented in this chapter did not only allow to enlarge the family of honeycomb and Seiwatz chains to trivalent adsorbates, but also to develop a coherent picture of the mechanisms behind the self-assembly process establishing the link between adsorbate valence and allowed periodicity. In the 2007 edition of the productive nanosystems technology roadmap [1], prior importance has been attributed to the identification of such atomically precise building blocks. Furthermore a detailed understanding of the mechanisms behind the self-assembly process is not only of fundamental interest but is also of high technological relevance.
Besides open questions related to the electronic structure of the In and Au induced chain systems discussed in sections 4.8 and 4.9, the electronic structure of the honeycomb and Seiwatz chains is relatively well understood. In what follows we discuss further directions, which are worth being explored.
A detailed comparison of experimental and theoretical IV-LEED data of the Si(111)-(5×"2")-Gd is still lacking, but would add further support to our ideas. Gd phaseshifts have been generated with the Barbieri/van Hove phaseshift package [20] and compare excellently to bulk Gd phaseshifts from the literature [391]. The difference in phaseshifts calculated for atoms located in the bulk vs atoms located at the surface appears to be negligible in a first approximation. We performed first trial calculations with a highly symmetric, non-relaxed model. Although the agreement between integer spots was quite good, comparison of satellite spots was not satisfactory. A second calculation used relaxed coordinates from our DFT calculations as a starting point. The use of relaxed coordinates strongly influences the satellite spots.

However, these relaxed coordinates were obtained with a model were one of the Gd atoms is sitting in a H_3 site, which we found to be energetically less favorable than the T_4 site. So a calculation taking coordinates from the model with the lowest energy configuration as a starting point promises improvement. Once a satisfying starting configuration has been found, the coordinates may further be refined by CLEED.

Further confirmation for our model could be obtained by determining the silicon surface atom density for the Si(111)-(5×"2")-Gd system in analogy with the work by Saranin [231–233, 262] for the monovalent and divalent adsorbates. According to our model to value should be 12/10 ML (8 honeycomb chain and 4 Seiwatz chain silicon atoms per (5×2) unit cell). Such a study requires very flat samples and measurements must be carried out far away from steps. Furthermore this method requires knowledge of the structure of all other phases present on the surface. Electromigration effects imposed by the direct current heating method should also be eliminated by annealing the sample by a resistive heater for example.

Investigations on the (5×"2") chain systems of the other trivalent rare earth adsorbates should also be carried out to verify the universality of our theory. However, due to the expected kinetic stability of these systems, their single domain preparation over macroscopic areas requires careful optimization of the growth parameters.

Roman Fasel suggested to me the possibility of mixing adsorbates of different valence to attain chain symmetries which are not allowed for individual adsorbates. These are though experiments, since the mixed chain configurations involving honeycomb and Seiwatz chains have been shown in section 4.7 to be only kinetically stable, leaving only a small window in parameter space to stabilize these chains. The two adsorbates must be chosen very carefully since every adsorbate has its own desorption temperature, reactivity and diffusion properties. Furthermore possible high coverage silicide phases, which are thermodynamically stable, may render two adsorbates incompatible.

Prof. Franz J. Himpsel asked me if I see a possibility to include the In and Au chains into our systematics. A preliminary discussion has been given for the Si(111)-(4×1)-In system in section 4.8. Currently our theory considers transfer of charge from the adsorbates to the chains in integer units of the electron charge. In order to account for the partially filled bands observed in these systems, partial charge transfer must be considered. I think, a careful analysis of DFT results allows to answer this question. However, most available DFT calculations on atomic chains use plane waves as a basis set. An analysis of charge transfer is much easier within the APW basis set, since it allows the analysis of the band characters by simple integration of the charge within the muffin tins. We already acquired experience in performing such analysis for transition metal trichalcogenides [392]. The problems is that the APW basis set requires more computational resources than the plane wave approach, and we currently do not have enough computational power to perform such calculations in Neuchâtel.

Cerium has been reported to stabilize an atomic chain reconstruction with (5×"2")

periodicity. Ce is a quite special element since its tetravalent state is energetically relatively close to its trivalent state [295]. The reconstruction phase diagram of Ce is far from simple including phases with (2×2), (2×1), ($\sqrt{3} \times \sqrt{3}$), ($2\sqrt{3} \times 2\sqrt{3}$), ($\sqrt{7} \times \sqrt{7}$) and ($\sqrt{48} \times \sqrt{48}$) periodicity [393,394]. Goshtasbi Rad *et al.* [393] additionally found a (3×2) phase and noted that the associated Si 2p core-level spectrum exhibits similarities with the spectra for the Yb and Sm induced (3×"2") chains. Recently they located an additional (5×2) phase [394]. Lee *et al.* [395] even reported two (5×2) phases obtained at two different coverages. However, more experimental data is required to arrive at a conclusive picture for the Ce chains. Additional experimental effort is also required for the intriguing (5×2) reconstruction stabilized by Ag observed in Ref. [210], probably at a coverage below 1/3 ML.

Another interesting route is to study to role of defects observed in the chains. We have discussed the zig-zag and ladder type configuration of the chains, directly observable in STM images, in section 4.5. At the frontier between these two configurations, charge is missing. In analogy with the self-doping mechanism proposed by Erwin [311] for the Si(111)-(5×"2")-Au system, we have speculated that the role of Si adatoms, which are ejected during the transformation from the Si(111)-(7×7) to the Si(111)-(5×"2")-Gd reconstruction, is to compensate local charge deficiencies. These ideas could be tested theoretically.

Gd and other rare earth metals carry a magnetic moment. Magnetic properties of the chains have so far not been explored at all, but since the chains are quasi one-dimensional there might be interesting consequences from the Mermin-Wagner theorem. But it remains an open question if there is a direct or possibly indirect magnetic coupling, via the silicon chains, of the individual Gd adsorbates, leaving a lot of room for physicists to explore alternative scenarios.

Chapter 5

Appendix

Acknowledgments

J'aimerais d'abord exprimer mes remerciements au Prof. Philipp Aebi pour m'avoir accueilli au sein de son groupe et avoir dirigé ma thèse. Son soutien, sa générosité, la disponibilité et la confiance qu'il a su m'accorder, ont été un apport précieux pour ce travail.
J'adresse également mes remerciement au Prof. Wolf-Dieter Schneider, Prof. Christophe Ballif et Dr. Pascal Ruffieux, membres du jury, pour avoir accepté de juger ce travail et avoir pris le temps de le lire.
J'aimerais remercier mes anciens et actuels collaborateurs du groupe 10^{-11} qui ont contribué quotidiennement à la maintenance des machines et à la bonne ambiance au travail. Gunnar Garnier pour ses précieux conseils techniques aux labos ainsi que sur l'eau. Ta cascade dans les vagues au large de la Corse restera graver dans mon souvenir. Claude Monney, mon conseiller scientifique numéro 1, de m'avoir supporté dans mon bureau. Merci pour cette inoubliable sortie au lac à travers les troncs d'arbres et bonne chance avec ton fireball! Christian Koitzsch pour m'avoir initié à la photoemission et avoir osé m'accompagner pendant mes premières excursions sur l'eau. Désolé pour le Mg/W(110). Laurent Despont pour les 100 kg au trapèze et de nous avoir rendu jaloux car il était le seul à savoir vivre deux couchers de soleil par jour pendant ses années à Neuchâtel. Florian Clerc, que j'aurais presque été tenté d'oublier de remercier, et Eike Bab Schwier, pour ses explications relatives au Weißwurschtäquator et au Röstigraben. J'aimerais particulièrement remercier mes postdocs nancéiens Hervé Cercellier et Clément Didiot pour l'excellente collaboration au niveau atomique. Merci aussi à Oliver Gallus, qui m'a initié aux chaînes atomiques, et à Laure Perret-Aebi, Pawel Starowicz et Marc Bovet.
J'aimerais à cette place aussi remercier les membres de l'atelier mécanique, Christian Hêche, Jean-Pierre Bourquin, André Cornu, Thierry Delhove, Isidro Fernandez et Dominique Schenker ainsi que les membres de l'atelier électronique Urs Bart et Daniel Varidel qui ont toujours su réaliser l'impossible. Leur expérience et leur créativité ont significativement contribué à resoudre les nombreux problèmes tech-

niques recontrés pendant cette thèse. Merci aussi aux membres de l'administration Anne-Marie Milo Romano, Muriel Vallery-Muegeli, Nicole Derendinger et Gianfranco Di Rocco.
Je dois un grand merci à mes agents de littérature Leslie-Anne Fendt, Samuel Hoffmann et Christoph Walther qui m'ont approvisionné avec des articles pendant ces dernières années. J'aimerais aussi remercier les anciens du groupes du Prof. Piero Martinoli, Oscar J. Cubero Garcia, Alain Rüfenacht, Veronica Marconi et surtout Ricardo Théron pour les nombreuses discussions et de m'avoir prêté du matériel. Merci aux spécialistes Linux du groupe du Prof. Jérôme Faist et Daniel Hofstetter, Tobias Gresch et Marcel Graf pour avoir sauvé de temps en temps nos ordinateurs de calcul. J'aimerais aussi remercier Mirko Bödecker, Danick Briand et Antje Schmalstieg pour leur aide.
Je remercie chaleureusement l'équipe de l'EMPA Oliver Gröning, Roman Fasel, Roland Widmer, Gilles Buchs, Marta Cañas-Ventura et surtout Pascal Ruffieux pour m'avoir acceuilli à Thun pour l'apprentissage du STM. Un grand merci à Pascal qui était toujours à l'écoute, quand j'avais des problèmes avec mon STM.
It has been a great pleasure collaborating with physicists from around the globe. In particular I would like to thank Prof. Franz J. Himpsel for stimulating discussions on atomic chains and catamarans, and for suggesting me to contact Steven C. Erwin. I thank Steven C. Erwin for sharing his deep insights on atomic chains with me and for the fruitful collaboration. I also owe my thanks to Katalin Gaàl-Nagy who performs the calculations on the Si(331) system. I further would like to thank Georg Held for his first-class support for his multiple scattering code and Prof. Randall M. Feenstra for answering my questions on bandbending. I further thank Prof. Alexander A. Saranin and Prof. Han Woong Yeom for discussions on silicon surface reconstructions, Fransisco Javier Garcia de Abajo for help with his multiple scattering code, Prof. Franco Jona for discussions on the Gd phaseshifts, and Michelle Johannes for citing my paper for the first time and for illuminating my view on Fermi surface nesting. Helpful advice and suggestions during the development of the IV-LEED setup by José A. Martín-Gago and Celia Rogero are also acknowledged.
Les années de thèse ne sont pas marquées uniquement par la recherche. Je remercie mes amis d'Ichtus, de la société nautique, du cercle de la voile et des Glénans pour les nombreuses heures de plaisir sur l'eau ainsi que les membres de mon groupe de musique. Je remercie mes étudiants en médicine et biologie pour leur motivation pour la physique expérimentale et mes étudiants en aviron pour avoir évité de couler un bateau. J'aimerais aussi remercier mes amis dans le canton d'Uri, Franziska et Angel, pour m'avoir accueilli avec les bras ouverts lors de mes nombreuses visites non-annoncées. Finalement j'aimerais exprimer ma reconnaissance à ma famille et à Soyoung pour leur soutien.

Curriculum Vitae

Name	Corsin BATTAGLIA
Date of birth	October 7, 1977
Origin	Salouf, Graubünden
Nationality	Swiss
E-mail	corsin.battaglia@unine.ch
Languages	German, English, French, some Italian and Korean

Education

2004-2008	PhD in physics, Université de Neuchâtel "Structural and electronic properties of self-assembled nanostructures on silicon surfaces" Image of the month May 2007, Swiss National Science Foundation
1998-2004	Diplôme de physicien, mention bien, Université de Neuchâtel "Fermi surface nesting" Omega student award 2004
1997-1998	Musician's Institute, Hollywood, USA Most promising student award 1998
1990-1997	Federal matura type B (latin), Gymnasium Karl Borromäus, Uri
1984-1990	Primary school, Uri

Professional Experience

2004-2008	Institut de physique, Université de Neuchâtel PhD student and teaching assistant in the electron spectroscopy group of Prof. P. Aebi, study of low-dimensional nanostructures at surfaces by scanning tunneling microscopy, photoemission spectroscopy, low-energy electron diffraction and density functional theory
Summer 2003	Hitachi High-Technologies Corporation, Hitachinaka-shi, Japan IAESTE traineeship in the electron optics group of M. Sato, development of a new magnetic lens for scanning electron microscopes
Summer 2002	Paul Scherrer Institute PSI, Villigen Traineeship in the low temperature facilities group of Dr. B. van den Brandt, optimization of dynamic nuclear polarization of protons via electron spin and nuclear magnetic resonance spectroscopy and neutron scattering

Publications

C. Koitzsch, C. Battaglia, F. Clerc, L. Despont, M.G. Garnier, P. Aebi,
Photoemission of a quantum cavity with non-magnetic spin separator,
Phys. Rev. Lett. **95**, 126401(2005)

C. Battaglia, H. Cercellier, F. Clerc, L. Despont, M.G. Garnier, C. Koitzsch, H. Berger, L. Forro,C. Ambrosch-Draxl, P. Aebi,
Fermi surface induced distortion in $NbTe_2$,
Phys. Rev. B **72**, 195114 (2005)
http://arxiv.org/abs/cond-mat/0508097

F. Clerc, C. Battaglia, M. Bovet, L. Despont, C. Monney, H. Cercellier, M.G. Garnier, P. Aebi,
Lattice-distortion-enhanced electron-phonon coupling and Fermi surface nesting in 1T-TaS_2,
Phys. Rev. B, **74**, 155114 (2006)

P. Starowicz, C. Battaglia, F. Clerc, L. Despont, A. Prodan, H.J.P. van Midden, U. Szerer, A. Szytula, M.G. Garnier, P. Aebi,
Electronic structure of $ZrTe_3$,
J. Alloys Comp. **442**, 268 (2007)

F. Clerc, C. Battaglia, H. Cercellier, C. Monney, H. Berger, L. Despont, M.G. Garnier, P. Aebi,
Fermi surface of layered compounds and bulk charge density wave systems,
J. Phys.: Condens. Matter **19**, 355002 (2007)

C. Battaglia, H. Cercellier, L. Despont, C. Monney, M. Prester, H. Berger, L. Forro, M.G. Garnier, P. Aebi,
Non-uniform doping across the Fermi surface of NbS_2 intercalates,
Eur. Phys. J. B **57**, 385 (2007)
http://arxiv.org/abs/cond-mat/0611215

H. Cercellier, C. Monney, F. Clerc, C. Battaglia, L. Despont, M.G. Garnier, H. Beck, P. Aebi, L. Patthey
Spectral function of an excitonic insulator: theoretical and ARPES study of 1T-$TiSe_2$,
Phys. Rev. Lett. **99**, 146403 (2007)
http://arxiv.org/abs/0704.0159

C. Battaglia, H. Cercellier, C. Monney, M.G. Garnier, P. Aebi,
Stabilization of silicon honeycomb chains by trivalent adsorbates,
Europhys. Lett. **77**, 36003 (2007)
http://arxiv.org/abs/cond-mat/0611776

C. Battaglia, H. Cercellier, C. Monney, M.G. Garnier, P. Aebi,
Unveiling new systematics in the self-assembly of atomic chains on Si(111),
Proceedings of the International Conference on Nanoscience and Technology ICN+T 2007,
J. Phys.: Conf. Ser. 100, 052078 (2008)
http://arxiv.org/abs/0706.3175

C. Battaglia, P. Aebi, S. Erwin
Stability and structure of atomic chains on Si(111),
submitted to Phys. Rev. B
http://arxiv.org/abs/0805.1843

C. Battaglia, K. Gaál-Nagy, C. Didiot, C. Monney, E.F. Schwier, M.G. Garnier, P. Aebi,
A new structural model for the Si(331)-(12×1) reconstruction,
to be submitted

C. Monney, H. Cercellier , F. Clerc, C. Battaglia, E.F. Schwier, C. Didiot, M.G. Garnier,
H. Beck, P. Aebi, L. Patthey, H. Berger, L. Forró
Spontaneous excitonic condensation in 1T-$TiSe_2$: a BCS-like approach,
to be submitted

Presence in public media

L'Express
Des colliers d'atomes assemblés par l'Université de Neuchâtel
May 23 2007

Tages-Anzeiger
Bauanleitung für Nanodrähte
May 24 2007

Le Matin Bleu
Mode d'emploi pour nanocolliers
May 25 2007

Trait d'union No 49
Nanocolliers d'atomes
May 2007

Chemische Rundschau No 6
Silizium organisiert sich selbst
June 6 2007

FNS Info No 1
Des physiciens lèvent un voile sur le monde des nanostructures:
Mode d'emploi pour la création de nanocolliers d'atomes
Physiker dringen weiter in die Welt der Nanostrukturen ein:
Eine Gebrauchsanweisung für den Bau von Nanoketten
June 2007

Alliance Info No 9
Mode d'emploi pour nano-colliers d'atomes
June 2007

Chemie Plus No 7-8
Aus der Welt der Nanostrukturen - Kette von Goldatomen wirkt als Nanodraht
July August 2007

Swiss Engineering - Revue Technique Suisse No 7/8
Créer des colliers d'atomes aux propriétées inouïes
July August 2007

Bibliography

[1] Battelle Memorial Institute and Foresight Nanotech Institute, Productive Nanosystems Technology Roadmap (2007).

[2] M. F. Crommie, C. P. Lutz, and D. M. Eigler, Science **262**, 218 (1993).

[3] H. J. Lee and W. Ho, Science **286**, 1719 (1999).

[4] S.-W. Hla, L. Bartels, G. Meyer, and K.-H. Rieder, Phys. Rev. Lett. **85**, 85 (2000).

[5] J. V. Barth, G. Costantini, and K. Kern, Nature **437**, 671 (2005).

[6] C. M. Niemeyer, Ang. Chemie **40**, 4128 (2001).

[7] N. C. Seeman, Trends in Biotechnology **17**, 437 (1999).

[8] J. C. Love *et al.*, Chem. Rev. **105**, 1103 (2005).

[9] International Technology Roadmap for Semiconductors, Process Integration, Devices, and Structures (2007).

[10] International Technology Roadmap for Semiconductors, Lithography (2007).

[11] V. V. Zhirnow, R. K. Cavin, J. A. Hutchby, and G. I. Bourianoff, Proceedings of the IEEE **91**, 1934 (2003).

[12] S. J. Tans, R. M. Verschueren, and C. Dekker, Nature **393**, 49 (1998).

[13] X. Duan *et al.*, Nature **409**, 66 (2001).

[14] S.-M. Koo *et al.*, Nanotechnology **16**, 1482 (2005).

[15] O. Boyraz and B. Jalali, Optics Express **12**, 5269 (2004).

[16] G. T. Reed and A. P. Knights, *Silicon Photonics* (Wiley, New York, 2005).

[17] S. Olibet, E. Vallat-Sauvain, and C. Ballif, Phys. Rev. B **76**, 035326 (2007).

[18] M. C. Hersam, N. P. Guisinger, and J. W. Lyding, Nanotechnology **11**, 70 (2000).

[19] T. Rakshit, G.-C. Liang, A. W. Ghosh, and S. Datta, Nano Lett. **4**, 1803 (2003).

[20] A. Barbieri and M. A. V. Hove, private communication (2007).

[21] G. Held, private communication (2006).

[22] Y. Baer, private communication (2002).

[23] H. E. Farnsworth, R. E. Schlier, T. H. George, and R. M. Burger, J. Appl. Phys. **29**, 1150 (1958).

[24] J. Wei, E. D. Williams, and R. L. Park, Surf. Sci. Lett. **250**, L368 (1991).

[25] J. M. Luttinger, J. Math. Phys. **4**, 1154 (1963).

[26] R. Peierls, *Quantum Theory of Solids* (Clarendon, Oxford, 1955).

[27] I. Barke, F. Zheng, T. K. Rügheimer, and F. J. Himpsel, Phys. Rev. Lett. **97**, 226405 (2006).

[28] D. Sánchez-Portal, S. Riikonen, and R. M. Martin, Phys. Rev. Lett. **93**, 146803 (2004).

[29] S. Hüfner, *Photoelectron Spectroscopy, Principles and Applications* (Springer, Berlin, 2003).

[30] G. Binnig and H. Rohrer, Nobel lecture (1986).

[31] G. Binnig, H. Rohrer, C. Gerber, and E. Weibel, Phys. Rev. Lett. **49**, 57 (1982).

[32] G. Binnig, H. Rohrer, C. Gerber, and E. Weibel, Phys. Rev. Lett. **50**, 120 (1983).

[33] G. Binnig, C. F. Quate, and C. Gerber, Phys. Rev. Lett. **56**, 930 (1984).

[34] D. W. Pohl, W. Denk, and M. Lanz, Appl. Phys. Lett. **50**, 651 (1984).

[35] Y. Martin and H. K. Wickramasinghe, Appl. Phys. Lett. **250**, 1455 (1987).

[36] M. Ternes, Thesis (2006).

[37] J. Tersoff and D. R. Hamann, Phys. Rev. Lett. **50**, 1998 (1983).

[38] J. Tersoff and D. R. Hamann, Phys. Rev. B **31**, 805 (1985).

[39] J. Bardeen, Phys. Rev. Lett. **6**, 57 (1961).

[40] N. D. Lang, Phys. Rev. B **34**, 5947 (1986).

[41] K. Takayanagi, Y. Tanishiro, M. Takahashi, and S. Takahashi, J. Vac. Sci. Technol. A **3**, 1502 (1985).

[42] K. Takayanagi, Y. Tanishiro, S. Takahashi, and M. Takahashi, Surf. Sci. **164**, 367 (1985).

[43] R. J. Hamers, R. M. Tromp, and J. E. Demuth, Phys. Rev. Lett. **56**, 1972 (1986).

[44] M. A. Green, J. Appl. Phys. **67**, 2944 (1990).

[45] F. Flores and N. Garcia, Phys. Rev. B **30**, 2289 (1984).

[46] R. M. Feenstra and J. A. Stroscio, J. Vac. Sci. Technol. B **5**, 923 (1987).

[47] R. M. Feenstra, J. Vac. Sci. Technol. B **21**, 2080 (2003).

[48] N. W. Ashcroft and N. D. Mermin, *Solid State Physics* (Thompson Learning, London, 1976).

[49] H. Lüth, *Solid Surfaces, Interfaces and Thin Films* (Springer, Berlin, 2001).

[50] M. Weimer, J. Kramar, and J. D. Baldeschwieler, Phys. Rev. B **39**, 5572 (1989).

[51] R. M. Feenstra, S. Gaan, G. Meyer, and K. H. Rieder, Phys. Rev. B **71**, 125316 (2005).

[52] R. M. Feenstra, SEMITIP code for electrostatic computations for a probe tip near a semiconductor
(URL http://www. andrew. cmu. edu/user/feenstra/semitipv2/) .

[53] S. M. Sze, *Physics of Semiconductor Devices* (Wiley, New York, 1981).

[54] W. Mönch, *Semiconductor Surfaces and Interfaces* (Springer, Berlin, 2001).

[55] R. M. Feenstra, private communication (2008).

[56] R. Losio, K. N. Altmann, and F. J. Himpsel, Phys. Rev. B **61**, 10845 (2000).

[57] F. J. Himpsel, G. Hollinger, and R. A. Pollack, Phys. Rev. B **28**, 7014 (1983).

[58] J. Ortega, F. Flores, and A. L. Yeyati, Phys. Rev. B **58**, 4584 (1998).

[59] S. Heike, S. Watanabe, Y. Wada, and T. Hashizume, Phys. Rev. Lett. **81**, 890 (1998).

[60] T. Tanikawa *et al.*, Phys. Rev. B **68**, 113303 (2003).

[61] J. W. Wells, J. F. Kallehauge, T. M. Hansen, and P. Hofmann, Phys. Rev. Lett. **97**, 206803 (2006).

[62] M. D'Angelo *et al.*, submitted to Phys. Rev. B (2008).

[63] J. Myslivecek *et al.*, Phys. Rev. B **73**, 161302R (2006).

[64] G. Dujardin, A. J. Mayne, and F. Rose, Phys. Rev. Lett. **89**, 036802 (2002).

[65] T. Yokoyama and K. Takayanagi, Phys. Rev. B **61**, R5078 (2000).

[66] M. Lastapis *et al.*, Low. Temp. Phys. **29**, 196 (2003).

[67] R. M. Feenstra, G. Meyer, and K. H. Rieder, Phys. Rev. B **69**, 081309R (2004).

[68] C. J. Davisson and L. H. Germer, Phys. Rev. **30**, 705 (1927).

[69] E. A. Wood, J. Appl. Phys. **35**, 1306 (1964).

[70] F. Jona, www. matscieng. sunysb. edu/ivdata/ (2007).

[71] G. Held, S. Uremovic, C. Stellwag, and D. Menzel, Rev. Sci. Instrum. **67**, 378 (1996).

[72] J. B. Pendry, *Low energy electron diffraction* (Academic Press, London, 1974).

[73] S. Y. Tong and M. A. V. Hove, Phys. Rev. B **16**, 1459 (1977).

[74] M. A. V. Hove and S. Y. Tong, *Surface Crystallography by LEED* (Springer, Berlin, 1979).

[75] F. Jona, J. Phys. C: Solid state Phys. **11**, 4271 (1978).

[76] M. A. van Hove, W. H. Weinberg, and C.-M. Chan, *Low-Energy Electron Diffraction* (Springer, Berlin, 1986).

[77] J. B. Pendry, J. Phys. C: Solid state Phys. **13**, 937 (1980).

[78] W. H. Press, B. P. Flannery, S. A. Teukolsky, and W. T. Vetterling, *Numerical Recipes* (Cambridge University Press, Cambridge, 1988).

[79] H. Over *et al.*, Phys. Rev. B **55**, 4731 (1997).

[80] S. Mizuna, T. Shirasawa, Y. Shiraishi, and H. Tochihara, Phys. Rev. B **69**, 241306(R) (2004).

[81] W. Schattke and M. A. van Hove, *Solid-State Photoemission and Related Methods* (Wiley, Weinheim, 2003).

[82] F. Bloch, Z. Physik **52**, 555 (1928).

[83] J. C. Slater and G. F. Koster, Phys. Rev. **94**, 1498 (1954).

[84] P.-O. Löwdin, J. Chem. Phys. **18**, 365 (1950).

[85] W. A. Harrison, *Electronic Structure and Properties of Solids* (Freeman, San Francisco, 1980).

[86] A. V. Podolskiy and P. Vogl, Phys. Rev. B **69**, 233101 (2004).

[87] F. Herman and S. Skillman, *Atomic Structure Calculations* (Prentice Hall, New Jersey, 1963).

[88] Blaha *et al.*, WIEN2k, An Augmented Plane Wave + Local Orbitals Program for Calculating Crystal Properties, Technische Universität Wien (URL http://wien2k. at) .

[89] The ABINIT code is a common project of the Université Catholique de Louvain, Corning Incorporated, and other contributors (URL http://www. abinit. org) .

[90] P. Hohenberg and W. Kohn, Phys. Rev. B **136**, 864 (1964).

[91] W. Kohn and L. J. Sham, Phys. Rev. A **140**, 1133 (1965).

[92] L. Hedin, Phys. Rev. A **139**, 796 (1965).

[93] X. Gonze *et al.*, Z. Kristallogr. **220**, 558 (2005).

[94] CODATA, Internationally recommanded values of the fundamental physical constants, http://physics. nist. gov/constants (2006).

[95] J. Viernow *et al.*, Appl. Phys. Lett. **72**, 948 (1998).

[96] J.-L. Lin *et al.*, J. Appl. Phys. **84**, 327 (1998).

[97] S. Yoshida, T. Sekiguchi, and K. M. Itoh, Appl. Phys. Lett. **87**, 031903 (2005).

[98] P. Wetzel *et al.*, Phys. Rev. B **56**, 9819 (1997).

[99] B. Farid and R. W. Godby, Phys. Rev. B **43**, 14248 (1991).

[100] A. E. Dolbak, B. Z. Olshanetsky, and R. A. Zhachuk, Phys. Low-Dim. Struct. **7/8**, 163 (1999).

[101] R. A. Wolkow, Phys. Rev. Lett. **68**, 2636 (1991).

[102] J. Dabrowski and H. J. Müssig, *Silicon Surfaces and Formation of Interfaces* (World Scientific, Singapore, 2000).

[103] K. Hata, S. Yoshida, and H. Shigekawa, Phys. Rev. Lett. **89**, 286104 (2002).

[104] F. J. Himpsel and E. D. Eastman, J. Vac. Sci. Technol. **16**, 1297 (1979).

[105] D. J. Chadi, Phys. Rev. Lett. **43**, 43 (1979).

[106] P. W. Palmberg and W. T. Peria, Surf. Sci. **6**, 57 (1967).

[107] D. J. Chadi and C. Chiang, Phys. Rev. B **23**, 1843 (1981).

[108] R. S. Becker, J. A. Golovchenko, and B. S. Swartzentruber, Phys. Rev. Lett. **54**, 2678 (1985).

[109] R. G. van Silfhout, J. F. van der Veen, C. Norris, and J. E. Macdonald, Farady Discuss. Chem. Soc. **89**, 169 (1990).

[110] R. E. Schlier and H. E. Farnsworth, J. Chem. Phys. **30**, 917 (1959).

[111] G. Binnig, H. Rohrer, C. Gerber, and E. Weibel, Phys. Rev. Lett. **56**, 1972 (1986).

[112] F. J. Himpsel and T. Fauster, J. Vac. Sci. Technol. A **2**, 815 (1984).

[113] J. E. Northrup, Phys. Rev. Lett. **57**, 154 (1986).

[114] R. I. G. Uhrberg, T. Kaurila, and Y.-C. Chao, Phys. Rev. B **58**, R1730 (1998).

[115] A. A. Baski, S. C. Erwin, and L. J. Whitman, Surf. Sci. **392**, 69 (1997).

[116] R. S. Becker, T. Klitsner, and J. S. Vickers, Phys. Rev. B **38**, 3537 (1988).

[117] R. S. Becker, B. S. Swartzentruber, J. S. Vickers, and T. Klitsner, Phys. Rev. B **39**, 1633 (1989).

[118] S. C. Erwin, Phys. Rev. Lett. **75**, 1973 (1995).

[119] U. Köhler, J. E. Demuth, and R. J. Hamers, J. Vac. Sci. Technol. A **7**, 2860 (1989).

[120] T. Suzuki *et al.*, Surf. Sci. **298**, 473 (1993).

[121] S. C. Erwin, A. A. Baski, and L. J. Whitman, Phys. Rev. Lett. **77**, 687 (1996).

[122] J. M. Gibson, M. L. McDonald, and F. C. Unterwald, Phys. Rev. Lett. **55**, 1765 (1985).

[123] B. Z. Olshanetsky and V. I. Mashanov, Surf. Sci. **111**, 414 (1981).

[124] J. Dabrowski, H.-J. Müssig, and G. Wolff, Phys. Rev. Lett. **73**, 1660 (1994).

[125] A. Laracuente, S. C. Erwin, and L. J. Whitman, Phys. Rev. Lett. **81**, 5177 (1998).

[126] J. Dabrowski, H.-J. Müssig, G. Wolff, and S. Hinrich, Surf. Sci. **411**, 54 (1998).

[127] T. An, M. Yoshimura, I. Ono, and K. Ueda, Phys. Rev. B **61**, 3006 (2000).

[128] A. A. Stekolnikov, J. Furthmüller, and F. Bechstedt, Phys. Rev. Lett **93**, 136104 (2004).

[129] N. D. Kim *et al.*, Phys. Rev. B **75**, 125309 (2007).

[130] F. M. Ross, R. M. Tromp, and M. C. Reuter, Science **286**, 1931 (1999).

[131] J. Dabrowski, H.-J. M*ü*ssig, and G. Wolff, Phys. Rev. Lett. **73**, 1660 (1994).

[132] A. A. Stekolnikov, J. Furthm*ü*ller, and F. Bechstedt, Phys. Rev. B **67**, 195332 (2003).

[133] A. A. Stekolnikov, J. Furthm*ü*ller, and F. Bechstedt, Phys. Rev. B **70**, 045305 (2004).

[134] B. Z. Olshanetsky, S. A. Teys, and I. G. Kozhemyako, Phys. Low-Dimens. Semicond. Struct. **11/12**, 85 (1998).

[135] Z. Gai, R. G. Zhao, T. Sakurai, and W. S. Yang, Phys. Rev. B **63**, 085301 (2001).

[136] B. W. Holland and D. P. Woodruff, Surf. Sci. **36**, 488 (1973).

[137] W. S. Yang and F. Jona, Phys. Rev. B **29**, 899 (1983).

[138] M. K. Debe and D. A. King, Phys. Rev. Lett. **39**, 708 (1977).

[139] H. Tanaka, Y. Watanabe, and I. Sumita, Appl. Surf. Sci. **60**, 474 (1992).

[140] H. Hibino *et al.*, Phys. Rev. B **47**, 13027 (1993).

[141] H. Tanaka, T. Yokoyama, and I. Sumita, Appl. Surf. Sci. **76**, 340 (1994).

[142] H. Hibino and T. Ogino, Surf. Sci. **357**, 102 (1996).

[143] H. Hibino and T. Ogino, Phys. Rev. B **53**, 15682 (1996).

[144] T. Ichikawa *et al.*, Sol. Stat. Comm. **93**, 541 (1995).

[145] Z. Gai, R. G. Zhao, and W. S. Yang, Phys. Rev. B **57**, R6795 (1998).

[146] Y. Yamada *et al.*, Phys. Rev. B **76**, 153309 (2007).

[147] P. Segovia, D. Purdie, M. Hengsberger, and Y. Baer, Nature **402**, 504 (1999).

[148] K. M. Jones, H. H. Song, and A. A. Baski, J. Cluster Science **10**, 573 (1999).

[149] H. Omi and T. Ogino, Phys. Rev. B **59**, 7521 (1999).

[150] H. H. Song, K. M. Jones, and A. A. Baski, J. Vac. Sci. Technol. A **17**, 1696 (1999).

[151] S. C. Erwin, A. A. Baski, L. J. Whitman, and R. E. Rudd, Phys. Rev. Lett. **83**, 1818 (1999).

[152] A. A. Baski, S. C. Erwin, L. J. Whitman, and R. E. Rudd, Surf. Sci. **423**, L265 (1999).

[153] Z. Gai, R. G. Zhao, W. S. Yang, and T. Sakurai, Phys. Rev. B **61**, 9928 (2000).

[154] M. Jalochowski and E. Bauer, Surf. Sci. **480**, 109 (2001).

[155] A. A. Baski, K. M. Saoud, and K. M. Jones, Appl. Surf. Sci. **7150**, 1 (2001).

[156] K. N. Altmann *et al.*, Phys. Rev. B **64**, 035406 (2001).

[157] R. Losio *et al.*, Phys. Rev. Lett. **86**, 4632 (2001).

[158] S. S. Lee *et al.*, Phys. Rev. B **66**, 115317 (2002).

[159] D. Sànchez-Portal, J. D. Gale, A. Garcia, and R. M. Martin, Phys. Rev. B **65**, 081401(R) (2002).

[160] R. Hild *et al.*, Surf. Sci. **512**, 117 (2002).

[161] J. N. Crain *et al.*, Phys. Rev. Lett. **90**, 176805 (2003).

[162] J. R. Ahn, H. W. Yeom, H. S. Yoon, and I.-W. Lyo, Phys. Rev. Lett. **91**, 196403 (2003).

[163] J. N. Crain *et al.*, Phys. Rev. B **69**, 125401 (2004).

[164] J. R. Ahn, H. W. Yeom, E. S. Cho, and C. Y. Park, Phys. Rev. B **69**, 2004 (233311).

[165] J. N. Crain and D. T. Pierce, Science **307**, 703 (2005).

[166] E. S. Cho *et al.*, J. Vac. Sci. Technol. A **23**, 609 (2005).

[167] S. K. Ghose, I. K. Robinson, P. A. Bennett, and F. H. Himpsel, Surf. Sci. **581**, 199 (2005).

[168] M. Krawiec, T. Kwapinski, and M. Jalochowski, Phys. Stat. Sol. b **242**, 332 (2005).

[169] J. R. Ahn, P. G. Kang, K. D. Ryang, and H. W. Yeom, Phys. Rev. Lett. **95**, 196402 (2005).

[170] H. W. Yeom *et al.*, Phys. Rev. B **72**, 035323 (2005).

[171] S. Riikonen and D. Sànchez-Portal, Nanotechnology **16**, S218 (2005).

[172] C. Tegenkamp *et al.*, Phys. Rev. Lett. **85**, 176804 (2005).

[173] M. Krawiec, T. Kwapinski, and M. Jalochowski, Phys. Rev. B **73**, 075415 (2006).

[174] J. A. Lipton-Duffin, J. M. MacLeod, and A. B. McLean, Phys. Rev. B **73**, 245418 (2006).

[175] T. Nagao, S. Yaginuma, T. Inaoka, and T. Sakurai, Phys. Rev. Lett. **97**, 116802 (2006).

[176] P. C. Snijders, S. Rogge, and H. H. Weitering, Europhys. News **37**, 27 (2006).

[177] S. Riikonen and D. Sànchez-Portal, Surf. Sci. **600**, 1201 (2006).

[178] P. C. Snijders, S. Rogge, and H. H. Weitering, Phys. Rev. Lett. **96**, 076801 (2006).

[179] K. S. Kim, W. H. Choi, and H. W. Yeom, Phys. Rev. B **75**, 195324 (2007).

[180] H. Li *et al.*, Phys. Rev. B **75**, 235442 (2007).

[181] H. Okino *et al.*, Phys. Rev. B **76**, 035424 (2007).

[182] K.-D. Ryang, P. G. Kang, and H. W. Yeom, Phys. Rev. B **76**, 205325 (2007).

[183] P. C. Snijders *et al.*, Phys. Rev. Lett. **99**, 116102 (2007).

[184] S. Riikonen and D. Sànchez-Portal, Phys. Rev. B **76**, 035410 (2007).

[185] T. K. Rügheimer, T. Fauster, and F. J. Himpsel, Phys. Rev. B **75**, 121401R (2007).

[186] I. Barke *et al.*, Sol. Stat. Comm. **142**, 617 (2007).

[187] J. R. Ahn, P. G. Kang, J. H. Byun, and H. W. Yeom, Phys. Rev. B **77**, 035401 (2008).

[188] C. Tegenkamp *et al.*, Phys. Rev. Lett. **100**, 076802 (2008).

[189] O. Kubo *et al.*, Phys. Rev. B **64**, 153406 (2001).

[190] A. R. Laracuente and L. J. Whitman, Surf. Sci. **476**, L247 (2001).

[191] A. R. Laracuente and L. J. Whitman, Surf. Sci. **545**, 70 (2003).

[192] I. C. Razado, H. M. Zhang, R. I. G. Uhrberg, and G. V. Hansson, Phys. Rev. B **71**, 235411 (2005).

[193] Y. Suwa *et al.*, Phys. Rev. B **74**, 205308 (2006).

[194] M. Lawrenz *et al.*, Phys. Rev. B **75**, 125424 (2007).

[195] M. W. Radny *et al.*, Phys. Rev. B **76**, 155302 (2007).

[196] J. Nara *et al.*, Phys. Rev. Lett. **100**, 026102 (2008).

[197] S. Vandré, T. Kalka, C. Preinesberger, and M. Dähne-Prietsch, J. Vac. Sci. Technol. B **17**, 1682 (1999).

[198] A. Scandurra, L. Renna, G. Cerofolini, and S. Pignataro, Surf. Interface Anal. **34**, 777 (2002).

[199] J.-H. Choi and J.-H. Cho, Phys. Rev. Lett. **98**, 246101 (2007).

[200] S. Nishikata *et al.*, Phys. Rev. B **76**, 165424 (2007).

[201] V. G. Lifshits, A. A. Saranin, and A. V. Zotov, *Surface Phases on Silicon: Preparation, Structures and Properties* (Wiley, New York, 1994).

[202] R. E. Weber and A. L. Johnson, J. Appl. Phys. **40**, 314 (1969).

[203] H. Daimon and S. Ino, Surf. Sci. **164**, 320 (1985).

[204] W. C. Fan and A. Ignatiev, Phys. Rev. B **40**, 5479 (1989).

[205] F. Wiame *et al.*, Phys. Rev. B **54**, 4480 (1996).

[206] G. L. Lay, M. Manneville, and R. Kern, Surf. Sci. **72**, 1978 (1977).

[207] Y. Gotoh and S. Ino, Jpn. J. Appl. Phys. **17**, 2097 (1978).

[208] K. Sakamoto, H. Ashima, H. M. Zhang, and R. I. G. Uhrberg, Phys. Rev. B **65**, 045305 (2001).

[209] N. Miyata *et al.*, e-J. Surf. Sci. Nanotech. **3**, 151 (2005).

[210] K. J. Wan, X. F. Lin, and J. Nogami, Phys. Rev. B **47**, 13700 (1993).

[211] V. B. et G. Del Re, G. L. Lay, and R. Kern, Surf. Sci. **99**, 223 (1980).

[212] A. Julg and A. Allouche, Int. J. Quantum Chem. **22**, 739 (1982).

[213] G. L. Lay, Surf. Sci. **132**, 169 (1983).

[214] W. S. Yang, S. C. Wu, and F. Jona, Surf. Sci. **169**, 383 (1986).

[215] R. J. Wilson and S. Chiang, Phys. Rev. Lett. **58**, 369 (1987).

[216] W. C. Fan and A. Ignatiev, Phys. Rev. B **41**, 3592 (1990).

[217] M. Tikhov, L. Surnev, and M. Kiskinova, Phys. Rev. B **44**, 3222 (1991).

[218] D. Jeon, T. Hashizume, T. Sakurai, and R. F. Willis, Phys. Rev. Lett. **69**, 1419 (1992).

[219] T. Fukuda, Phys. Rev. B **50**, 1969 (1994).

[220] S. Jeong and M.-H. Kang, Phys. Rev. B **51**, 17635 (1995).

[221] R. Seiwatz, Surf. Sci. **2**, 473 (1964).

[222] H. H. W. et N. J. DiNardo, R. Pérez-Sandoz, J. Chen, and E. J. Mele, Phys. Rev. B **49**, 16837 (1994).

[223] K. S. et T. Okuda *et al.*, Phys. Rev. B **50**, 1725 (1994).

[224] G. C. L. W. et C. A. Lucas, D. Loretto, A. P. Payne, and P. H. Fuoss, Phys. Rev. Lett. **73**, 991 (1994).

[225] K. C. Pandey, Phys. Rev. Lett. **74**, 1913 (1981).

[226] T. O. et H. Shigeoka *et al.*, Surf. Sci. **321**, 105 (1994).

[227] L. Lottermoser *et al.*, Phys. Rev. Lett. **80**, 3980 (1998).

[228] S. Jeong and M. H. Kang, Phys. Rev. B **54**, 8196 (1996).

[229] J. J. Paggel, G. Neuhold, H. Haak, and K. Horn, Phys. Rev. B **52**, 5813 (1995).

[230] S. Olthoff, A. W. McKinnon, and M. E. Welland, Surf. Sci. **326**, 113 (1995).

[231] A. A. Saranin *et al.*, Phys. Rev. B **58**, 3545 (1998).

[232] A. A. Saranin *et al.*, Phys. Rev. B **58**, 7059 (1998).

[233] A. A. S. et A. V. Zotov, V. G. Lifshits, M. Katayama, and K. Oura, Surf. Sci. **426**, 298 (1999).

[234] C. Gollazo-Davila, D. Grozea, and L. D. Marks, Phys. Rev. Lett. **80**, 1678 (1998).

[235] S. C. Erwin and H. H. Weitering, Phys. Rev. Lett. **81**, 2296 (1998).

[236] M.-H. Kang, J.-H. Kang, and S. Jeong, Phys. Rev. B **58**, R13359 (1998).

[237] J. Y. Lee and M.-H. Kang, Phys. Rev. B **66**, 233301 (2002).

[238] H. H. Weitering, X. Shi, and S. C. Erwin, Phys. Rev. B **54**, 10585 (1996).

[239] T. Okuda *et al.*, Phys. Rev. B **55**, 6762 (1997).

[240] M. Gurnett *et al.*, Phys. Rev. B **66**, 161101 (2002).

[241] C. Bromberger *et al.*, Phys. Rev. B **68**, 075320 (2003).

[242] K. Sakamoto and R. I. G. Uhrberg, e-J. Surf. Sci. Nanotech. **2**, 210 (2004).

[243] M. Gurnett *et al.*, Phys. Rev. B **71**, 195408 (2005).

[244] K. J. Wan, X. F. Lin, and J. Nogami, Phys. Rev. B **46**, 13635 (1992).

[245] D. Jeon, T. Hashizume, and T. Sakurai, J. Vac. Sci. Technol. B **12**, 2044 (1994).

[246] H. Ohnishi *et al.*, Appl. Surf. Sci. **82**, 444 (1994).

[247] S. Olthoff and M. E. Welland, J. Vac. Sci. Technol. B **14**, 1019 (1996).

[248] J. M. Carpinelli and H. H. Weitering, Phys. Rev. B **53**, 12651 (1996).

[249] G. Lee, H. Mai, and R. F. Willis, Phys. Rev. B **63**, 085323 (2001).

[250] G. Lee *et al.*, Phys. Rev. B **61**, 9921 (2000).

[251] J. Kuntze, A. Mugarza, and J. E. Ortega, Appl. Phys. Lett. **81**, 2463 (2002).

[252] M. Ueno, I. Matsuda, C. Liu, and S. Hasegawa, Jpn. J. Appl Phys. **52**, 4894 (2003).

[253] M. A. Olmstead, R. I. G. Uhrberg, R. D. Bringans, and R. Z. Bachrach, J. Vac. Sci. Tech. B **4**, 1123 (1986).

[254] M. A. Olmstead, R. I. G. Uhrberg, R. D. Bringans, and R. Z. Bachrach, Phys. Rev. B **35**, 7526 (1987).

[255] J. Quinn and F. Jona, Surf. Sci. **249**, L307 (1991).

[256] K. S. An *et al.*, Surf. Sci. **337**, L789 (1995).

[257] F. Shimokoshi, I. Matsuda, S. Hasegawa, and S. Ino, e-J. Surf. Sci. Nanotech. **2**, 178 (2004).

[258] C. Wigren *et al.*, Phys. Rev. B **48**, 11014 (1993).

[259] C. Wigren *et al.*, Phys. Rev. B **47**, 9663 (1993).

[260] R.-L. Vaara *et al.*, Appl. Surf. Sci. **220**, 327 (2003).

[261] O. Kubo *et al.*, Surf. Sci. **415**, L971 (1998).

[262] A. A. Saranin *et al.*, Surf. Sci. **448**, 87 (2000).

[263] T. Okuda *et al.*, Phys. Rev. B **64**, 165312 (2001).

[264] O. Gallus, T. Pillo, P. Starowicz, and Y. Baer, Europhys. Lett. **60**, 903 (2002).

[265] K. Sakamoto, W. Takeyama, H. M. Zhang, and R. I. G. Uhrberg, Phys. Rev. B **66**, 165319 (2002).

[266] Y. K. Kim *et al.*, Phys. Rev. B **68**, 245312 (2003).

[267] M. Kuzmin *et al.*, Phys. Rev. B **71**, 155334 (2005).

[268] K. Sakamoto *et al.*, Phys. Rev. B **74**, 235311 (2006).

[269] A. A. Baski *et al.*, Surf. Sci. **476**, 22 (2001).

[270] T. Sekiguchi, F. Shimoksoshi, T. Nagao, and S. Hasegawa, Surf. Sci. **493**, 148 (2001).

[271] P. Avouris and R. Wolkow, Appl. Phys. Lett. **55**, 1074 (1989).

[272] G. Lee *et al.*, Phys. Rev. Lett. **87**, 056104 (2001).

[273] D. Y. Petrovykh *et al.*, Surf. Sci. **512**, 269 (2002).

[274] J. Schäfer *et al.*, Phys. Rev. B **67**, 085411 (2003).

[275] G. Lee, S. Hong, H. Kim, and J.-Y. Koo, Phys. Rev. B **68**, 115314 (2003).

[276] F. Palmino *et al.*, Phys. Rev. B **67**, 195413 (2003).

[277] M. Kuzmin *et al.*, Surf. Sci. **538**, 124 (2003).

[278] M. Kuzmin *et al.*, Surf. Sci. **549**, 183 (2004).

[279] K. Sakamoto, A. Pick, and R. I. G. Uhrberg, Phys. Rev. B **72**, 045310 (2005).

[280] T. Okuda, K.-S. An, A. Harasawa, and T. Kinoshita, Phys. Rev. B **71**, 085317 (2005).

[281] K. Sakamoto, A. Pick, and R. I. G. Uhrberg, Phys. Rev. B **72**, 195342 (2005).

[282] C. Eames, M. I. J. Probert, and S. P. Tear, Phys. Rev. B **75**, 205420 (2007).

[283] R. H. Miwa, Phys. Rev. B **72**, 085325 (2005).

[284] S. Jeong, J. Y. Lee, and M. H. Kang, Phys. Rev. B **72**, 193309 (2005).

[285] T. Sekiguchi, T. Nagao, and S. Hasegawa, e-J. Surf. Sci. Nanotech. **1**, 26 (2003).

[286] A. Kirakosian *et al.*, Surf. Sci. **498**, L109 (2002).

[287] J. L. McChesney *et al.*, Nanotechnology **13**, 545 (2002).

[288] T. J. Wood, private communication (2007).

[289] I. Engelhardt *et al.*, Surf. Sci. **600**, 755 (2006).

[290] F. J. Himpsel *et al.*, J. Phys. Chem. B **108**, 14484 (2004).

[291] E. W. Perkins, I. M. Scott, and S. P. Tear, Surf. Sci. **578**, 80 (2005).

[292] T. Okuda *et al.*, J. Electron Spectros. And Relat. Phenom. **137**, 125 (2004).

[293] E. V. Sampathkumaran, L. C. Gupta, and R. Vijayaraghavan, J. Phys. C: Solid State Phys. **12**, 1979 (1979).

[294] Z. Hu, G. Kaindl, and B. G. Müller, J. Alloys Comp. **246**, 177 (1997).

[295] B. T. Kilbourn, in *Kirk-Othmer Encyclopedia of Chemical Technology* (Wiley, New York, 2003), Chap. Cerium and Cerium Compounds.

[296] P. Dorenbos, J. Phys. : Condens. Matter **15**, 575 (2003).

[297] P. Dorenbos, J. Lumin. **91**, 91 (2003).

[298] P. Dorenbos, J. Lumin. **91**, 155 (2003).

[299] G. Wiese, H. Schäffer, and B. Elschner, Europhys. Lett. **11**, 791 (1990).

[300] W.-D. Schneider, private communication (2007).

[301] M. Kuzmin *et al.*, Phys. Rev. B **75**, 165305 (2007).

[302] T. V. Krachino, M. V. Kuz'min, M. V. Loginov, and M. A. Mittsev, Phys. Solid State **40**, 341 (1998).

[303] C. Bonet *et al.*, Phys. Rev. B **72**, 165407 (2005).

[304] C. Battaglia *et al.*, Europhys. Lett. **77**, 36003 (2007).

[305] C. Battaglia *et al.*, J. Phys. : Conf. Ser. **100**, 052078 (2008).

[306] C. Battaglia, P. Aebi, and S. C. Erwin, to be published (2008).

[307] G. Lee, J. Guo, and E. W. Plummer, Phys. Rev. Lett. **95**, 116103 (2005).

[308] S. J. Park, H. W. Yeom, J. R. Ahn, and I.-W. Lyo, Phys. Rev. Lett. **95**, 126102 (2005).

[309] J. Guo, G. Lee, and E. W. Plummer, Phys. Rev. Lett. **95**, 046102 (2005).

[310] J. R. Ahn *et al.*, Phys. Rev. Lett. **93**, 106401 (2004).

[311] S. C. Erwin, Phys. Rev. Lett. **91**, 206101 (2003).

[312] C. Battaglia *et al.*, to be published (2008).

[313] G. Kresse and J. Hafner, Phys. Rev. B **47**, 558 (1993).

[314] G. Kresse and J. Furthmüller, Phys. Rev. B **54**, 11169 (1996).

[315] E. Kaxiras, Y. Bar-Yam, J. D. Joannopoulos, and K. C. Pandey, Phys. Rev. B **35**, 9625 (1987).

[316] K. D. Brommer, M. Needles, B. Larson, and J. D. Joannopoulos, Phys. Rev. Lett. **68**, 1355 (1992).

[317] C. Rogero *et al.*, Phys. Rev. B **69**, 045312 (2004).

[318] J. J. Lander and J. Morrison, J. Appl. Phys. **36**, 1706 (1965).

[319] C. Collazo-Davila, L. D. Marks, K. Nishii, and Y. Tanishiro, Surf. Rev. Lett. **4**, 65 (1997).

[320] A. A. Saranin *et al.*, Phys. Rev. B **56**, 1017 (1997).

[321] A. A. Saranin *et al.*, Phys. Rev. B **55**, 5353 (1997).

[322] A. V. Zotov and A. A. Saranin, Appl. Surf. Sci. **159**, 237 (2000).

[323] N. Nakamura, K. Anno, and S. Kono, Surf. Sci. **256**, 129 (1991).

[324] O. Bunk *et al.*, Phys. Rev. B **59**, 12228 (1999).

[325] J. Wang *et al.*, Phys. Rev. B **72**, 245324 (2005).

[326] R. H. Miwa and G. P. Srivastava, Surf. Sci. **473**, 123 (2001).

[327] J.-H. Cho, D.-H. Oh, K. S. Kim, and L. Kleinman, Phys. Rev. B **64**, 235302 (2001).

[328] G. Lee *et al.*, Phys. Rev. B **67**, 035327 (2003).

[329] S. Wang, W. Lu, W. G. Schmidt, and J. Bernholc, Phys. Rev. B **68**, 035329 (2003).

[330] G. Lee, S.-Y. Yu, H. Kim, and J.-Y. Koo, Phys. Rev. B **70**, 121304 (2004).

[331] J.-H. Cho, J.-Y. Lee, and L. Kleinman, Phys. Rev. B **71**, 081310 (2005).

[332] X. López-Lozano, A. A. Stekolnikov, J. Furthmüller, and F. Bechstedt, Phys. Rev. B **589**, 77 (2005).

[333] C. Gonzáles, J. Ortega, and F. Flores, New J. Phys. **7**, 100 (2005).

[334] S.-F. Tsay, Phys. Rev. B **71**, 035207 (2005).

[335] C. Gonzáles, F. Flores, and J. Ortega, Phys. Rev. Lett. **96**, 136101 (2006).

[336] S. Riikonen, A. Ayuela, and D. Sànchez-Portal, Surf. Sci. **600**, 3821 (2006).

[337] X. López-Lozano *et al.*, Phys. Rev. B **73**, 035430 (2006).

[338] J.-H. Cho and J.-Y. Lee, Phys. Rev. B **76**, 033405 (2007).

[339] A. A. Stekolnikov *et al.*, Phys. Rev. Lett. **98**, 026105 (2007).

[340] H. Öfner, S. L. Surnev, Y. Shapira, and F. P. Netzer, Phys. Rev. B **48**, 10940 (1993).

[341] T. Abukawa *et al.*, Surf. Sci. **325**, 33 (1995).

[342] I. G. Hill and A. B. McLean, Phys. Rev. B **56**, 15725 (1997).

[343] I. G. Hill and A. B. McLean, Phys. Rev. B **59**, 9791 (1999).

[344] H. W. Yeom *et al.*, Phys. Rev. Lett. **82**, 4898 (1999).

[345] O. Gallus *et al.*, Eur. Phys. J. B **20**, 313 (2001).

[346] H. W. Yeom, J. Electron Spectros. and Relat. Phenom. **114**, 283 (2001).

[347] H. W. Yeom *et al.*, Phys. Rev. B **65**, 241307 (2002).

[348] J. R. Ahn, J. H. Byun, J. K. Kom, and H. W. Yeom, Phys. Rev. B **75**, 033313 (2007).

[349] Y. J. Sun *et al.*, Phys. Rev. B **77**, 125115 (2008).

[350] J. Nogami, S. Park, and C. F. Quate, Phys. Rev. B **36**, 6221 (1987).

[351] J. L. Stevens, M. S. Worthington, and I. S. T. Tsong, Phys. Rev. B **47**, 1453 (1993).

[352] F. Owman and P. Mårtensson, Surf. Sci. **359**, 122 (1996).

[353] H. Morikawa, I. Matsuda, and S. Hasewaga, Phys. Rev. B **70**, 085412 (2004).

[354] S. Kurata and T. Yokoyama, Phys. Rev. B **71**, 121306 (2005).

[355] C. Kumpf *et al.*, Phys. Rev. Lett. **85**, 4916 (200).

[356] S. Hasegawa, J. Phys. : Condens. Matter **12**, R463 (2000).

[357] K. Sakamoto, H. Ashima, H. W. Yeom, and W. Uchida, Phys. Rev. B **62**, 9923 (2000).

[358] T. Kanagawa *et al.*, Phys. Rev. Lett. **91**, 036805 (2003).

[359] T. Tanikawa, I. Matsuda, T. Kanagawa, and S. Hasewaga, Phys. Rev. Lett. **93**, 016801 (2004).

[360] K. Fleischer *et al.*, Appl. Surf. Sci. **234**, 302 (2004).

[361] K. Fleischer *et al.*, Phys. Rev. B **76**, 205406 (2007).

[362] H. W. Yeom, Phys. Rev. Lett. **97**, 189701 (2006).

[363] C. Gonzáles, F. Flores, and J. Ortega, Phys. Rev. Lett. **97**, 189702 (2006).

[364] H. E. Bishop and J. C. Rivière, J. Phys. D **2**, 1635 (1969).

[365] H. Lipson and K. E. Singer, J. Phys. C **7**, 12 (1974).

[366] G. Lelay and J. P. Faurie, Surf. Sci. **69**, 295 (1977).

[367] T. Hasegawa, K. Takata, S. Hosaka, and S. Hosoki, J. Vac. Sci. Technol. A **9**, 241 (1990).

[368] A. A. Baski, J. Nogami, and C. F. Quate, Phys. Rev. B **41**, 10247 (1990).

[369] J. D. O'Mahony *et al.*, Surf. Sci. **277**, L57 (1992).

[370] J. D. O'Mahony *et al.*, Phys. Rev. B **49**, 2527 (1994).

[371] L. D. Marks and R. Plass, Phys. Rev. Lett. **75**, 2172 (1995).

[372] I. R. Collins *et al.*, Surf. Sci. **325**, 45 (1995).

[373] R. Losio, K. N. Altmann, and F. J. Himpsel, Phys. Rev. B **85**, 808 (2000).

[374] I. Matsuda *et al.*, Phys. Rev. B **68**, 195319 (2003).

[375] R. Bennewitz *et al.*, Nanotechnology **13**, 499 (2002).

[376] A. Kirakosian *et al.*, Surf. Sci. **532**, 928 (2003).

[377] A. Kirakosian, R. Bennewitz, F. J. Himpsel, and L. W. Bruch, Phys. Rev. B **67**, 205412 (2003).

[378] J. L. McChesney *et al.*, Phys. Rev. B **70**, 195430 (2004).

[379] H. S. Yoon *et al.*, Phys. Rev. Lett. **92**, 096801 (2004).

[380] H. S. Yoon *et al.*, Phys. Rev. B **72**, 155443 (2005).

[381] S. Riikonen and D. Sànchez-Portal, Phys. Rev. B **71**, 235423 (2005).

[382] C.-Y. Ren, S.-F. Tsay, and F.-C. Chuang, Phys. Rev. B **76**, 075414 (2007).

[383] A.-L. Chin and F.-K. Men, Phys. Rev. B **76**, 073403 (2007).

[384] W. H. Choi, P. G. Kang, K. D. Ryang, and H. W. Yeom, Phys. Rev. Lett. **100**, 126801 (2008).

[385] I. K. Robinson, P. A. Bennett, and F. J. Himpsel, Phys. Rev. Lett. **88**, 096104 (2002).

[386] D. Sánchez-Portal and R. M. Martin, Surf. Sci. **532**, 665 (2003).

[387] H. Okino *et al.*, Phys. Rev. B **70**, 113404 (2004).

[388] S. Riikonen and D. Sànchez-Portal, arXiv:0712. 1735 (2007).

[389] A. A. Baski, K. M. Saoud, and K. M. Jones, Ultramicroscopy **86**, 23 (2001).

[390] J. L. McChesney, J. N. Crain, F. J. Himpsel, and R. Bennewitz, Phys. Rev. B **72**, 035446 (2005).

[391] J. Quinn, Y. S. Li, F. Jona, and D. Fort, Phys. Rev. B **46**, 9694 (1992).

[392] P. Starowicz *et al.*, J. All. Comp. **442**, 268 (2007).

[393] M. GoshtasbiRad, M. Göthelied, B. Hirschhauer, and U. O. Karlsson, Surf. Sci. **166**, 209 (2000).

[394] M. GoshtasbiRad, M. Göthelied, G. LeLay, and U. O. Karlsson, Surf. Sci. **558**, 49 (2004).

[395] H. G. Lee, D. Lee, S. Kim, and C. Hwang, Surf. Sci. **596**, 39 (2005).